

Numerically Exact Simulation of Non-Markovian Open Quantum Dynamics

Dissertation

zur Erlangung des Doktorgrades
an der Fakultät für Mathematik,
Informatik und Naturwissenschaften

Fachbereich Physik

Universität Hamburg

vorgelegt von

Florian Benedikt Otterpohl

Hamburg
2024

Gutacher der Dissertation:

Prof. Dr. Michael Thorwart
Prof. Dr. Walter Strunz

Zusammensetzung der Prüfungskommission:

Prof. Dr. Daniela Pfannkuche
Prof. Dr. Michael Thorwart
Prof. Dr. Walter Strunz
Prof. Dr. Michael Potthoff
Prof. Dr. Christian Bressler

Vorsitzende der Prüfungskommission:

Prof. Dr. Daniela Pfannkuche

Datum der Disputation:

30.08.2024

Vorsitzender des Fach-
Promotionsausschusses Physik:

Prof. Dr. Markus Drescher

Leiter des Fachbereichs Physik:

Prof. Dr. Wolfgang J. Parak

Dekan der Fakultät MIN:

Prof. Dr.-Ing. Norbert Ritter

Und an seines Hauses Schwelle
Wird ein jeder festgebannt;
Aber Liebesfäden spinnen
Heimlich sich von Land zu Land.

– *Theodor Storm*

Abstract

This thesis focuses on the numerically exact computation of the nonequilibrium quantum dynamics of several instances of the Caldeira-Leggett model. It begins with a detailed derivation of the quasi adiabatic propagator path integral method, along with a minor improvement of the original iteration scheme. Additionally, the small matrix decomposition of the path integral expression is derived, and the approximation it introduces is systematically analyzed. Next, an introduction to the tensor network formalism is provided, followed by a derivation of the time-evolving matrix product operator (TEMPO) technique that is significantly simpler than what is given in the original literature. TEMPO is benchmarked on a trivially solvable model, revealing its quadratic computational complexity with respect to the inverse discretized time step. By utilizing TEMPO, a novel dynamical phase of the (sub-)Ohmic spin-boson model at zero temperature is discovered, and a corresponding phase diagram is obtained. Furthermore, the dephasing rate at weak system-bath coupling in the (sub-)Ohmic and the $1/f$ regime is studied. The TEMPO method is then generalized to the case of multiple baths acting on the central system, and subsequently used to study the disruption of the quantum Zeno effect in the Ohmic spin-boson model. Finally, the hierarchical equations of motion technique is summarized and used to demonstrate that a spectroscopic technique known as transient redistribution of ultrafast electronic coherences in attosecond Raman signals is robust against environmental dissipation at room temperature.

Zusammenfassung

Diese Arbeit beschäftigt sich mit der numerisch exakten Berechnung verschiedener Instanzen des Caldeira-Leggett-Modells. Sie beginnt mit einer detaillierten Herleitung des quasiadiabatischen Propagator-Pfadintegrals (QUAPI) und einer geringfügigen Verbesserung des ursprünglichen Iterationsschemas. Darüber hinaus wird die kleine Matrixzerlegung des Pfadintegralausdrucks (SMatPI) hergeleitet und die dadurch eingeführte Näherung systematisch analysiert. Daraufhin wird der Tensornetzwerk-Formalismus eingeführt, gefolgt von einer Herleitung des zeitlich sich entwickelnden Matrixproduktoperators (TEMPO), die wesentlich einfacher ist als die in der ursprünglichen Literatur beschriebene. TEMPO wird an einem trivial lösbaeren Modell getestet, wobei gezeigt wird, dass dessen Rechenkomplexität quadratisch im inversen diskretisierten Zeitschritt ist. Durch den Einsatz von TEMPO wird eine neue dynamische Phase des (sub-)ohmschen Spin-Bosonen-Modells bei Nulltemperatur entdeckt und ein entsprechendes Phasendiagramm erhalten. Außerdem wird die Dephasierungsrate bei schwacher System-Bad-Kopplung im (sub-)Ohmschen und im $1/f$ -Regime untersucht. Die TEMPO-Methode wird dann auf den Fall verallgemeinert, dass mehrere Bäder auf das zentrale System einwirken, und anschließend verwendet, um die Störung des Quanten-Zeno-Effekts im Ohmschen Spin-Boson-Modell zu untersuchen. Schließlich wird die Methode der hierarchischen Bewe-

gungsgleichungen (HEOM) zusammengefasst und angewandt, um zu demonstrieren, dass eine spektroskopische Technik, die als transiente Umverteilung ultraschneller elektronischer Kohärenzen in Attosekunden-Raman-Signalen bekannt ist, bei Raumtemperatur robust gegenüber Störungen durch die Umgebung ist.

List of Publications

- F. Otterpohl, P. Nalbach, and M. Thorwart, Hidden Phase of the Spin-Boson Model, *Phys. Rev. Lett.* **129**, 120406 (2022). (see Chapter 4)
 - Ph. Nacke, F. Otterpohl, M. Thorwart, and P. Nalbach, Dephasing and Pseudo-coherent Quantum Dynamics in Super-Ohmic Environments, *Phys. Rev. A* **107**, 062218 (2023). (not included in this thesis)
 - F. Otterpohl, D. Keefer, S. Mukamel, and M. Thorwart, Coherent ultrafast stimulated x-ray Raman spectroscopy of dissipative conical intersections, *submitted* (see Chapter 6)
 - F. Otterpohl, P. Nalbach, and M. Thorwart, Quantum $1/f$ Noise Induced Relaxation in the Spin-Boson Model, *submitted* (see Chapter 5)
-

Contents

1	Introduction	1
2	Quasi Adiabatic Propagator Path Integral (QUAPI)	5
2.1	Propagators	5
2.1.1	Free Particle	8
2.1.2	Driven Harmonic Oscillator	8
2.2	Equilibrium Density Matrix	10
2.2.1	Harmonic Oscillator	10
2.3	System-Bath Model	11
2.4	Discretizing the Path Integral	15
2.5	Polarized Initial Conditions	19
2.6	Blip Decomposition	20
2.7	Iterative QUAPI	21
2.7.1	Deviation from the Full Path Sum	23
2.8	Improved Iterative QUAPI	23
2.9	SMatPI	25
2.9.1	Deviation from i-QUAPI	27
2.10	χ -SMatPI	28
2.10.1	Deviation from the Full Path Sum	29
3	Time-Evolving Matrix Product Operator (TEMPO)	31
3.1	Introduction to Tensor Networks	32
3.2	TEMPO: Computing QUAPI using a Tensor Network	36
3.3	Benchmark of TEMPO on a Single Mode Model	40
3.4	Generalization of TEMPO to Non-Commuting Baths	42
3.4.1	Verification Based on Previous Results	46
3.4.2	Quantum Zeno Disruption by Non-Commuting Baths	47
3.5	Summary	49
4	Hidden Phase of the Spin-Boson Model	51
4.1	Previous Publications	51
4.2	Dynamical Phase Diagram	54
4.3	Summary	59

5	1/f Quantum Noise in the Spin-Boson Model	61
5.1	Extended Phase Diagram	62
5.2	Dephasing Rate	62
5.3	Reorganization Energy	65
5.4	Summary	65
6	Coherent Ultrafast Stimulated X-Ray Raman Spectroscopy of Dissipative Conical Intersections	67
6.1	Hierarchical Equations of Motion (HEOM)	67
6.1.1	Benchmark	69
6.2	Model	72
6.2.1	Mapping to an Effective Spin-Boson Model	74
6.3	Dissipative Transient Redistribution of Ultrafast Electronic Coherences in Attosecond Raman Signals	74
6.3.1	Frequency-Resolved Optical Gating (FROG) Spectrogram	77
6.4	Summary	78
7	Conclusion and Outlook	79
	Bibliography	81
	Eidesstattliche Versicherung	91

1 Introduction

Aristotle postulated that a particle could only maintain its velocity if a force is applied, corresponding to $\dot{x} \propto \mathbf{F}$ [1]. Two millennia later, Isaac Newton recognized that this applies only in the special case where significant friction is present. He proposed the more general equation of motion $\mathbf{F} = m\ddot{x}$. Centuries later, physicists realized that the idea of a particle having a fixed location and momentum simultaneously is an approximation that breaks down at small scales or low temperatures due to quantum effects. To account for these effects, they introduced the concept of a state vector in a Hilbert space as a complete description of a particle's state. Neglecting relativistic effects, the time evolution of this state is governed by the Schrödinger equation, which is the fundamental equation of motion this thesis is based upon.

Quantum mechanics allows for phenomena with no classical equivalent. An example is the directly observable kaon oscillation [2]. Neither the neutral kaon K^0 nor its antiparticle \bar{K}^0 is an energy eigenstate due to the weak interaction, resulting in coherent oscillations between these two particles. Another example is given by qubits in a quantum computer, where interaction with the environment is a critical issue. While isolated to preserve quantum coherence, qubits also need to be controllable, which inevitably introduces environmental noise [3]. Other examples of these coherent oscillations are ubiquitous in quantum mechanics, including tunneling between different molecular configurations, chemical reaction dynamics, and the transport of excitations within molecules.

To study environmental effects on these oscillations, the Caldeira-Leggett model [4] models the environment as a set of uncoupled harmonic oscillators that are bilinearly coupled to the system of interest. The oscillator bath, typically initialized in thermal equilibrium, is integrated out as only the system dynamics is of interest. Due to the response of the bath, the system dynamics generally becomes non-Markovian, as the bath retains a *memory* of the system's past interactions. As an analogy, imagine the system being like a ship being influenced by waves it has generated itself.

The influence of the bath on the system can be fully characterized by specifying its temperature and *spectral density* $J(\omega)$, which corresponds to the coupling strength density to the bath modes of frequency ω . Unsurprisingly, the bath generally introduces tremendous complexity to the model. Even for a simple two-level system (this case is also known as the *spin-boson model*), no general solutions exist for all temperatures and spec-

tral densities.

While in many cases where the coupling between the central system and the bath is weak, a Markovian approximation leading to a master equation for the reduced density matrix (which is the density matrix of the central system only) is justified [5], this work focuses on a numerically exact treatment. The path integral formalism allows analytically integrating out the environment [6]. The system dynamics can then be represented as a path integral over all system paths only, with the entire influence of the bath on each path being encoded in the Feynman-Vernon influence functional. Quantum Monte Carlo methods tackle this in general exponentially complex problem by sampling these paths [7]. The quasi adiabatic propagator path integral (QUAPI) method is based on directly evaluating a path sum, which is the discretized version of the path integral. Originally, a controlled cutoff of the bath memory was employed to make the summation tractable, leading to an iterative tensor multiplication scheme [8, 9]. The small matrix decomposition of the path integral (SMatPI) [10] eliminates the large memory requirements of this scheme. Both QUAPI and SMatPI will be covered in detail in chapter 2.

Using the QUAPI formalism, the path sum can be calculated in terms of contracting a tensor network, which is then referred to as the time-evolving matrix product operator (TEMPO) method [11]. This method will be derived in a novel simplified fashion in chapter 3. The hierarchical equations of motion (HEOM) technique [12] has also been derived from the Feynman-Vernon influence functional. It yields a temporal differential equation for the reduced density matrix coupled to differential equations for nonphysical auxiliary density matrices that encode the bath dynamics. A similar set of differential equations is obtained in the hierarchy of pure states (HOPS) [13] method. While HEOM was originally limited to the *Ohmic* case $J(\omega) \propto \omega$, it has been generalized to handle the *super-Ohmic* ($J(\omega) \propto \omega^s$ with $s > 1$) and *sub-Ohmic* ($J(\omega) \propto \omega^s$ with $s < 1$) cases [14, 15]. The advantages of HEOM include its straightforward generalization to multiple baths and superior efficiency compared to QUAPI for some specific spectral densities. On the other hand, it offers less flexibility with respect to bath temperature and the specific form of the spectral density, which are both strengths of QUAPI.

Among the numerically exact methods applicable to the spin-boson model that are not based on the Feynman-Vernon influence functional is the multiconfiguration time-dependent Hartree (MCTDH) technique [16, 17]. Its efficiency has been improved using a multi-layered recursive approach (referred to as ML-MCTDH) [18] and a matrix product state representation [19]. Finally, the numerical renormalization group is mentioned, which involves a mapping to a semi-infinite chain and subsequent iterative numerical diagonalization [20].

At low temperatures and weak system bath coupling strength, the spin-boson model

typically exhibits damped coherent oscillations between the two central system states with decreasing amplitude due to the influence of the bath [2]. Stronger dissipation or high temperatures generally lead to incoherent decay towards a delocalized state. At zero temperature and strong dissipation, the system can even become localized, trapped in its initial state due to the constant influence of the environment acting like a measurement.

For the sub-Ohmic spin-boson model without a high-frequency cutoff of the spectral density, the system always localizes at zero temperature regardless of the coupling strength [2]. However, in experimentally realistic settings with sub-Ohmic noise, encountered for example in some nano-mechanical devices [21] and amorphous solids [22], the bath always has a high-frequency cutoff as its energy has to be finite. While all subsequent numerical studies found damped coherent oscillations at weak coupling, they have been inconclusive about the fate of the coherence at strong coupling [15, 23, 24]. Chapter 4 (published in Ref. [25]) resolves this issue by identifying a novel *pseudo-coherent* phase. This phase occurs at strong coupling and is solely a consequence of the finite bath reaction time due to the high-frequency cutoff. It causes an initial shallow, non-coherent minimum in the dynamics, effectively overdamping the system in this regime. A subsequent study has also shown this phase for a super-Ohmic spectral density [26].

While originally considered to be pathological [2], the case of $1/f$ quantum noise with spectral exponents $s < 0$ has been recognized as a major factor in the loss of coherence (dephasing) of superconducting qubits due to magnetic flux noise [27]. Additionally, the electronic spin of a color center that couples to the vibrational motion of hexagonal boron nitride membranes has been addressed in terms of the spin-boson model with $s = -1$ using approximate numerical tools [28]. Due to its notorious difficulty, a numerically exact investigation of the corresponding highly non-Markovian and strongly damped quantum dissipative dynamics had remained elusive. In chapter 5, the quantum $1/f$ noise regime is investigated numerically exactly.

In chapter 3.4, the TEMPO method is generalized to handle cases where the system interacts with multiple baths through operators that do not commute with each other. Physical realizations of such cases include voltage fluctuations in quantum dot qubits [29], magnetic field fluctuations in nuclear magnetic resonance spectroscopy [2], and molecular vibronic dynamics [30, 31]. The novel method is used to demonstrate how a second bath can suppress the localization transition in the Ohmic spin-boson model.

In molecules, the electronic energies generally depend on the configuration of the nuclei, giving rise to the *electronic potential energy surfaces*. The existence of *conical intersections* is crucial for many photochemical processes [32–35]. These intersections occur when two or more electronic potential energy surfaces intersect, allowing for rapid radiationless transitions between electronic states. In this regime, electronic and nuclear motion be-

comes strongly coupled, rendering the Born-Oppenheimer approximation invalid [36]. Due to the significant change in the energy gap between the electronic states near conical intersections, which is traversed by the wavepackets on a short femtosecond timescale, directly observing this process requires both high temporal and spectral resolution [37]. Consequently, conical intersections have only been observed indirectly through decay rates [38] or rapidly changing optical spectra [37].

The transient redistribution of ultrafast electronic coherences in attosecond Raman signals (TRUECARS) technique utilizes a combination of broadband and narrowband X-ray pulses to achieve the necessary resolution for directly measuring a wavepacket moving through a conical intersection [39]. Since the off-resonant X-ray pulses do not directly excite the molecule's core electrons, the signal is not influenced by the electronic population dynamics and thus provides a background-free measure of coherences. While implementing TRUECARS is experimentally challenging due to the precise phase control required between the X-ray pulses, recent advancements in free-electron lasers have made it potentially achievable. So far, TRUECARS has only been studied theoretically for isolated quantum systems [39–42], leaving the open question to what extent strong electronic or vibrational dissipation smear out such quantum coherences on ultrashort times. In chapter 6, the effect of dissipation on the TRUECARS signal is investigated in a model system with two molecular electronic states and two vibrational modes. An oscillator bath coupled to the electronic states models the fluctuating electric fields produced by surrounding solvent molecules, while additional oscillator baths coupled to the vibrational modes model the fluctuating nuclei of the host molecule. It is concluded that TRUECARS should be sufficiently robust to be measurable in a future spectroscopic experiment.

Throughout this thesis, natural units are used, where the reduced Planck constant \hbar and the Boltzmann constant k_B are both set to 1.

2 Quasi Adiabatic Propagator Path Integral (QUAPI)

As a discretized form of the real-time path integral for a multilevel quantum system bilinearly coupled to a bath of uncoupled harmonic oscillators, QUAPI [8, 9] enables the numerically exact evaluation of non-Markovian quantum dissipative dynamics in terms of a path summation.

In this chapter, the QUAPI-algorithm is re-derived. Following the presentation of Ref. [43], we start with the Schrödinger equation and derive the Feynman-Vernon influence functional. Following the work of Ref. [29], we discretize the path integral in time, which is the essence of QUAPI. Then, its generalization to polarized bath initial conditions as used in Ref. [23] is introduced. While the rest of the chapter has not been used in generating the results of this work, a few additional insights into QUAPI are presented. Section 2.6 summarizes the blip decomposition of Ref. [44] as an example of a non-tensor network approach to speed up path summation. Then, a version of the original iteration scheme of QUAPI is presented in Section 2.7 where the Trotter splitting used in Ref. [45] is employed. The modified Trotter splitting slightly simplifies and reduces the computational cost of the original iterative QUAPI scheme and of the algorithms presented in the following sections. The iterative QUAPI algorithm has been used in many publications over the last decades, including in the investigation of dissipative effects in quantum bits [46, 47], Landau-Zener transitions [48], and exciton transfer dynamics in a photosynthetic complex [49]. In section 2.8, a novel (however, due to other recent advancements less relevant) improvement of this scheme is introduced. In the final sections, the small matrix decomposition of the path integral expression (SMatPI) [50] and its extension [51] is presented and the approximations they introduce are analyzed beyond what is given in the literature.

Naturally, there is some overlap with Ref. [52] throughout this chapter.

2.1 Propagators

The subsequent standard derivation follows the presentation of chapter 2 in Ref. [43]. The Schrödinger equation is given by

$$i\partial_t |\psi\rangle = \hat{H} |\psi\rangle. \quad (2.1)$$

If \hat{H} is time-independent, its formal solution reads

$$|\psi(t)\rangle = \exp(-i\hat{H}t) |\psi(0)\rangle. \quad (2.2)$$

The Hamiltonian of a particle in a potential $V(\hat{x})$ is given by

$$\hat{H} = \frac{\hat{p}^2}{2m} + V(\hat{x}). \quad (2.3)$$

In the completeness relation in position space

$$\mathbb{1}_{(k)} = \int dx_k |x_k\rangle \langle x_k|, \quad (2.4)$$

we will use the index k to discriminate between multiple insertions of the completeness relation. As in Eq. (24) of Ref. [43], the propagator in coordinate representation can be written as

$$\begin{aligned} U(x_N, t_N; x_0, 0) &= \langle x_N | \exp(-i\hat{H}t_N) | x_0 \rangle = \langle x_N | \exp(-i\hat{H}\Delta t)^N | x_0 \rangle \\ &= \int \left(\prod_{k=1}^{N-1} dx_k \right) \prod_{k=1}^N \langle x_k | e^{-i\hat{H}\Delta t} | x_{k-1} \rangle, \end{aligned} \quad (2.5)$$

where $t_N = N\Delta t$. As in Eq. (21) of Ref. [43], we make use of the Baker-Campbell-Hausdorff formula:

$$\exp(-i\hat{H}\Delta t) = \exp\left(-i\frac{\hat{p}^2}{2m}\Delta t\right) \exp(-iV(\hat{x})\Delta t) + \mathcal{O}(\Delta t^2). \quad (2.6)$$

Thus, the short-time propagator $U(x_k, t_k; x_{k-1}, t_{k-1})$ can be expressed as

$$\begin{aligned} \langle x_k | e^{-i\hat{H}\Delta t} | x_{k-1} \rangle &= \int dp_k \langle x_k | p_k \rangle \langle p_k | \exp(-i\hat{H}\Delta t) | x_{k-1} \rangle \\ &= \int dp_k \langle x_k | p_k \rangle \left\langle p_k \left| \exp\left(-i\frac{\hat{p}^2}{2m}\Delta t\right) \exp(-iV(\hat{x})\Delta t) \right| x_{k-1} \right\rangle + \mathcal{O}(\Delta t^2) \\ &= \exp(-iV(x_{k-1})\Delta t) \int dp_k \exp\left(-i\frac{p_k^2}{2m}\Delta t\right) \langle x_k | p_k \rangle \langle p_k | x_{k-1} \rangle + \mathcal{O}(\Delta t^2) \\ &= \exp(-iV(x_{k-1})\Delta t) \int dp_k \frac{1}{2\pi} \exp\left(-i\frac{p_k^2}{2m}\Delta t + ip_k(x_k - x_{k-1})\right) + \mathcal{O}(\Delta t^2) \\ &= \sqrt{\frac{m}{2\pi i\Delta t}} \exp\left(i\frac{m}{2\Delta t}(x_k - x_{k-1})^2\right) \exp(-i\Delta t V(x_{k-1})) + \mathcal{O}(\Delta t^2), \end{aligned} \quad (2.7)$$

where the completeness relation in momentum space has been used in the first step and the eigenstate of the momentum operator in position space

$$\langle x | p \rangle = \frac{1}{\sqrt{2\pi}} \exp(ipx) \quad (2.8)$$

has been used in the third step. Using Eq. (2.7), we rewrite Eq. (2.5) as

$$U(x_N, t_N; x_0, 0) = \lim_{N \rightarrow \infty} \int \left(\prod_{k=1}^{N-1} dx_k \right) \left(\frac{m}{2\pi i \Delta t} \right)^{N/2} \cdot \exp \left(i \Delta t \sum_{k=1}^N \left[\frac{m}{2} \left(\frac{x_k - x_{k-1}}{\Delta t} \right)^2 - V(x_{k-1}) \right] \right) \quad (2.9)$$

to yield Eq. (26) of Ref. [43]. As a shorthand notation, the *real time path integral* is defined as

$$\int_{(x_0, 0)}^{(x_N, t_N)} \mathcal{D}[x(t)] := \lim_{N \rightarrow \infty} \int \left(\prod_{k=1}^{N-1} dx_k \right) \left(\frac{m}{2\pi i \Delta t} \right)^{N/2}. \quad (2.10)$$

By use of

$$\frac{x_k - x_{k-1}}{\Delta t} = \frac{x(k\Delta t) - x((k-1)\Delta t)}{\Delta t} = \dot{x}((k-1)\Delta t) + \mathcal{O}(\Delta t^2) \quad (2.11)$$

and

$$\lim_{N \rightarrow \infty} \left(\Delta t \sum_{k=1}^N f[x((k-1)\Delta t)] \right) = \int_0^{t_N} dt f(x(t)), \quad (2.12)$$

Eq. (2.9) becomes

$$U(x_N, t_N; x_0, 0) = \int_{(x_0, 0)}^{(x_N, t_N)} \mathcal{D}[x(t)] \exp(iS[x(t)]), \quad (2.13)$$

with the action

$$S[x(t)] = \int_0^{t_N} dt L(x(t)) \quad (2.14)$$

and the Lagrange function

$$L(x(t)) = \frac{m}{2} \dot{x}^2(t) - V(x(t)). \quad (2.15)$$

2.1.1 Free Particle

As in Section 2.3 of Ref. [43], consider a free particle of mass m with $\hat{H} = \frac{\hat{p}^2}{2m}$. Due to $V = 0$, the $\mathcal{O}(\Delta t^2)$ terms in Eq. (2.7) vanish and therefore

$$U(x_f, t, x_i, 0) = \left\langle x_f \left| \exp \left(-i \frac{\hat{p}^2}{2m} t \right) \right| x_i \right\rangle = \sqrt{\frac{m}{2\pi i t}} \exp \left(i \frac{m(x_f - x_i)^2}{2t} \right). \quad (2.16)$$

Note that the exponent is given by iS_{cl} with the *classical action* S_{cl} :

$$S_{\text{cl}}[x_{\text{cl}}(s)] = \int_0^t ds L(x_{\text{cl}}(s)) = \frac{m}{2} \int_0^t ds \dot{x}^2(s) = \frac{m(x_f - x_i)^2}{2t} \quad (2.17)$$

with the *classical path* $x_{\text{cl}}(s) = x_i + (x_f - x_i)\frac{s}{t}$, which is the path that solves the Euler-Lagrange equation.

2.1.2 Driven Harmonic Oscillator

Following section 2.7 of Ref. [43], we consider a particle of mass m in an externally driven harmonic potential with the Lagrange function

$$L = \frac{1}{2}m\dot{x}^2 - \frac{1}{2}m\omega^2 x^2 + x f(t). \quad (2.18)$$

We decompose the path of the system into a sum of the classical path and quantum fluctuations $x(s) = x_{\text{cl}}(s) + \zeta(s)$. To compute the propagator $U(x_f, t, x_i, 0)$, we employ the boundary conditions $x_{\text{cl}}(0) = x_i$, $x_{\text{cl}}(t) = x_f$ and $\zeta(0) = \zeta(t) = 0$.

The classical path is determined by the Euler-Lagrange equation, which has the solution (which can be obtained by the multidimensional version of variation of constants):

$$x_{\text{cl}}(s) = x_f \frac{\sin(\omega s)}{\sin(\omega t)} + x_i \frac{\sin(\omega(t-s))}{\sin(\omega t)} + \frac{1}{m\omega} \left[\int_0^s \sin(\omega(s-s')) f(s') ds' - \frac{\sin(\omega s)}{\sin(\omega t)} \int_0^t \sin(\omega(t-s')) f(s') ds' \right]. \quad (2.19)$$

The classical action follows as

$$S_{\text{cl}}[x_{\text{cl}}(s)] = \frac{m\omega}{2\sin(\omega t)} \left[(x_i^2 + x_f^2) \cos(\omega t) - 2x_i x_f \right] + \frac{x_f}{\sin(\omega t)} \int_0^t ds \sin(\omega s) f(s) + \frac{x_i}{\sin(\omega t)} \int_0^t ds \sin(\omega(t-s)) f(s) - \frac{1}{m\omega \sin(\omega t)} \int_0^t ds \int_0^s ds' \sin(\omega s') \sin(\omega(t-s)) f(s') f(s). \quad (2.20)$$

The action of the path $x(s) = x_{\text{cl}}(s) + \xi(s)$ may be represented as

$$S[x(s)] = S_{\text{cl}} - \frac{m}{2} \int_0^t \xi(s) \left(\frac{d^2}{ds^2} + \omega^2 \right) \xi(s) ds, \quad (2.21)$$

where we have made use of partial integration, the boundary conditions on $\xi(s)$, and the Euler-Lagrange equation.

Next, we expand $\xi(s)$ into eigenfunctions $\xi_n(s)$ of the operator $\frac{d^2}{ds^2} + \omega^2$:

$$\xi(s) = \sum_{n=1}^{\infty} a_n \xi_n(s). \quad (2.22)$$

The eigenfunctions that obey $\xi_n(0) = \xi_n(t) = 0$ and orthonormality

$$\langle \xi_n | \xi_m \rangle := \int_0^t \xi_n(s) \xi_m(s) ds = \delta_{nm} \quad (2.23)$$

are given by

$$\xi_n(s) = \sqrt{\frac{2}{t}} \sin\left(n\pi \frac{s}{t}\right) \quad (2.24)$$

with the eigenvalues $\lambda_n = -\left(\frac{n\pi}{t}\right)^2 + \omega^2$.

As they are the eigenfunctions of a self-adjoint operator, they form a basis. In this basis, Eq. (2.21) has the shape

$$S = S_{\text{cl}} - \frac{m}{2} \left\langle \sum_{n=1}^{\infty} a_n \xi_n(s) \left| \sum_{m=1}^{\infty} \lambda_m a_m \xi_m(s) \right. \right\rangle = S_{\text{cl}} - \frac{m}{2} \sum_{n=1}^{\infty} a_n^2 \lambda_n. \quad (2.25)$$

According to Eq. (2.13), the propagator is given by the integral over all possible system paths. Up to a prefactor D caused by the Jacobi determinant of the transformation into the basis of the ξ_n , the propagator is therefore given by

$$\begin{aligned} U(x_f, t, x_i, 0) &= D \int \left(\prod_{n=1}^{\infty} da_n \right) \exp \left(i \left(S_{\text{cl}} - \frac{m}{2} \sum_{n=1}^{\infty} a_n^2 \lambda_n \right) \right) \\ &= D \sqrt{\prod_{n=1}^{\infty} \left(\frac{2\pi}{im\lambda_n} \right)} \exp(iS_{\text{cl}}), \end{aligned} \quad (2.26)$$

where we have executed the integral in the second step. Note that the infinite product is not well-defined, which is due to D also not being well-defined on its own. As the eigenfunctions ξ_n do not depend on ω or $f(s)$, D also cannot depend on them. Thus, we may retrieve it by comparing Eq. (2.26) to the case of the free particle for which we

already know the result (given in Eq. (2.16)). Therefore, the Jacobi determinant must be

$$D = \sqrt{\frac{m}{2\pi it}} \sqrt{\prod_{n=1}^{\infty} \left(\frac{im\lambda_n^{\omega=0}}{2\pi} \right)}. \quad (2.27)$$

Plugging this back into Eq. (2.26), we finally obtain the propagator of the driven harmonic oscillator

$$U(x_f, t, x_i, 0) = \sqrt{\frac{m\omega}{2\pi i \sin(\omega t)}} \exp(iS_{cl}), \quad (2.28)$$

where we have used

$$\prod_{n=1}^{\infty} \frac{\lambda_n^{\omega=0}}{\lambda_n} = \prod_{n=1}^{\infty} \left(\frac{-\left(\frac{n\pi}{t}\right)^2}{-\left(\frac{n\pi}{t}\right)^2 + \omega^2} \right) = \frac{1}{\prod_{n=1}^{\infty} \left(1 - \left(\frac{\omega t}{n\pi}\right)^2 \right)} = \frac{\omega t}{\sin(\omega t)}. \quad (2.29)$$

2.2 Equilibrium Density Matrix

Following section 2.9 of Ref. [43], the equilibrium density matrix in position representation of a system with Hamiltonian \hat{H} that is coupled to a bath of temperature $T = \beta^{-1}$ is given by

$$\rho(x^+, x^-) = \frac{1}{\mathcal{Z}} \langle x^+ | \exp(-\beta\hat{H}) | x^- \rangle \quad (2.30)$$

with the partition function

$$\mathcal{Z} = \int dx \langle x | \exp(-\beta\hat{H}) | x \rangle. \quad (2.31)$$

Note that we can retrieve the equilibrium density matrix from the propagator

$$U(x^+, t, x^-, 0) = \langle x^+ | \exp(-i\hat{H}t) | x^- \rangle \quad (2.32)$$

by the substitution $t \rightarrow -i\beta$.

2.2.1 Harmonic Oscillator

By setting $f(t) = 0$ and replacing $t \rightarrow -i\beta$ in Eq. (2.28) and Eq. (2.20), we straightforwardly obtain the equilibrium density matrix of the harmonic oscillator:

$$\rho(x^+, x^-) = \frac{1}{\mathcal{Z}} \sqrt{\frac{m\omega}{2\pi \sinh(\omega\beta)}} \exp \left[-\frac{m\omega}{2} \frac{(x^{+2} + x^{-2}) \cosh(\omega\beta) - 2x^+x^-}{\sinh \omega\beta} \right] \quad (2.33)$$

with

$$\begin{aligned}
\mathcal{Z} &= \int dx \langle x | \exp(-\beta \hat{H}) | x \rangle \\
&= \sqrt{\frac{m\omega}{2\pi \sinh(\beta\omega)}} \int dx \exp\left(-m\omega \frac{\cosh(\omega\beta) - 1}{\sinh(\omega\beta)} \cdot x^2\right) \\
&= \frac{1}{2 \sinh\left(\frac{\omega\beta}{2}\right)} \tag{2.34}
\end{aligned}$$

and therefore

$$\rho(x^+, x^-) = \sqrt{\frac{m\omega}{\pi} \tanh\left(\frac{\omega\beta}{2}\right)} \exp\left[-\frac{m\omega}{2} \frac{(x^+)^2 + (x^-)^2 \cosh(\omega\beta) - 2x^+x^-}{\sinh \omega\beta}\right]. \tag{2.35}$$

2.3 System-Bath Model

Following Section 3.2 of Ref. [43], we consider the *Caldeira-Leggett model*, which consists of a central system \hat{H}_S that is coupled to an environment of harmonic oscillators such that

$$\hat{H} = \hat{H}_S + \hat{H}_{\text{env}} = \hat{H}_S + \sum_j \left[\frac{\hat{p}_j^2}{2m_j} + \frac{1}{2} m_j \omega_j^2 \left(\hat{x}_j - \frac{c_j \hat{s}}{m_j \omega_j^2} \right)^2 \right] = \hat{H}_S + \sum_j \hat{H}_j, \tag{2.36}$$

where \hat{s} is a "position" operator that only acts on the central system. Although we are only interested in the dynamics of the central system, the bath is modeled explicitly because a time-independent Hamiltonian implies energy conservation. The coupling between central system and environment takes place through the bilinear term $-\hat{s} \sum_j c_j \hat{x}_j$ with coupling strengths c_j to the j -th bath mode. To avoid a qualitative change of the central system potential by the environment, the *counter term*

$$\hat{s}^2 \sum_j \frac{c_j^2}{2m_j \omega_j^2} \tag{2.37}$$

is added such that if the oscillators are located in their potential minimum

$$\hat{x}_j = \frac{c_j \hat{s}}{m_j \omega_j^2}, \tag{2.38}$$

then the harmonic oscillators do not exert a force upon the central system:

$$\frac{\partial \hat{H}}{\partial \hat{s}} = \frac{\partial \hat{H}_S}{\partial \hat{s}}. \tag{2.39}$$

Following Refs. [29, 53], we assume that the coupling between central system and bath is only present for $t > 0$ such that the initial density matrix $W(0)$ factorizes into a system

and a bath part:

$$W(0) = \tilde{\rho}(0) \otimes \rho_{\text{env}}(0). \quad (2.40)$$

We further assume that the bath is initially in thermal equilibrium at temperature $T = \beta^{-1}$, i.e.,

$$\rho_{\text{env}}(0) = \mathcal{Z}_{\text{env}}^{-1} e^{-\beta \hat{H}_{\text{env}}^0} = \prod_j \mathcal{Z}_j^{-1} e^{-\beta \hat{H}_j^0} \quad (2.41)$$

with the bare environment Hamiltonian

$$\hat{H}_{\text{env}}^0 = \sum_j \left(\frac{\hat{p}_j^2}{2m_j} + \frac{1}{2} m_j \omega_j^2 \hat{x}_j^2 \right) =: \sum_j \hat{H}_j^0. \quad (2.42)$$

To compute the *reduced density matrix* $\tilde{\rho}(t)$, which is the density matrix of the central system only, we propagate $W(0)$ in time and then trace out the environment:

$$\begin{aligned} \langle s_f^+ | \tilde{\rho}(t) | s_f^- \rangle &= \int d\mathbf{x}_f ds_i^\pm d\mathbf{x}_i^\pm U(s_f^+ \mathbf{x}_f, t, s_i^+ \mathbf{x}_i^+, 0) \langle s_i^+ \mathbf{x}_i^+ | W(0) | s_i^- \mathbf{x}_i^- \rangle U^\dagger(s_f^- \mathbf{x}_f, t, s_i^- \mathbf{x}_i^-, 0) \\ &= \int d\mathbf{x}_f ds_i^\pm d\mathbf{x}_i^\pm U(s_f^+ \mathbf{x}_f, t, s_i^+ \mathbf{x}_i^+, 0) \langle s_i^+ | \tilde{\rho}(0) | s_i^- \rangle \\ &\quad \cdot \langle \mathbf{x}_i^- | \rho_{\text{env}}(0) | \mathbf{x}_i^+ \rangle U^\dagger(s_f^- \mathbf{x}_f, t, s_i^- \mathbf{x}_i^-, 0), \end{aligned} \quad (2.43)$$

where the vectors \mathbf{x} contain all the coordinates of the harmonic oscillators. From Eq. (2.35) follows that

$$\begin{aligned} \langle \mathbf{x}^+ | \rho_{\text{env}}(0) | \mathbf{x}^- \rangle &= \left\langle \mathbf{x}^+ \left| \prod_j \mathcal{Z}_j^{-1} e^{-\beta \hat{H}_j^0} \right| \mathbf{x}^- \right\rangle = \prod_j \langle x_j^+ | \mathcal{Z}_j^{-1} e^{-\beta \hat{H}_j^0} | x_j^- \rangle \\ &= \prod_j \sqrt{\frac{m_j \omega_j}{\pi}} \tanh\left(\frac{\omega_j \beta}{2}\right) \exp\left[-\frac{m_j \omega_j}{2} \frac{(x_j^{+2} + x_j^{-2}) \cosh(\omega_j \beta) - 2x_j^+ x_j^-}{\sinh \omega_j \beta}\right]. \end{aligned} \quad (2.44)$$

In accordance with Eq. (2.13), we rewrite the propagators in Eq. (2.43) as the path integral

$$\begin{aligned} \langle s_f^+ | \tilde{\rho}(t) | s_f^- \rangle &= \int d\mathbf{x}_f ds_i^\pm d\mathbf{x}_i^\pm \int_{s^+(0)=s_i^+}^{s^+(t)=s_f^+} \mathcal{D}s^+ \int_{\mathbf{x}^+(0)=\mathbf{x}_i^+}^{\mathbf{x}^+(t)=\mathbf{x}_f} \mathcal{D}\mathbf{x}^+ \exp(iS[\mathbf{x}^+, s^+]) \langle s_i^+ | \tilde{\rho}(0) | s_i^- \rangle \\ &\quad \cdot \langle \mathbf{x}_i^+ | \rho_{\text{env}}(0) | \mathbf{x}_i^- \rangle \int_{s^-(0)=s_i^-}^{s^-(t)=s_f^-} \mathcal{D}s^- \int_{\mathbf{x}^-(0)=\mathbf{x}_i^-}^{\mathbf{x}^-(t)=\mathbf{x}_f} \mathcal{D}\mathbf{x}^- \exp(-iS[\mathbf{x}^-, s^-]) \\ &= \int ds_i^\pm \int \mathcal{D}s^\pm \exp[i(S_S[s^+] - S_S[s^-])] \langle s_i^+ | \tilde{\rho}(0) | s_i^- \rangle \\ &\quad \cdot \int d\mathbf{x}_f d\mathbf{x}_i^\pm \langle \mathbf{x}_i^+ | \rho_{\text{env}}(0) | \mathbf{x}_i^- \rangle \int \mathcal{D}\mathbf{x}^\pm \exp[i(S_{\text{env}}[s^+, \mathbf{x}^+] - S_{\text{env}}[s^-, \mathbf{x}^-])] \\ &= \int ds_i^\pm \int \mathcal{D}s^\pm \exp[i(S_S[s^+] - S_S[s^-])] \langle s_i^+ | \tilde{\rho}(0) | s_i^- \rangle \mathcal{F}_{\text{FV}}[s^+, s^-]. \end{aligned} \quad (2.45)$$

The Feynman-Vernon influence functional $\mathcal{F}_{\text{FV}}[s^+, s^-]$ (see Ref. [6]) fully characterizes the influence of the environment on the system and is defined as

$$\begin{aligned}\mathcal{F}_{\text{FV}}[s^+, s^-] &= \int d\mathbf{x}_f d\mathbf{x}_i^\pm \langle \mathbf{x}_i^+ | \rho_{\text{env}}(0) | \mathbf{x}_i^- \rangle \int \mathcal{D}\mathbf{x}^\pm \exp [i(S_{\text{env}}[s^+, \mathbf{x}^+] - S_{\text{env}}[s^-, \mathbf{x}^-])] \\ &= \int d\mathbf{x}_f d\mathbf{x}_i^\pm \langle \mathbf{x}_i^+ | \rho_{\text{env}}(0) | \mathbf{x}_i^- \rangle \prod_j \int \mathcal{D}x_j^+ \exp(iS_j[s^+, x_j^+]) \int \mathcal{D}x_j^- \exp(-iS_j[s^-, x_j^-])\end{aligned}\quad (2.46)$$

due to $S_{\text{env}} = \sum_j S_j$. We may retrieve the results of the last two path integrals, which are the propagators corresponding to the Hamiltonians

$$H_j = \frac{\hat{p}_j^2}{2m_j} + \frac{1}{2}m_j\omega_j^2\hat{x}_j^2 - c_jx_j\hat{s} + \frac{c_j^2\hat{s}^2}{2m_j\omega_j^2}\quad (2.47)$$

by comparing with our results from section 2.1.2. Namely, we interpret the system path $s(t')$ as an external driving and identify

$$f(t') = c_js(t').\quad (2.48)$$

The additional driving term

$$\frac{c_j^2s(t')^2}{2m_j\omega_j^2}\quad (2.49)$$

does not enter the Euler-Lagrange equation as it does not depend on x_j or \dot{x}_j . In fact, it only enters straightforwardly in the classical action, which becomes

$$\begin{aligned}S_{\text{cl}}[s, x_{\text{cl}}] &= \frac{m_j\omega_j}{2\sin(\omega_j t)} [(x_{i,j}^2 + x_{f,j}^2) \cos(\omega_j t) - 2x_{i,j}x_{f,j}] \\ &+ \frac{x_{f,j}c_j}{\sin(\omega_j t)} \int_0^t dt' \sin(\omega_j t')s(t') + \frac{x_{i,j}c_j}{\sin(\omega_j t)} \int_0^t dt' \sin(\omega_j(t-t'))s(t') \\ &- \frac{c_j^2}{m_j\omega_j \sin(\omega_j t)} \int_0^t dt' \int_0^{t'} dt'' \sin[\omega_j(t-t')] \sin(\omega_j t'')s(t')s(t'') \\ &- \frac{c_j^2}{2m_j\omega_j^2} \int_0^t dt' s^2(t').\end{aligned}\quad (2.50)$$

So we have according to Eq. (2.28)

$$\int \mathcal{D}x_j \exp(iS_j[s, x_j]) = \sqrt{\frac{m_j\omega_j}{2\pi i \sin(\omega_j t)}} \exp(iS_{\text{cl}}[s, x_{\text{cl}}]).\quad (2.51)$$

Inserting Eq. (2.51) and its complex conjugate as well as Eq. (2.44) into Eq. (2.46) yields

$$\begin{aligned}
\mathcal{F}_{\text{FV}}[s^+, s^-] &= \int dx_f dx_i^\pm \prod_j \sqrt{\frac{m_j \omega_j}{\pi} \tanh\left(\frac{\omega_j \beta}{2}\right)} \frac{m_j \omega_j}{2\pi \sin(\omega_j t)} \\
&\cdot \exp \left[-\frac{m_j \omega_j (x_{i,j}^{+2} + x_{i,j}^{-2}) \cosh(\omega_j \beta) - 2x_{i,j}^+ x_{i,j}^-}{\sinh \omega_j \beta} + iS_{\text{cl}}[s^+, x_{j,\text{cl}}^+] - iS_{\text{cl}}[s^-, x_{j,\text{cl}}^-] \right] \\
&= \int dx_f dx_i^\pm \prod_j \sqrt{\frac{m_j \omega_j}{\pi} \tanh\left(\frac{\omega_j \beta}{2}\right)} \frac{m_j \omega_j}{2\pi \sin(\omega_j t)} \\
&\cdot \exp \left[-\frac{1}{2} \begin{pmatrix} x_{f,j} \\ x_{i,j}^+ \\ x_{i,j}^- \end{pmatrix}^\top \cdot A_j \cdot \begin{pmatrix} x_{f,j} \\ x_{i,j}^+ \\ x_{i,j}^- \end{pmatrix} + \mathbf{J}_j \cdot \begin{pmatrix} x_{f,j} \\ x_{i,j}^+ \\ x_{i,j}^- \end{pmatrix} \right. \\
&- i \frac{c_j^2}{m_j \omega_j \sin(\omega_j t)} \int_0^t dt' \int_0^{t'} dt'' \sin[\omega_j(t-t')] \sin(\omega_j t'') [s^+(t')s^+(t'') - s^-(t')s^-(t'')] \\
&\left. - i \frac{c_j^2}{2m_j \omega_j^2} \int_0^t dt' [s^{+2}(t') - s^{-2}(t')] \right] \quad (2.52)
\end{aligned}$$

where

$$A_j = m_j \omega_j \begin{pmatrix} 0 & \frac{i}{\sin(\omega_j t)} & \frac{-i}{\sin(\omega_j t)} \\ \frac{i}{\sin(\omega_j t)} & \coth(\omega_j \beta) - i \cot(\omega_j t) & \frac{-1}{\sinh(\omega_j \beta)} \\ \frac{-i}{\sin(\omega_j t)} & \frac{-1}{\sinh(\omega_j \beta)} & \coth(\omega_j \beta) + i \cot(\omega_j t) \end{pmatrix}, \quad (2.53)$$

$$\det(A_j) = \frac{2(m_j \omega_j)^3 \tanh\left(\frac{\omega_j \beta}{2}\right)}{\sin^2(\omega_j t)}, \quad (2.54)$$

$$A_j^{-1} = \frac{1}{2m_j \omega_j} \begin{pmatrix} \coth(\omega_j \beta/2) & \cos(\omega_j t) - i & \cos(\omega_j t) + i \\ \cos(\omega_j t) - i & \coth(\omega_j \beta/2) & \coth(\omega_j \beta/2) \\ \cos(\omega_j t) + i & \coth(\omega_j \beta/2) & \coth(\omega_j \beta/2) \end{pmatrix}, \quad (2.55)$$

$$\mathbf{J}_j = i \cdot \frac{c_j}{\sin(\omega_j t)} \int_0^t dt' \begin{pmatrix} \sin(\omega_j t') [s^+(t') - s^-(t')] \\ \sin(\omega_j(t-t')) s^+(t') \\ \sin(\omega_j(t-t')) s^-(t') \end{pmatrix}. \quad (2.56)$$

By use of the identity (see Ref. [54])

$$\int \exp\left(-\frac{1}{2} \mathbf{x}^\top \cdot A \cdot \mathbf{x} + \mathbf{J} \cdot \mathbf{x}\right) d^3 \mathbf{x} = \sqrt{\frac{(2\pi)^3}{\det A}} \exp\left(\frac{1}{2} \mathbf{J} \cdot A^{-1} \cdot \mathbf{J}\right), \quad (2.57)$$

we are left with

$$\mathcal{F}_{\text{FV}}[s^+, s^-] = \exp(-\Phi_{\text{FV}}[s^+, s^-]), \quad (2.58)$$

where

$$\begin{aligned}
\Phi_{\text{FV}}[s^+, s^-] &= \sum_j \frac{c_j^2}{2m_j\omega_j} \left(\int_0^t dt' \int_0^{t'} dt'' [s^+(t') - s^-(t')] \right. \\
&\quad \cdot \left. \left\{ \coth\left(\frac{\omega_j\beta}{2}\right) \cos(\omega_j(t' - t'')) [s^+(t'') - s^-(t'')] \right. \right. \\
&\quad \left. \left. - i \sin(\omega_j(t' - t'')) [s^+(t'') - s^-(t'')] \right\} + i \frac{1}{\omega_j} \int_0^t dt' [s^{+2}(t') - s^{-2}(t')] \right) \\
&= \int_0^t dt' \int_0^{t'} dt'' [s^+(t') - s^-(t')] [\eta(t' - t'')s^+(t'') - \eta^*(t' - t'')s^-(t'')]
\end{aligned} \tag{2.59}$$

and

$$\eta(t) = L(t) + i\delta(t) \frac{2}{\pi} \int_0^\infty d\omega \frac{J(\omega)}{\omega} \tag{2.60}$$

with the *bath autocorrelation function*

$$L(t) = \frac{1}{\pi} \int_0^\infty d\omega J(\omega) \left[\coth\left(\frac{\omega\beta}{2}\right) \cos(\omega t) - i \sin(\omega t) \right] \tag{2.61}$$

and the *bath spectral density*

$$J(\omega) = \frac{\pi}{2} \sum_j \frac{c_j^2}{m_j\omega_j} \delta(\omega - \omega_j). \tag{2.62}$$

This notation straightforwardly allows us to take the bath continuum limit by specifying a continuous spectral density.

2.4 Discretizing the Path Integral

In order to compute the dynamics of the reduced density matrix in the system-bath model according to Eq. (2.45), we discretize the central system path integral. The analytical result for the Feynman-Vernon influence functional in Eq. (2.58) thereby turns into a discrete sum over all possible central system paths that can be evaluated numerically. This requires \hat{H}_S to be either a discrete system of n states or a discretized continuous system such that the observable \hat{s} has eigenvalues $\{s_1, s_2, \dots, s_n\}$. Following the presentation of Ref. [29] (but using the modified Trotter splitting of Ref. [45]) of the original QUAPI method [8, 9], one assumes that \hat{H} is time-independent (although time-independence is not strictly required for QUAPI, it is chosen here for ease of notation) such that its prop-

agator can be decomposed as:

$$\hat{U} = e^{-i\hat{H}t} = \prod_{j=1}^{N+1} e^{-i\hat{H}\Delta t} \approx e^{-i\hat{H}_S \frac{\Delta t}{2}} \left(\prod_{j=1}^N e^{-i\hat{H}_{\text{env}}\Delta t} e^{-i\hat{H}_S\Delta t} \right) e^{-i\hat{H}_{\text{env}}\Delta t} e^{-i\hat{H}_S \frac{\Delta t}{2}} \quad (2.63)$$

with $t = (N + 1) \cdot \Delta t$ and using the symmetric Trotter splitting:

$$e^{-i\hat{H}\Delta t} = e^{-i\hat{H}_S \frac{\Delta t}{2}} e^{-i\hat{H}_{\text{env}}\Delta t} e^{-i\hat{H}_S \frac{\Delta t}{2}} + \mathcal{O}(\Delta t^3). \quad (2.64)$$

The error introduced in Eq. (2.63) is therefore of order

$$(N + 1) \cdot \mathcal{O}(\Delta t^3) = t \cdot \mathcal{O}(\Delta t^2). \quad (2.65)$$

The completeness relation is given by

$$\mathbb{1}_{(k)} = \sum_{i_k=1}^n |s_{i_k}\rangle \langle s_{i_k}| \int d\mathbf{x}_k |\mathbf{x}_k\rangle \langle \mathbf{x}_k| \quad (2.66)$$

with the eigenstates $|s_i\rangle$ of \hat{s} and the eigenstates $|\mathbf{x}\rangle$ of all the harmonic oscillators. The index k will be used to discriminate between multiple insertions of the completeness relation. Switching to coordinate representation, we separate out the first and last half-step of the central system dynamics in Eq. (2.63):

$$\begin{aligned} U(s_{i_{N+1}}, \mathbf{x}_{N+1}; s_{i_0}, \mathbf{x}_0) &= \langle s_{i_{N+1}}, \mathbf{x}_{N+1} | \hat{U} | s_{i_0}, \mathbf{x}_0 \rangle \\ &= \sum_{i_{N+1/2}, i_{1/2}=1}^n \left\langle s_{i_{N+1}}, \mathbf{x}_{N+1} \left| e^{-i\hat{H}_S \frac{\Delta t}{2}} \right| s_{i_{N+1/2}} \right\rangle \\ &\cdot \left\langle s_{i_{N+1/2}} \left| \left(\prod_{j=1}^N e^{-i\hat{H}_{\text{env}}\Delta t} e^{-i\hat{H}_S\Delta t} \right) e^{-i\hat{H}_{\text{env}}\Delta t} \right| s_{i_{1/2}} \right\rangle \left\langle s_{i_{1/2}} \left| e^{-i\hat{H}_S \frac{\Delta t}{2}} \right| s_{i_0}, \mathbf{x}_0 \right\rangle \\ &= \sum_{i_{N+1/2}, i_{1/2}=1}^n \left\langle s_{i_{N+1}}, \mathbf{x}_{N+1} \left| e^{-i\hat{H}_S \frac{\Delta t}{2}} \right| s_{i_{N+1/2}} \right\rangle U(s_{i_{N+1/2}}, \mathbf{x}_{N+1}; s_{i_{1/2}}, \mathbf{x}_0) \left\langle s_{i_{1/2}} \left| e^{-i\hat{H}_S \frac{\Delta t}{2}} \right| s_{i_0}, \mathbf{x}_0 \right\rangle. \end{aligned} \quad (2.67)$$

Next, we insert the completeness relation after every time-step:

$$\begin{aligned} U(s_{i_{N+1/2}}, \mathbf{x}_{N+1}; s_{i_{1/2}}, \mathbf{x}_0) &= \left\langle s_{i_{N+1/2}}, \mathbf{x}_{N+1} \left| \prod_{j=1}^N \left(e^{-i\hat{H}_{\text{env}}\Delta t} e^{-i\hat{H}_S\Delta t} \mathbb{1}_{(N+1-j)} \right) e^{-i\hat{H}_{\text{env}}\Delta t} \right| s_{i_{1/2}}, \mathbf{x}_0 \right\rangle \\ &= \sum_{i_{3/2}, \dots, i_{N+1/2}=1}^n \left\langle s_{i_{N+1/2}} \left| e^{-i\hat{H}_S\Delta t} \right| s_{i_{N-1/2}} \right\rangle \cdot \dots \cdot \left\langle s_{i_{3/2}} \left| e^{-i\hat{H}_S\Delta t} \right| s_{i_{1/2}} \right\rangle \\ &\cdot \int d\mathbf{x}_N, \dots, d\mathbf{x}_1 \left\langle \mathbf{x}_{N+1} \left| e^{-i\hat{H}_{\text{env}}(s_{i_{N-1/2}})\Delta t} \right| \mathbf{x}_N \right\rangle \cdot \dots \cdot \left\langle \mathbf{x}_1 \left| e^{-i\hat{H}_{\text{env}}(s_{i_{1/2}})\Delta t} \right| \mathbf{x}_0 \right\rangle. \end{aligned} \quad (2.68)$$

As the only system operator that \hat{H}_{env} depends on is \hat{s} , the $|s_i\rangle$ can be drawn past the bath time evolution operators while replacing \hat{s} by the corresponding eigenvalue s_i .

This leads to the discretized *path distributions*

$$\begin{aligned} \tilde{s}^\pm(t) = & s_{i_{1/2}^\pm} \cdot \left(1 - \theta \left[t - \frac{3\Delta t}{2} \right] \right) + \sum_{j=1}^{N-1} \left\{ s_{i_{j+1/2}^\pm} \left(\theta \left[t - \left(j + \frac{1}{2} \right) \Delta t \right] - \theta \left[t - \left(j + \frac{3}{2} \right) \Delta t \right] \right) \right\} \\ & + s_{i_{N+1/2}^\pm} \cdot \theta \left[t - \left(N - \frac{1}{2} \right) \Delta t \right], \end{aligned} \quad (2.69)$$

with the Heaviside function $\theta(t)$. It is also useful to define the *antisymmetric path distribution* $\zeta(t) = \tilde{s}^+ - \tilde{s}^-$. The derivatives of the path distributions are

$$\dot{\zeta}(t) = \sum_{j=0}^N \left[s_{i_{j+3/2}^+} - s_{i_{j+3/2}^-} - \left(s_{i_{j+1/2}^+} - s_{i_{j+1/2}^-} \right) \right] \delta \left(t - \left(j + \frac{1}{2} \right) \Delta t \right), \quad (2.70)$$

$$\dot{\tilde{s}}^\pm(t) = \sum_{j=0}^N \left[s_{i_{j+3/2}^\pm} - s_{i_{j+1/2}^\pm} \right] \delta \left(t - \left(j + \frac{1}{2} \right) \Delta t \right). \quad (2.71)$$

Similarly to Ref. [50], we define the *reduced propagator* $U_{i_{N+1/2}^\pm, i_{1/2}^\pm}^{(N+1/2, 1/2)}$, which has the property of relating the reduced density matrix at $t = \Delta t/2$ to the reduced density matrix at time $(N + 1/2)\Delta t$ by a matrix multiplication:

$$\tilde{\rho}_{i_{N+1/2}^\pm}^{(N+1/2)} = \sum_{i_{1/2}^\pm} U_{i_{N+1/2}^\pm, i_{1/2}^\pm}^{(N+1/2, 1/2)} \tilde{\rho}_{i_{1/2}^\pm}^{(1/2)}. \quad (2.72)$$

By comparing Eqs. (2.68), (2.43), and (2.45), we find that

$$\begin{aligned} U_{i_{N+1/2}^\pm, i_{1/2}^\pm}^{(N+1/2, 1/2)} &= \int d\mathbf{x}_{N+1} d\mathbf{x}_0^\pm U(s_{i_{N+1/2}^+}, \mathbf{x}_{N+1}; s_{i_{1/2}^+}, \mathbf{x}_0^+) \langle \mathbf{x}_0^+ | \rho_{\text{env}} | \mathbf{x}_0^- \rangle U^\dagger(s_{i_{N+1/2}^-}, \mathbf{x}_{N+1}; s_{i_{1/2}^-}, \mathbf{x}_0^-) \\ &= \sum_{i_{3/2}^\pm, \dots, i_{N+1/2}^\pm=1}^n \left\langle s_{i_{N+1/2}^+}^+ \left| e^{-i\hat{H}_S \Delta t} \right| s_{i_{N-1/2}^+}^+ \right\rangle \cdots \left\langle s_{i_{3/2}^+}^+ \left| e^{-i\hat{H}_S \Delta t} \right| s_{i_{1/2}^+}^+ \right\rangle \\ &\quad \cdot \left\langle s_{i_{1/2}^-}^- \left| e^{i\hat{H}_S \Delta t} \right| s_{i_{3/2}^-}^- \right\rangle \cdots \left\langle s_{i_{N-1/2}^-}^- \left| e^{i\hat{H}_S \Delta t} \right| s_{i_{N+1/2}^-}^- \right\rangle \mathcal{F}_{\text{FV}}[s^+, s^-]. \end{aligned} \quad (2.73)$$

Partially integrating Eq. (2.59) twice to make it dependent on the derivatives of the path distributions containing delta functions yields

$$\begin{aligned} \Phi_{\text{FV}} = & - \int_{\Delta t/2}^{(N+1/2)\Delta t} dt' \int_{\Delta t/2}^{t'} dt'' \dot{\zeta}(t'') [Q(t' - t'') \dot{\tilde{s}}^+(t'') - Q^*(t' - t'') \dot{\tilde{s}}^-(t'')] \\ & + \dot{\zeta}(t) \int_{\Delta t/2}^{(N+1/2)\Delta t} dt' [Q(t - t') \dot{\tilde{s}}^+(t') - Q^*(t - t') \dot{\tilde{s}}^-(t')] \\ & + \dot{\zeta}(t) [Q(t) \tilde{s}^+(0) - Q^*(t) \tilde{s}^-(0)] - \int_{\Delta t/2}^{(N+1/2)\Delta t} dt' \dot{\zeta}(t') [Q(t') \tilde{s}^+(0) - Q^*(t') \tilde{s}^-(0)], \end{aligned} \quad (2.74)$$

where we have used the second antiderivative of $L(t)$ as

$$Q(t) = \frac{1}{\pi} \int_0^\infty d\omega \frac{J(\omega)}{\omega^2} \left[\coth\left(\frac{\omega\beta}{2}\right) (1 - \cos(\omega t)) + i(\sin(\omega t) - \omega t) \right], \quad (2.75)$$

with $Q(0) = 0 = \dot{Q}(0)$, which is very similar to what is referred to as the pair correlation function in the literature [55]. Plugging Eqs. (2.70) and (2.71) into Eq. (2.74) yields

$$\Phi_{FV} = \sum_{k=0}^N \sum_{k'=0}^k (s_{i_{k+1/2}^+} - s_{i_{k+1/2}^-}) \left(\eta_{kk'} s_{i_{k'+1/2}^+} - \eta_{kk'}^* s_{i_{k'+1/2}^-} \right), \quad (2.76)$$

with the coefficients

$$\eta_{kk} = Q(\Delta t) \quad (2.77)$$

$$\eta_{kk'} = Q((k - k' - 1)\Delta t) + Q((k - k' + 1)\Delta t) - 2Q((k - k')\Delta t), \quad (2.78)$$

where $k' < k$. While the "local" terms η_{kk} just depend on $Q(t)$, the remaining "nonlocal" terms depend on the discretized second derivative of $Q(t)$, which is approximately related to $L(t)$ by

$$\eta_{kk'} \approx \Delta t^2 L((k - k')\Delta t). \quad (2.79)$$

As a shorthand notation, we define the *forward-backward system propagator*:

$$G_{i_{j+1/2}^\pm i_{j-1/2}^\pm} = \left\langle s_{i_{j+1/2}^+} \left| e^{-i\hat{H}_S \Delta t} \right| s_{i_{j-1/2}^+} \right\rangle \left\langle s_{i_{j-1/2}^-} \left| e^{i\hat{H}_S \Delta t} \right| s_{i_{j+1/2}^-} \right\rangle \quad (2.80)$$

and the terms contained in the discretized influence functional

$$F_{i_{k+1/2}^\pm i_{k'+1/2}^\pm}^{(k+1/2, k'+1/2)} = \exp \left[- (s_{i_{k+1/2}^+} - s_{i_{k+1/2}^-}) \left(\eta_{kk'} s_{i_{k'+1/2}^+} - \eta_{kk'}^* s_{i_{k'+1/2}^-} \right) \right]. \quad (2.81)$$

The forward-backward system propagator of Eq. (2.80) can be computed by analytically or numerically solving the Schrödinger equation.

With this, we arrive at

$$U_{i_{N+1/2}^\pm i_{1/2}^\pm}^{(N+1/2, 1/2)} = \sum_{i_{3/2}^\pm, \dots, i_{N-1/2}^\pm} \prod_{j=1}^N \left(G_{i_{j+1/2}^\pm i_{j-1/2}^\pm}^{(j+1/2, j-1/2)} \right) \prod_{k=0}^N \prod_{k'=0}^k F_{i_{k+1/2}^\pm i_{k'+1/2}^\pm}^{(k+1/2, k'+1/2)} \quad (2.82)$$

for the reduced propagator and from it trivially follows the reduced density matrix

$$\tilde{\rho}_{i_{N+1}^\pm}^{(N+1)} = \sum_{i_0^\pm, i_{1/2}^\pm, \dots, i_{N+1/2}^\pm} G_{i_{N+1}^\pm i_{N+1/2}^\pm}^{(N+1, N+1/2)} G_{i_{1/2}^\pm i_0^\pm}^{(1/2, 0)} \tilde{\rho}_{i_0^\pm}^{(0)} \prod_{j=1}^N \left(G_{i_{j+1/2}^\pm i_{j-1/2}^\pm}^{(j+1/2, j-1/2)} \right) \prod_{k=0}^N \prod_{k'=0}^k F_{i_{k+1/2}^\pm i_{k'+1/2}^\pm}^{(k+1/2, k'+1/2)}. \quad (2.83)$$

To simplify the notation of Eq. (2.82), we rename the indices such that the reduced propagator becomes

$$U_{i_N^\pm, i_0^\pm}^{(N0)} = \sum_{i_1^\pm, \dots, i_{N-1}^\pm} \prod_{j=1}^N \left(G_{i_j^\pm, i_{j-1}^\pm}^{(j, j-1)} \right) \prod_{k=0}^N \prod_{k'=0}^k F_{i_k^\pm, i_{k'}^\pm}^{(k, k')}. \quad (2.84)$$

Now, we can in principle already numerically evaluate this expression. Unfortunately, as the influence functional terms couple each time-step to all previous time-steps as depicted in Fig. 2.1, Eq. (2.84) can in general not be evaluated iteratively, but instead requires summation of $n^{2(N+1)}$ terms (for each of the n^4 elements of $U_{\alpha_N \alpha_0}$, a sum of $n^{2(N-1)}$ terms has to be computed), which makes long-time propagation by direct evaluation of this expression infeasible. While originally an iterative evaluation of Eq. (2.82) based on a memory cutoff $\eta_{kk'} \approx 0$ for $k - k' > \Delta k_{\max}$ as presented in section 2.7 has been used [8, 9], this thesis exclusively uses a tensor network approach to evaluate the path sum, which will be introduced in chapter 3.

2.5 Polarized Initial Conditions

Instead of using the unpolarized initial condition of the bath (Eq. (2.41)), one can also consider the case where the bath is equilibrated to an initially polarized system such that

$$\rho_{\text{env}}(0) \propto e^{-\beta \hat{H}_{\text{env}}(\hat{s}=1)}. \quad (2.85)$$

This density matrix is obtained in complete analogy to Section 2.2.1, but with $f(t) = 1$ instead of $f(t) = 0$, and then plugged into Eq. (2.44). After discretization, one obtains the additional factors

$$\prod_{k>0} \tilde{F}_{i_k^\pm, i_0^\pm}^{(k,0)} = \prod_{k>0} \exp \left[\frac{i}{2} (s_{i_k^+} - s_{i_k^-}) \tilde{\eta}_{k0} \right] \quad (2.86)$$

in Eq. (2.84), where

$$\tilde{\eta}_{k0} = 2 \int_0^\infty \frac{J(\omega)}{\omega^2} [\sin(\omega k \Delta t) - \sin(\omega(k-1)\Delta t)] d\omega. \quad (2.87)$$

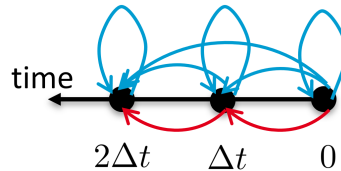


Figure 2.1: Graphical representation of the path sum in Eq. (2.84) for $N = 3$. System propagator terms G are colored in red, influence functional terms F are colored in blue.

Note the typo in the definition of $\tilde{\eta}_{k0}$ in Ref. [23], where this calculation has previously been performed.

2.6 Blip Decomposition

As in Ref. [44], we consider the change of basis

$$\Delta s_k := s_{i_{k+1/2}^+} - s_{i_{k+1/2}^-} \quad (2.88)$$

$$\bar{s}_k := \frac{1}{2} \left(s_{i_{k+1/2}^+} + s_{i_{k+1/2}^-} \right). \quad (2.89)$$

The configuration $\Delta s_k = 0$ is referred to as a *sojourn* and $\Delta s_k \neq 0$ as a *blip*. In this basis, Eq. (2.81) becomes

$$F_{i_{k+1/2}^\pm, i_{k'+1/2}^\pm}^{(k+1/2, k'+1/2)} = \exp \left[-\Delta s_k \left(\text{Re}(\eta_{kk'}) \Delta s_{k'} + 2i \text{Im}(\eta_{kk'}) \bar{s}_{k'} \right) \right]. \quad (2.90)$$

The advantage of this basis is that only blips are coupled to previous times while sojourns decouple from all previous times.

Eq. (2.84) then becomes

$$U_{i_N^\pm, i_0^\pm}^{(N0)} = \sum_{\Delta s_1} \dots \sum_{\Delta s_{N-1}} \sum_{\bar{s}_1} \dots \sum_{\bar{s}_{N-1}} G_{i_N^\pm, i_{N-1}^\pm} \cdot \dots \cdot G_{i_1^\pm, i_0^\pm} \exp \left[- \sum_{k=0}^N \sum_{k'=0}^k \Delta s_k \left(\text{Re}(\eta_{kk'}) \Delta s_{k'} + 2i \text{Im}(\eta_{kk'}) \bar{s}_{k'} \right) \right]. \quad (2.91)$$

For example, in the case $n = 2$ and $s_{i_k^\pm} \in \{1, -1\}$, we have $\Delta s_k \in \{0, 2, -2\}$ and

$$\bar{s}_k \in \begin{cases} \{0\} & \text{if } \Delta s_k = \pm 2 \\ \{1, -1\} & \text{if } \Delta s_k = 0 \end{cases}.$$

Note that therefore the sum over \bar{s}_k depends on the outer sum over Δs_k . For each of the $(n^2 - 1)^{N-1}$ combinations of $\Delta s_1, \Delta s_2, \dots, \Delta s_{N-1}$, the inner term of Eq. (2.91) may be written as

$$\exp \left[- \sum_{k=0}^N \sum_{k'=0}^k \Delta s_k \text{Re}(\eta_{kk'}) \Delta s_{k'} \right] \sum_{\bar{s}_{N-1}} G_{i_N^\pm, i_{N-1}^\pm} e^{i(\sum_{j>N-1} \omega_{j,N-1}) \bar{s}_{N-1}} \dots \sum_{\bar{s}_k} G_{i_{k+1}^\pm, i_k^\pm} e^{i(\sum_{j>k} \omega_{j,k}) \bar{s}_k} \dots \cdot \sum_{\bar{s}_1} G_{i_2^\pm, i_1^\pm} e^{i(\sum_{j>1} \omega_{j,1}) \bar{s}_1} G_{i_1^\pm, i_0^\pm} e^{i(\sum_{j>0} \omega_{j,0}) \bar{s}_0} \quad (2.92)$$

with $\omega_{k,k'} = -2\Delta s_k \text{Im}(\eta_{kk'})$. The evaluation of this inner term is very efficient since it only requires a maximum of $N - 1$ sums over n terms. Compared to Eq. (2.84), the exact blip decomposition enables a reduction of the computational effort by a factor of $\sim \left(\frac{n^2 - 1}{n^2} \right)^N$ and is therefore most useful for systems with few states.

In Ref. [44], an approximation valid for systems with a strong coupling to the bath reduces the computational effort even more dramatically. There, the number of blips that are summed over in the outer sum is treated as a convergence parameter.

2.7 Iterative QUAPI

In order to tame the exponential scaling of the path sum in Eq. (2.84), Makri and Makarov [8, 9] have introduced a memory cut-off, which is a controlled approximation assuming that the influence functional terms connecting times far apart from each other become negligible. This leads to the iterative QUAPI method, which will be explained in detail in the following.

The memory cut-off is justified when the bath autocorrelation function Eq. (2.61) falls off sufficiently quickly in time. The latter implies $\eta_{kk'} \approx 0$ for $k - k' > k_{\max}$ because of Eq. (2.79) and thus $F^{(k,k')} \approx 0$ in Eq. (2.84). For notational convenience, we ignore the initial and final half time-step and omit the subscripts as they follow from the superscripts. Then, the reduced density matrix at time $N \cdot \Delta t$ is given by

$$\tilde{\rho}^{(N)} = \sum_{0,1,\dots,N-1} \prod_{j=1}^N \left(G^{(j,j-1)} \right) \prod_{k'=0}^N \prod_{k''=\max(0,k'-k_{\max})}^{k'} \left(F^{(k',k'')} \right) \tilde{\rho}^{(0)}. \quad (2.93)$$

Consider the case $k_{\max} = 1$. We define the *reduced density tensor*

$$A^{(1)} = \sum_0 G^{(10)} F^{(11)} F^{(10)} F^{(00)} \tilde{\rho}^{(0)}, \quad (2.94)$$

which coincides with the reduced density matrix $\tilde{\rho}^{(1)}$ at time $t = \Delta t$. Note that this is more complicated in the original publication Ref. [9] as there the Trotter splitting is made such that the initial and final half time-steps are taken with respect to the bath Hamiltonian. For the next time-step, we may write

$$\begin{aligned} A^{(2)} &= \sum_1 \sum_0 G^{(21)} G^{(10)} F^{(22)} F^{(21)} F^{(11)} F^{(10)} F^{(00)} \tilde{\rho}^{(0)} \\ &= \sum_1 G^{(21)} F^{(22)} F^{(21)} \sum_0 G^{(10)} F^{(11)} F^{(10)} F^{(00)} \tilde{\rho}^{(0)} \\ &= \sum_1 \Lambda^{(21)} A^{(1)} \end{aligned} \quad (2.95)$$

with

$$\Lambda^{(k+1,k)} = G^{(k+1,k)} F^{(k+1,k+1)} F^{(k+1,k)}. \quad (2.96)$$

Note that we can perform the summation over the 0-th index in $A^{(1)}$ already and still compute $A^{(2)}$ from it due to the absence of $F^{(20)}$. Iterating this procedure allows to com-

pute A at arbitrary times:

$$A^{(k+1)} = \sum_k \Lambda^{(k+1,k)} A^{(k)}. \quad (2.97)$$

The corresponding reduced density matrix is then given by

$$\tilde{\rho}^{(k)} = A^{(k)}. \quad (2.98)$$

Note that setting $k_{\max} = 1$ allowed us to decompose the summation over n^{2N} terms of Eq. (2.93) into N matrix-vector multiplications of $n^2 \times n^2$ matrices with vectors of dimension n^2 .

Now consider the case $k_{\max} = 2$. Similarly as before, we define

$$A^{(10)} = G^{(10)} F^{(11)} F^{(10)} F^{(00)} \tilde{\rho}^{(0)}, \quad (2.99)$$

which allows us to write

$$A^{(21)} = \sum_0 \Lambda^{(210)} A^{(10)} \quad (2.100)$$

with

$$\Lambda^{(k+1,k,k-1)} = G^{(k+1,k)} F^{(k+1,k+1)} F^{(k+1,k)} F^{(k+1,k-1)}, \quad (2.101)$$

giving the iterative procedure

$$A^{(k+1,k)} = \sum_{k-1} \Lambda^{(k+1,k,k-1)} A^{(k,k-1)}, \quad (2.102)$$

and the reduced density matrix

$$\tilde{\rho}^{(k)} = \sum_{k,k-1} A^{(k,k-1)}. \quad (2.103)$$

This scheme is straightforwardly extended to arbitrary k_{\max} with the initial condition

$$A^{(k_{\max}-1, k_{\max}-2, \dots, 0)} = \prod_{j=1}^{k_{\max}-1} \left(G^{(j,j-1)} \right) \prod_{k'=0}^{k_{\max}-1} \prod_{k''=0}^{k'} \left(F^{(k'k'')} \right) \tilde{\rho}^{(0)}, \quad (2.104)$$

and the iterative procedure

$$A^{(k+1, k, \dots, k+2-k_{\max})} = \sum_{k+1-k_{\max}} \Lambda^{(k+1, k, \dots, k+1-k_{\max})} A^{(k, k-1, \dots, k+1-k_{\max})} \quad (2.105)$$

with

$$\Lambda^{(k+1,k,\dots,k+1-k_{\max})} = G^{(k+1,k)} \prod_{j=k+1-k_{\max}}^{k+1} F^{(k+1,j)}, \quad (2.106)$$

and the reduced density matrix

$$\tilde{\rho}^{(k)} = \sum_{k-1,k-2,\dots,k+1-k_{\max}} A^{(k,\dots,k+1-k_{\max})}. \quad (2.107)$$

The computational bottleneck of this algorithm is typically the memory required by the object Λ , which contains $n^{2(k_{\max}+1)}$ complex numbers.

2.7.1 Deviation from the Full Path Sum

By cutting off memory in Eq. (2.93), the i-QUAPI results are based on leaving out the factors

$$\prod_{i=0}^{N-k_{\max}-1} \prod_{j=k_{\max}+1+i}^N F^{(j,i)} \quad (2.108)$$

compared to the full path sum. Due to Eq. (2.79) and (2.81), each of those terms behaves as

$$F^{(j,i)} \sim 1 + \mathcal{O}[\Delta t^2 L((j-i)\Delta t)]. \quad (2.109)$$

The total number of these terms is of order $N^2 = (\frac{t}{\Delta t})^2$. Depending on the decay behavior of $L(t)$, the number of non-negligible terms is of order N to N^2 . Since $(1 + \mathcal{O}[\Delta t^2])^{N^2} = 1 + \mathcal{O}[\Delta t^0]$ and $(1 + \mathcal{O}[\Delta t^2])^N = 1 + \mathcal{O}[\Delta t]$, the memory cutoff may introduce errors of order Δt^n for $n \geq 0$. Therefore i-QUAPI somewhat surprisingly may not only contain discretization errors of second order in Δt due to Eq. (2.64), but also of first order in Δt due to cutting of memory. The term of order Δt^0 is of course the intuitive memory cutoff error that is independent of Δt .

2.8 Improved Iterative QUAPI

In this section, a novel improvement of the method shown in section 2.7 is introduced. Consider the case $k_{\max} = 3$ of Eq. (2.104):

$$A^{(210)} = G^{(21)} G^{(10)} F^{(22)} F^{(21)} F^{(20)} F^{(11)} F^{(10)} F^{(00)} \tilde{\rho}^{(0)}. \quad (2.110)$$

The iteration of Eq. (2.105) can be rewritten as

$$\begin{aligned} A^{(321)} &= \sum_0 G^{(32)} F^{(33)} F^{(32)} F^{(31)} F^{(30)} A^{(210)} \\ &= G^{(32)} F^{(33)} F^{(32)} F^{(31)} \sum_0 F^{(30)} A^{(210)} \\ &= \Omega^{(321)} \sum_0 F^{(30)} A^{(210)} \end{aligned} \quad (2.111)$$

by using

$$\Omega^{(k+1,k,k-1)} = G^{(k+1,k)} F^{(k+1,k+1)} F^{(k+1,k)} F^{(k+1,k-1)}. \quad (2.112)$$

This results in the iterative procedure

$$A^{(k+1,k,k-1)} = \Omega^{(k+1,k,k-1)} \sum_{k-2} F^{(k+1,k-2)} A^{(k,k-1,k-2)} \quad (2.113)$$

with the reduced density matrix

$$\tilde{\rho}^{(k+1)} = \sum_{k,k-1} A^{(k+1,k,k-1)}. \quad (2.114)$$

For arbitrary k_{\max} , we again start with the initial condition given in Eq. (2.104) and then iterate according to

$$A^{(k+1,k,\dots,k+2-k_{\max})} = \Omega^{(k+1,k,\dots,k+2-k_{\max})} \sum_{k+1-k_{\max}} F^{(k+1,k+1-k_{\max})} A^{(k,k-1,\dots,k+1-k_{\max})} \quad (2.115)$$

with

$$\Omega^{(k+1,k,\dots,k+2-k_{\max})} = G^{(k+1,k)} \prod_{j=k+2-k_{\max}}^{k+1} F^{(k+1,j)}. \quad (2.116)$$

The corresponding reduced density matrix is given by

$$\tilde{\rho}^{(k+1)} = \sum_{k,\dots,k+2-k_{\max}} A^{(k+1,k,\dots,k+2-k_{\max})}. \quad (2.117)$$

Note that Ω contains only $n^{2k_{\max}}$ complex numbers, reducing the memory usage compared to Λ of i-QUAPI by a factor of n^2 . This gain in efficiency is due to drawing more of the influence functional terms through sums which their indices do not depend on in Eq. (2.93). Notice that drawing the Ω term in the last line of Eq. (2.111) into the sum \sum_0 leads to the original i-QUAPI.

In our implementation for $n = 2$, a single iteration step shown in Eq. (2.115) for $k_{\max} = 14$ takes ~ 14 seconds on a single processor core while using ~ 6 GB of memory. Given the resources that are available to us, this makes $k_{\max} = 17$ feasible.

2.9 SMatPI

In this section, the small matrix decomposition of the path integral expression (SMatPI) [50], which has been introduced by Makri, is discussed. SMatPI eliminates the large memory requirements of the iterative QUAPI while only introducing an approximation that is small compared to the memory cutoff.

Following Ref. [50], we start with the reduced propagator

$$U^{(N0)} = \sum_{1, \dots, N-1} \prod_{j=1}^N \left(G^{(j, j-1)} \right) \prod_{k'=0}^N \prod_{k''=\max(0, k'-k_{\max})}^{k'} F^{(k'k'')}. \quad (2.118)$$

Consider the case $k_{\max} = 1$ where

$$U^{(k+1,0)} = \sum_k M^{(k+1,k)} U^{(k0)} \quad \text{for } k \geq 1, \quad (2.119)$$

with

$$M^{(k+1,k)} = G^{(k+1,k)} F^{(k+1,k)} F^{(k,k)} \quad \text{for } k \geq 1. \quad (2.120)$$

Note that this is analogous to Eqs. (2.96) and (2.97) with the only difference that we do not fix the initial condition here.

In the case $k_{\max} = 2$, we write $U^{(20)}$ as the *Markovian* term from the previous case, which only contains bath influences that connect adjacent time-steps in the system dynamics, plus a correction from the two-step memory:

$$U^{(20)} = \sum_1 M^{(21)} U^{(10)} + M^{(20)}. \quad (2.121)$$

Using Eqs. (2.118) and (2.120), we find

$$M^{(20)} = (F^{(20)} - 1) \sum_1 M^{(21)} U^{(10)}. \quad (2.122)$$

Due to Eqs. (2.79) and (2.81), the magnitude of this term is of $\mathcal{O}(\Delta t^2 L(2\Delta t))$, which is small for two reasons: Δt should in general be small enough such that $|\eta_{\cdot}| \ll 1$ and in this case we already neglect $\mathcal{O}(\Delta t^2 L(3\Delta t))$ -terms implying that $\mathcal{O}(\Delta t^2 L(2\Delta t))$ -terms will usually also be small. Further note that $F^{(20)} - 1$ will only be nonzero for $s_{i_2^+} \neq s_{i_2^-}$ due to Eq. (2.81).

At the next time-step, we can write

$$U^{(30)} = \sum_2 M^{(32)} U^{(20)} + \sum_1 M^{(31)} U^{(10)} + M^{(30)}. \quad (2.123)$$

In analogy to Eq. (2.122), we have:

$$M^{(31)} = (F^{(31)} - 1) \sum_2 M^{(32)} M^{(21)}, \quad (2.124)$$

and therefore

$$M^{(30)} = \sum_2 \sum_1 (F^{(31)} - 1)(F^{(20)} - 1) M^{(32)} M^{(21)} U^{(10)}. \quad (2.125)$$

This term is of $\mathcal{O}\left((\Delta t^2 L(2\Delta t))^2\right)$ and therefore even smaller than $M^{(20)}$.

The exact decomposition of the reduced propagator can be continued to arbitrary times and arbitrary k_{\max} . It reads

$$U^{(N0)} = \sum_{r=1}^{N-1} \sum_{N-r} M^{(N,N-r)} U^{(N-r,0)} + M^{(N0)}. \quad (2.126)$$

For time-independent \hat{H}_0 we have

$$M^{(N,N-r)} = M^{(r,0)}. \quad (2.127)$$

As the magnitude of $M^{(N0)}$ rapidly decreases when N is increased while k_{\max} is fixed, we may approximate the reduced propagator as

$$U^{(N0)} = \sum_{r=1}^{r_{\max}} M^{(N,N-r)} U^{(N-r,0)} \quad \text{for } N \geq r_{\max} + 1, \quad (2.128)$$

introducing a new convergence parameter r_{\max} . Setting $r_{\max} = k_{\max}$ will typically deviate from the i-QUAPI result using k_{\max} less than the error of the memory truncation of i-QUAPI (see section 2.9.1).

We now give a recipe for the computation of $\tilde{\rho}^{(N)}$ for a time-independent \hat{H}_0 within SMatPI with parameters r_{\max} and k_{\max} . To get the propagation of Eq. (2.128) started, we need $U^{(N0)}$ for $N = 1, \dots, r_{\max}$, which are computed by direct evaluation of Eq. (2.118). Then Eq. (2.126) yields

$$M^{(j,0)} = U^{(j,0)} - \sum_{r=1}^{j-1} M^{(j,r)} U^{(r,0)}. \quad (2.129)$$

According to Eq. (2.127), the $M^{(N,N-r)}$ are now given by $M^{(r,0)}$ for $r = 1, \dots, r_{\max}$. This then allows to approximately compute all $U^{(N,0)}$ by use of Eq. (2.128) and from it the reduced density matrix follows trivially. The most computational demanding part of SMatPI is the calculation of $U^{(r_{\max},0)}$, which requires summation of $n^{2(r_{\max}-1)}$ terms for each of its n^4 entries. For $r_{\max} = k_{\max}$, this effort is comparable to a single i-QUAPI time-step. The computational cost of the SMatPI long-time propagation according to Eq. (2.128) is negligible as it only requires matrix multiplications of $r_{\max} n^2 \times n^2$ matrices for one time-

step. The memory bottleneck of i-QUAPI is eliminated since SMatPI only requires the storage of arrays that contain n^4 complex numbers.

In our implementation for $n = 2$ using the blip decomposition, the computation time on a single processor core for $r_{\max} = 20$ is ~ 20 hours.

2.9.1 Deviation from i-QUAPI

While in previous works examples have been given where choosing $r_{\max} = k_{\max}$ in SMatPI leads to sub-percent level accuracy compared to i-QUAPI taking k_{\max} time-steps of memory into account[10, 50], we will here elaborate more on showing the explicit form of the errors produced by SMatPI in terms of the small factors $(F^{(kk')} - 1)$. For $r_{\max} = k_{\max} = 2$, the dominant term left out in the truncation in Eq. (2.128) is given by Eq. (2.125) and contains the two factors $(F^{(31)} - 1)(F^{(20)} - 1)$. By writing $H^{(\Delta k)} := (F^{kk'} - 1)$ with $\Delta k = k - k'$ and not explicitly writing out the summation and the Markovian dynamics part (which is always incorporated exactly anyway), we get

$$M^{(30)} \propto H^{(2)} \cdot H^{(2)}. \quad (2.130)$$

For $r_{\max} = k_{\max} = 3$, the dominant term $M^{(40)}$ left out in the truncation has the form

$$M^{(40)} \propto 2H^{(3)}H^{(2)} + H^{(3)}H^{(3)} + \mathcal{O}((H)^3). \quad (2.131)$$

The number of terms that are of second order in H contained in $M^{(k_{\max}+1,0)}$ for $r_{\max} = k_{\max} = 3, 4, 5, 6$ are graphically depicted in Fig. 2.2. Note how $M^{(40)}$ is represented, which contains two terms of the form $H^{(3)}H^{(2)}$ and one term of the form $H^{(3)}H^{(3)}$.

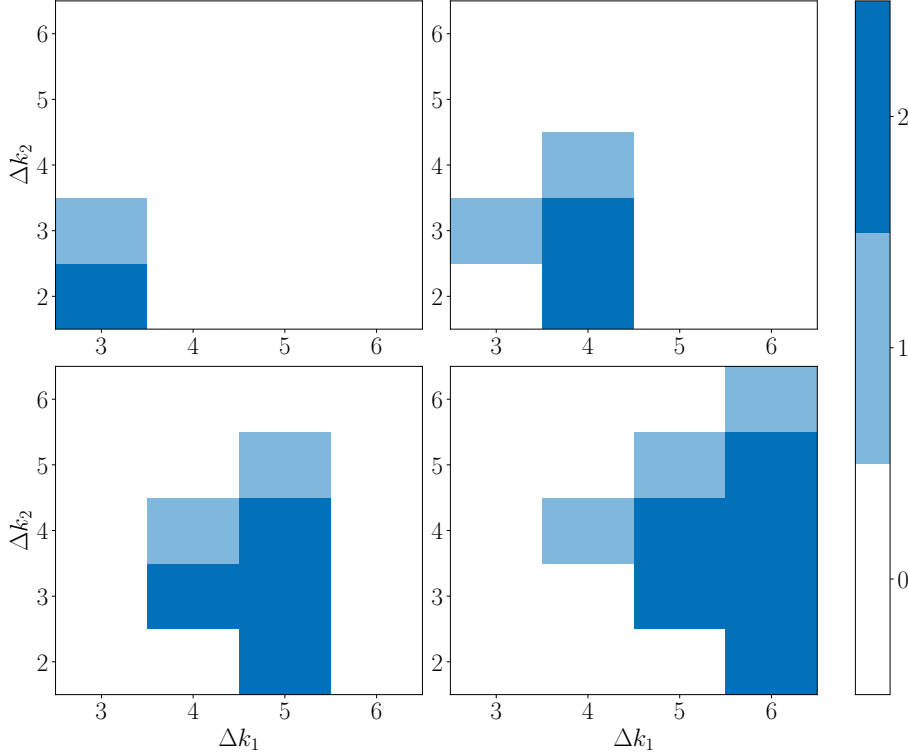


Figure 2.2: Color-coded number of second order terms $H^{(\Delta k_1)} H^{(\Delta k_2)}$ contained in $M^{(k_{\max}+1,0)}$. Top left: $r_{\max} = k_{\max} = 3$. Top right: $r_{\max} = k_{\max} = 4$. Bottom left: $r_{\max} = k_{\max} = 5$. Bottom right: $r_{\max} = k_{\max} = 6$

We have found that the $H^{(\Delta k_1)} H^{(\Delta k_2)}$ terms in $M^{(k_{\max}+1,0)}$ have the property that $\Delta k_1 + \Delta k_2 \geq k_{\max} + 2$, which are of $\mathcal{O}(L(\Delta k_1)L(\Delta k_2))$ (see Fig. 2.2 for a few examples). We have also checked that the terms of third order in H have a similar property. Therefore, the error introduced by SMatPI with $r_{\max} = k_{\max}$ compared to i-QUAPI while increasing k_{\max} will decay similarly to the squared bath autocorrelation function. Thus, the error introduced by the SMatPI-truncation will in general be smaller than the memory-truncation due to the second-order nature of the SMatPI-truncation.

2.10 x-SMatPI

In this section, the extended SMatPI (x-SMatPI) method [51], which has been introduced by Makri, is discussed. x-SMatPI involves incorporating some additional long-range influence functional terms to the SMatPI scheme at essentially no computational cost.

Following Ref. [51], the SMatPI procedure is extended to $k_{\max} > r_{\max}$. Consider $U^{(r_{\max}+1,0)}$ of Eq. (2.128). Compared to the full path sum, it contains the typical SMatPI errors of $\mathcal{O}(H^2)$, but it also does not include $F^{(r_{\max}+1,0)}$. We can simply include it by

$$U^{(r_{\max}+1,0)} = F^{(r_{\max}+1,0)} \sum_{r=1}^{r_{\max}} M^{(r_{\max}+1, r_{\max}+1-r)} U^{(r_{\max}+1-r,0)}. \quad (2.132)$$

By use of Eq. (2.126), it follows that

$$M^{(r_{\max}+1,0)} = (F^{(r_{\max}+1,0)} - 1) \sum_{r=1}^{r_{\max}} M^{(r_{\max}+1, r_{\max}+1-r)} U^{(r_{\max}+1-r,0)}. \quad (2.133)$$

We may even proceed with this procedure to arbitrary k_{\max} at negligible computational cost as this operation only acts on the small matrices with n^4 elements. Note that this method will include all first order contributions from influence terms that span up to k_{\max} time-steps.

Including the correct connections to intermediate and end points and also computing the quantities that are needed for propagation, we extend the propagation of SMatPI and calculate

$$U^{(r_{\max}+j,0)} = F^{(r_{\max}+j,0)} \sum_{r=1}^{r_{\max}+j-1} M^{(r_{\max}+j, r_{\max}+j-r)} U^{(r_{\max}+j-r,0)}, \quad (2.134)$$

$$M^{(r_{\max}+j,0)} = \left(F^{(r_{\max}+j,0)} - 1 \right) \sum_{r=1}^{r_{\max}+j-1} M^{(r_{\max}+j, r_{\max}+j-r)} U^{(r_{\max}+j-r,0)} \quad (2.135)$$

for $j = 1, \dots, k_{\max} - r_{\max}$. If we decide to cut bath memory after k_{\max} time-steps, for example to test if cutting extremely long range correlations makes a difference, we can do so by computing

$$U^{(j,0)} = \sum_{r=1}^{k_{\max}} M^{(j, j-r)} U^{(j-r,0)} \quad (2.136)$$

for $j \geq k_{\max} + 1$.

2.10.1 Deviation from the Full Path Sum

Suppose we want to compute $U^{(N,0)}$ at some arbitrary time $N\Delta t$. We may set $k_{\max} = N$ as this comes at no significant computational effort within x-SMatPI and then start from a low r_{\max} and increase it until convergence is reached. The second order terms in H of the error that x-SMatPI introduces are graphically depicted in Fig. 2.3 for the case $N = 6$. We again find that the $H^{(\Delta k_1)} H^{(\Delta k_2)}$ terms have the property that $\Delta k_1 + \Delta k_2 \geq r_{\max} + 2$. Thus, the error introduced by x-SMatPI while increasing r_{\max} will again decay similarly to the bath autocorrelation function. Of course the number of error terms in an x-SMatPI calculation with $r_{\max} < k_{\max}$ is far larger than for the corresponding SMatPI calculation with $r_{\max} = k_{\max}$ as the SMatPI decomposition is truncated earlier. In fact, it has been numerically shown that x-SMatPI performs similarly to SMatPI in some cases as the additional influence functional terms taken into account are offset by the additional approximation [52].

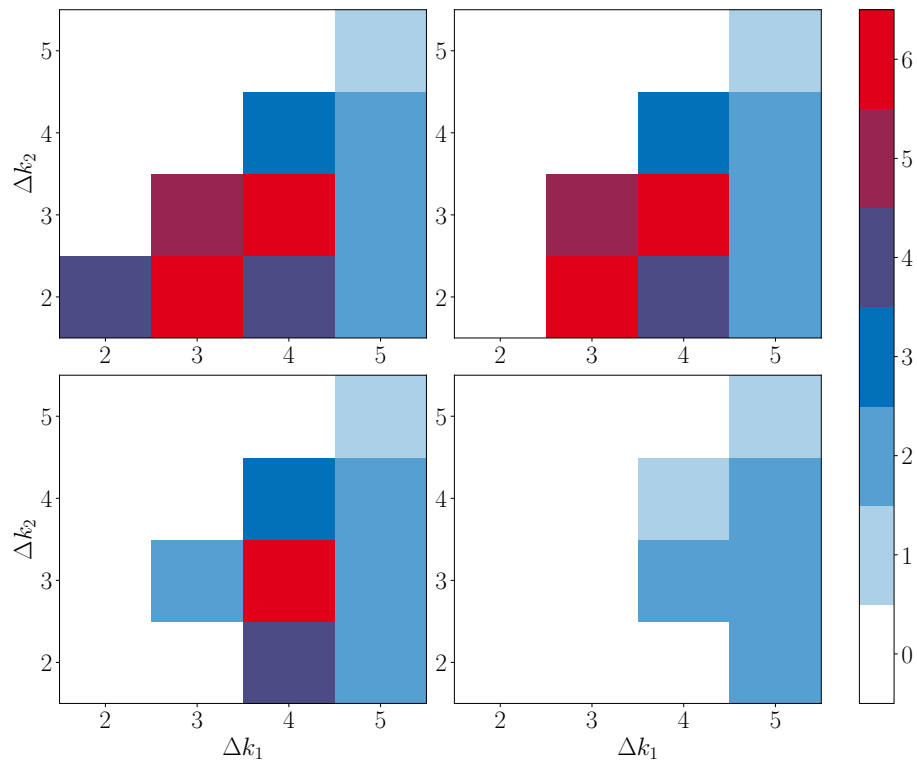


Figure 2.3: Color-coded number of second order terms $H^{(\Delta k_1)} H^{(\Delta k_2)}$ contained in the difference between the full path sum $U^{(60)}$ and its approximation using x-SMatPI with $k_{\max} = 6$ and different values for r_{\max} . Top left: $r_{\max} = 2$. Top right: $r_{\max} = 3$. Bottom left: $r_{\max} = 4$. Bottom right: $r_{\max} = 5$.

3 Time-Evolving Matrix Product Operator (TEMPO)

All of the improvements of the original QUAPI method presented in chapter 2 directly inherit the exponential scaling of the path sum (Eq. (2.84)) with respect to the number of time-steps without cutting off memory.

A similar fundamental problem is encountered in quantum many-body physics, where the Hilbert space scales exponentially with the number of particles. The density matrix renormalization group (DMRG) [56, 57] is a variational technique concerned with finding the ground state of such many-body problems by compressing their wavefunction into a *matrix product state*, which makes use of the fact that such states are typically far from being fully entangled [58].

A similar strategy is employed by the time-evolving matrix product operator (TEMPO) technique [11], which efficiently compresses the discretized influence function of QUAPI into a matrix product state. However, the scopes of DMRG and TEMPO are very different. While DMRG compresses the state of many particles into a matrix product state at a fixed time, TEMPO compresses the history of a single particle immersed in a heat bath into a matrix product state. Stated differently, the matrix product states used in DMRG exist in space while the matrix product states used in TEMPO exist in time.

In section 3.1, the formal prerequisites of TEMPO are presented. This is followed by a novel simplified derivation of TEMPO in section 3.2. In section 3.3, we validate our numerical TEMPO results on a single mode model, which is trivial to solve using other methods. However, for the TEMPO approach it presents a significant challenge as it renders the system dynamics strongly non-Markovian. Furthermore, the scaling of TEMPO with respect to the Trotter time-step size is analyzed on this model.

The effects of dissipative environments on the electronic dynamics in biomolecules can be modeled by a more general version of the Caldeira-Leggett model involving multiple baths [30, 31]. In section 3.4, we introduce a novel generalization of the TEMPO method to this case. Subsequently, this method is validated by comparing to previous results and then used to investigate the suppression of the localization transition in the Ohmic spin-boson model by a second bath.

3.1 Introduction to Tensor Networks

In this section, the basics of tensor networks required for understanding the TEMPO algorithm [11] are presented by following Refs. [45, 59]. Consider a state in a two-body Hamiltonian $|\psi\rangle \in \mathcal{H}_1 \otimes \mathcal{H}_2$ with finite-dimensional Hilbert spaces $\dim(\mathcal{H}_1) = \dim(\mathcal{H}_2) = d$. Given orthonormal bases $\{|n_j\rangle | n_j \in \{1, 2, \dots, d\}\}$ where $j \in \{1, 2\}$, we can write

$$|\psi\rangle = \sum_{n_1, n_2} |n_1, n_2\rangle \langle n_1, n_2 | \psi\rangle =: \sum_{n_1, n_2} \psi^{n_1 n_2} |n_1, n_2\rangle. \quad (3.1)$$

The standard graphical representation for the matrix $\psi^{n_1 n_2} \in \mathbb{C}^{d \times d}$ is a rectangle with a *leg* for each index and is depicted in Fig. 3.1. If the two-body state $|\psi\rangle$ is separable (i.e.

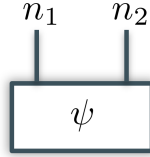


Figure 3.1: Tensor diagram of the coefficient matrix $\psi^{n_1 n_2}$ of Eq. (3.1).

not entangled), then $\psi^{n_1 n_2}$ factorizes as

$$\psi^{n_1 n_2} = \psi_1^{n_1} \psi_2^{n_2} \quad (3.2)$$

into the two rank-1 tensors $\psi_1^{n_1}$ and $\psi_2^{n_2}$, which are depicted in Fig. 3.2. Note that we use

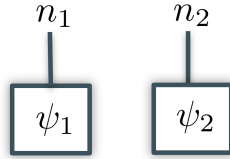


Figure 3.2: Tensor diagram of the rank-1 tensors $\psi_{1,2}^{n_{1,2}}$ of Eq. (3.2) with indices indicated on top of legs.

the term "rank- k tensor" here to reference a k -dimensional array of complex numbers and not an object with a specific behavior under some transformation. The *matrix product state* (MPS) representation is given by

$$\psi^{n_1 n_2} = \sum_i (\psi_1)_i^{n_1} (\psi_2)_i^{n_2}. \quad (3.3)$$

Note how the matrix product state is effectively an expansion of the state in Eq. (3.1) into multiple separable states. The rank-2 tensors $(\psi_1)_i^{n_1}$ and $(\psi_2)_i^{n_2}$ may be retrieved from

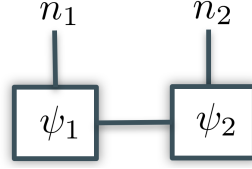


Figure 3.3: Tensor diagram of the matrix product state $\sum_i (\psi_1)_i^{n_1} (\psi_2)_i^{n_2}$ of Eq. (3.3).

$\psi^{n_1 n_2}$ by applying a singular value decomposition (SVD):

$$\psi^{n_1 n_2} = \sum_{i=1}^{\text{rank}(\psi^{n_1 n_2})} L_i^{n_1} \sigma_i R_i^{n_2} \quad (3.4)$$

where we identify $(\psi_1)_i^{n_1} = L_i^{n_1} \sigma_i$ and $(\psi_2)_i^{n_2} = R_i^{n_2}$ using the convention to multiply the singular values σ_i to the left. Graphically, we represent the sum over the common index i in Eq. (3.3) by connecting up the corresponding legs into a bond as shown in Fig. 3.3. The number of terms in the sum that is represented by such a bond is referred to as the *bond dimension*. Consider the example of a system consisting of two spin- $\frac{1}{2}$ particles, i.e. $|n_{1,2}\rangle \in \{|\uparrow\rangle, |\downarrow\rangle\}$, which are in the state

$$\psi = \frac{1}{\sqrt{2}}(|\uparrow\uparrow\rangle + |\downarrow\uparrow\rangle) =: \frac{1}{\sqrt{2}} \begin{pmatrix} 1 & 0 \\ 1 & 0 \end{pmatrix}. \quad (3.5)$$

Application of a SVD yields

$$\mathbf{L} = \frac{1}{\sqrt{2}} \begin{pmatrix} 1 & 1 \\ 1 & -1 \end{pmatrix} \quad \boldsymbol{\sigma} = \begin{pmatrix} 1 \\ 0 \end{pmatrix} \quad \mathbf{R} = \begin{pmatrix} 1 & 0 \\ 0 & -1 \end{pmatrix}. \quad (3.6)$$

As the rank of the matrix in Eq. (3.5) is 1, there is only one non-zero singular value and thus the MPS consists of only one term $\psi = \psi_1 \psi_2$ with $\psi_1 = \frac{1}{\sqrt{2}}(|\uparrow\rangle + |\downarrow\rangle)$ and $\psi_2 = |\uparrow\rangle$. Thus, constructing the MPS has automatically revealed the fact that the state in Eq. (3.5) is separable. More generally, the degree of entanglement of the system is related to the absolute value of the singular values.

Next consider a many-body state $|\psi\rangle \in \mathcal{H}_1 \otimes \mathcal{H}_2 \otimes \dots \otimes \mathcal{H}_N$. In analogy to the two-body case, we write the state in some orthonormal basis as

$$|\psi\rangle = \sum_{n_1, n_2, n_3, \dots, n_N} \psi^{n_1 n_2 n_3 \dots n_N} |n_1, n_2, n_3, \dots, n_N\rangle \quad (3.7)$$

and graphically represent the arising rank- N tensor $\psi^{n_1 n_2 n_3 \dots n_N}$ in Fig. 3.4. The MPS representation in this case has the form

$$\psi^{n_1 n_2 n_3 \dots n_N} = \sum_i (\psi_1)_{i_1}^{n_1} (\psi_2)_{i_1 i_2}^{n_2} (\psi_3)_{i_2 i_3}^{n_3} \dots (\psi_N)_{i_{N-1}}^{n_N}, \quad (3.8)$$

which is graphically represented in Fig. 3.5. This case makes the potential for exponential

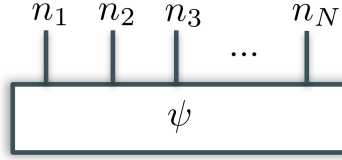


Figure 3.4: Tensor diagram of the coefficient rank- N tensor $\psi^{n_1 n_2 n_3 \dots n_N}$ of Eq. (3.7).

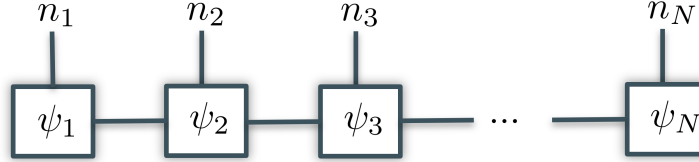


Figure 3.5: Tensor diagram of the matrix product state $\sum_i (\psi_1)_{i_1}^{n_1} (\psi_2)_{i_1 i_2}^{n_2} (\psi_3)_{i_2 i_3}^{n_3} \dots (\psi_N)_{i_{N-1}}^{n_N}$ of Eq. (3.8).

savings in the amount of memory required to store a quantum many-body state apparent: The MPS represents a rank- N tensor while only consisting of rank-3 tensors. To accurately represent a maximally entangled state however, the bond dimension of the respective tensors would be so large that no memory would be saved. In cases where the system is far from being fully entangled, which is oftentimes fulfilled in many-body systems [58], the savings in memory will indeed be exponential. While the computation of a scalar product $\langle \psi | \phi \rangle$ has complexity $\mathcal{O}(d^N)$ for uncompressed states, the complexity reduces to $\mathcal{O}(b^3 d N)$ if ψ and ϕ are matrix product states with bond dimension b for every internal bond. For $N = 3$, the corresponding tensor diagram is given in Fig. 3.6. The

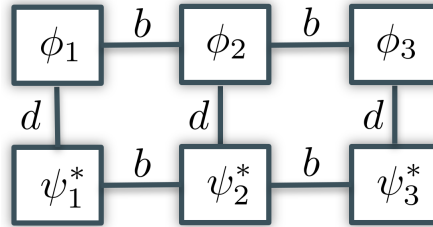


Figure 3.6: Tensor diagram of the scalar product $\langle \psi | \phi \rangle$ with bond dimensions indicated next to bonds.

procedure to contract this tensor diagram is sketched in Fig. 3.7. We start by taking the tensors ϕ_1 and ψ_1^* and execute the summation of d terms for each of the b^2 elements of the resulting rank-2 tensor, which is an $\mathcal{O}(b^2 d)$ operation. Next, we contract this tensor with ϕ_2 , which requires summation of b terms for each of the $b^2 d$ terms of the resulting rank-3 tensor, which is an $\mathcal{O}(b^3 d)$ operation. This tensor is then contracted with ψ_2^* , which requires summation of bd terms for each of the b^2 terms of the resulting rank-2 tensor, which is again an $\mathcal{O}(b^3 d)$ operation. The final result for the scalar product is then obtained by contracting with ϕ_3 and ψ_3^* , which is an $\mathcal{O}(b^2 d)$ operation. Note how this procedure is straightforwardly generalized to arbitrary N by repetition of the second and third step. The computational complexity of the scalar product is thus reduced from exponential to

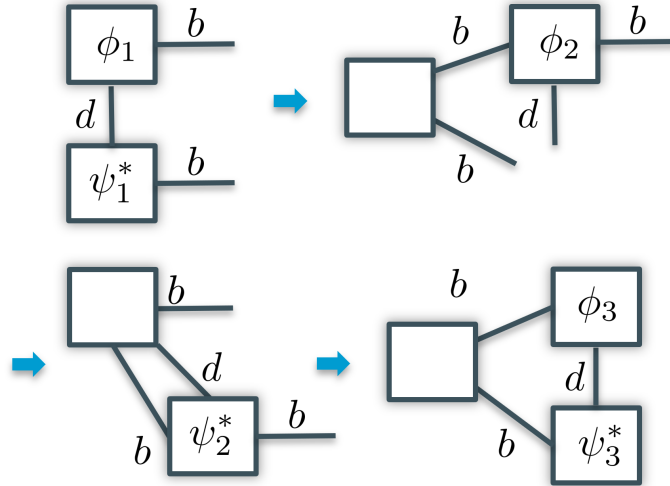


Figure 3.7: Contraction of the scalar product tensor diagram shown in Fig. 3.6.

linear scaling in N as all the operations are only acting locally. Keep in mind however that in the case of full entanglement these savings will be counteracted by the bond dimension b scaling exponentially in N . In analogy to the matrix product state as in Fig. 3.5,

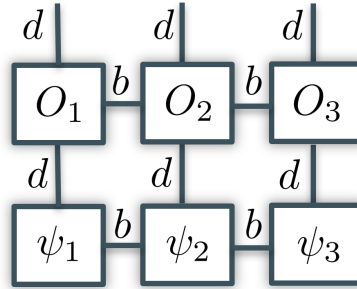


Figure 3.8: Tensor diagram of a matrix product operator \hat{O} acting on a matrix product state $|\psi\rangle$.

an operator \hat{O} can be represented as a *matrix product operator* (MPO)

$$O^{n_1 m_1 n_2 m_2 \dots n_N m_N} = \sum_i (O_1)_{i_1}^{n_1 m_1} (O_2)_{i_1 i_2}^{n_2 m_2} (O_3)_{i_2 i_3}^{n_3 m_3} \dots (O_N)_{i_{N-1}}^{n_N m_N}. \quad (3.9)$$

The procedure to compute an MPO acting on an MPS as sketched for $N = 3$ in Fig. 3.8 is similar to the scalar product and of crucial importance for the TEMPO algorithm introduced in Section 3.2. As sketched in Fig. 3.9, we start by contracting O_1 and ψ_1 together, which is an $\mathcal{O}(b^2 d^2)$ operation. Then, we contract O_2 and ψ_2 together, which is an $\mathcal{O}(b^4 d^2)$ operation. Finally, we contract O_3 and ψ_3 together, which is again of $\mathcal{O}(b^2 d^2)$. Generalized to arbitrary N , this procedure is thus of $\mathcal{O}(N b^4 d^2)$. Note how the bond dimension of the resulting MPS is b^2 as opposed to b in the initial state, which means that repeated application of an MPO to an MPS leads to an exponential growth of the bond dimension. Assuming limited entanglement, this can be significantly slowed by performing an SVD on all of the bonds and then truncating singular values. Thus we continue our procedure

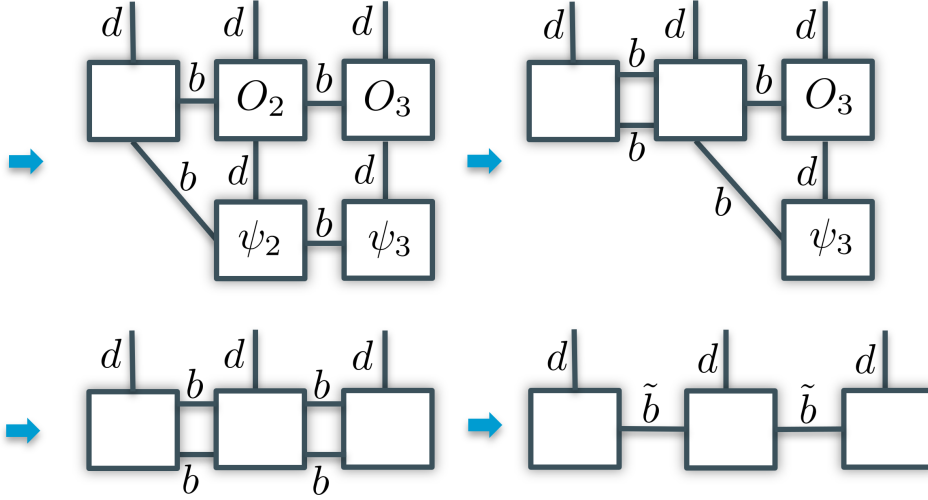


Figure 3.9: Contraction of the tensor diagram of a matrix product operator acting on a matrix product state as shown in Fig. 3.8.

in the third step of Fig. 3.9 by performing an SVD of the two tensors on the left, which represent a $d \times b^2d$ matrix. We then truncate all singular values λ , which are smaller than $\lambda_c \cdot \lambda_{\max}$, where λ_{\max} is the largest singular value and λ_c is a convergence parameter related to the fidelity of the approximation. This is then repeated for all remaining bonds as well, which forms a full compression *sweep*. In order to improve compression, several sweeps are performed resulting in bond dimensions \tilde{b} , which are generally smaller than b . We remark that in the literature a procedure where one truncates all singular values that have a sum of squares smaller than a threshold times the sum of all squared singular values is commonplace [60].

3.2 TEMPO: Computing QUAPI using a Tensor Network

In the reduced propagator of the QUAPI scheme Eq. (2.84), the structure connecting two adjacent time-steps shows up in both the bare system propagator and the influence functional. Using a simplified notation $\alpha_k := i_k^\pm$ and leaving out the superscripts as they can be read off from the subscripts, we define [45]

$$I_{\alpha_{k_1} \alpha_{k_2}} := \begin{cases} G_{\alpha_{k_1} \alpha_{k_2}} F_{\alpha_{k_1} \alpha_{k_2}} & \text{if } k_1 - k_2 = 1, \\ F_{\alpha_{k_1} \alpha_{k_2}} & \text{else,} \end{cases} \quad (3.10)$$

to reach a more compact notation for the reduced propagator

$$U_{\alpha_N \alpha_0} = \sum_{\alpha_1, \dots, \alpha_{N-1}} \prod_{k=0}^{N-1} \prod_{k'=0}^k I_{\alpha_k \alpha_{k'}}. \quad (3.11)$$

Using this expression as a starting point, a more intuitive derivation than what has originally been given in Ref. [45] is shown here. We first consider the case $N = 1$ of Eq. (3.11)

in Fig. 3.10. We explicitly write the three tensors that the reduced propagator consists

$$\begin{aligned}
 U_{\alpha_1\alpha_0} &= I_{\alpha_1\alpha_1} I_{\alpha_1\alpha_0} I_{\alpha_0\alpha_0} = I_{\alpha_1\alpha_1} \sum_{\beta_0} I_{\alpha_1\beta_0} \delta_{\alpha_0\beta_0} I_{\alpha_0\alpha_0} \\
 &= \sum_{\beta_1} \delta_{\alpha_1\beta_1} I_{\alpha_1\alpha_1} \sum_{\beta_0} I_{\beta_1\beta_0} \delta_{\alpha_0\beta_0} I_{\alpha_0\alpha_0}
 \end{aligned}$$

Figure 3.10: Manipulation of Eq. (3.11) for $N = 1$ with corresponding tensor diagrams with indices indicated next to legs.

of in that case and arrange them in a tensor diagram in a triangular structure motivated by the structure of Eq. (3.11). Note that the tensors are not connected in the first step as there is no summation. In the next step, we introduce a Kronecker delta $\delta_{\alpha_0\beta_0}$ and a sum over all β_0 , which cancel each other out. In the tensor diagram, we now reinterpret the bottom right tensor marked in blue as $\delta_{\alpha_0\beta_0} I_{\alpha_0\alpha_0}$, which is then a (diagonal) rank-2 tensor. Additionally, we are allowed to replace α_0 by β_0 in $I_{\alpha_1\alpha_0}$ as the Kronecker delta always ensures $\alpha_0 = \beta_0$ anyways. The sum over β_0 is then automatically incorporated in the tensor diagram in the bond between the top and bottom right tensor. We then proceed by introducing the Kronecker delta $\delta_{\alpha_1\beta_1}$ and a corresponding sum over β_1 and replace α_1 by β_1 in $I_{\alpha_1\beta_0}$. Then, we interpret the bottom left tensor marked in red as $\delta_{\alpha_1\beta_1} I_{\alpha_1\alpha_1}$. Notice that the introduction of Kronecker deltas has allowed us to form a bond out of all the legs of tensors that are pointed to another tensor in the tensor diagram. In the case $N = 2$, the reduced propagator reads $U_{\alpha_2\alpha_0} = \sum_{\alpha_1} I_{\alpha_2\alpha_2} I_{\alpha_2\alpha_1} I_{\alpha_2\alpha_0} I_{\alpha_1\alpha_1} I_{\alpha_1\alpha_0} I_{\alpha_0\alpha_0}$, which is drawn as a tensor diagram at the top of Fig. 3.11 with the sum over the index α_1 being written explicitly. Following our observation in the case $N = 1$, we connect up all the legs pointed to another tensor (marked in blue). Then we realize that there are two open legs with index α_1 , which by definition form a bond together with the sum over α_1 (marked in red). For $N = 3$, this procedure results in the tensor diagram given in Fig. 3.12. The generalization of this procedure to arbitrary N is now straightforward. The formal definition of the tensors labeled (k_1, k_2) in the figures above is given in Fig. 3.13 where tensors with fewer legs lack the corresponding Kronecker deltas. Finally, the reduced propagator Eq. (3.11) is computed iteratively by contracting the arising tensor network. We begin with the three

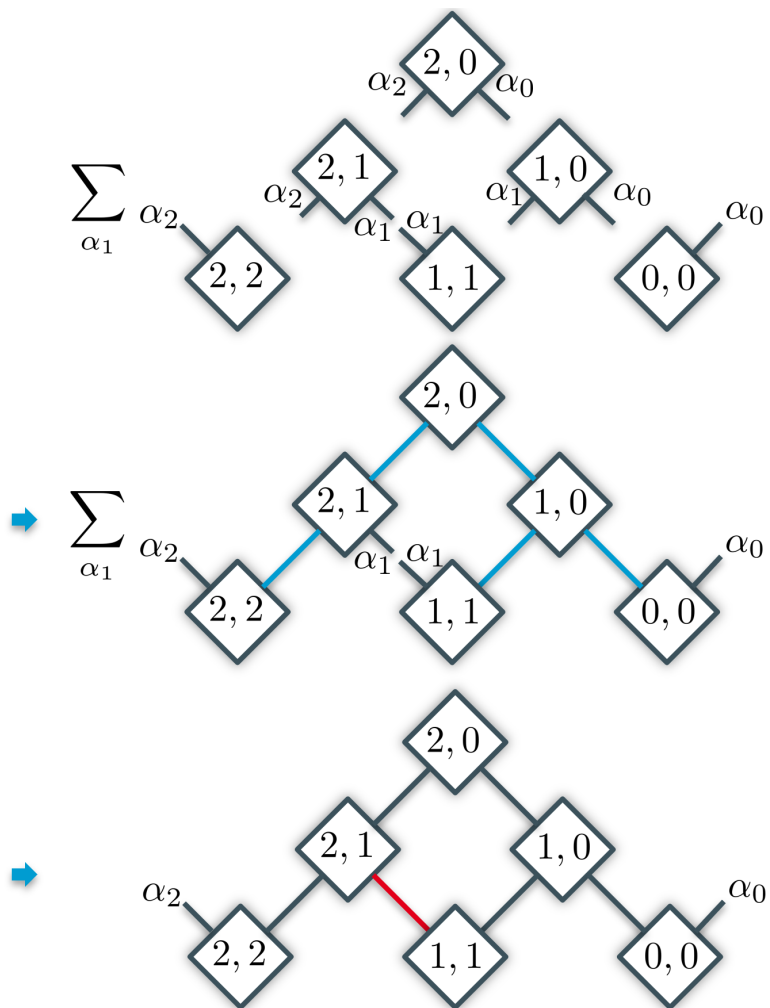


Figure 3.11: Tensor diagrams for manipulation of Eq. (3.11) for $N = 2$ with indices indicated next to legs.

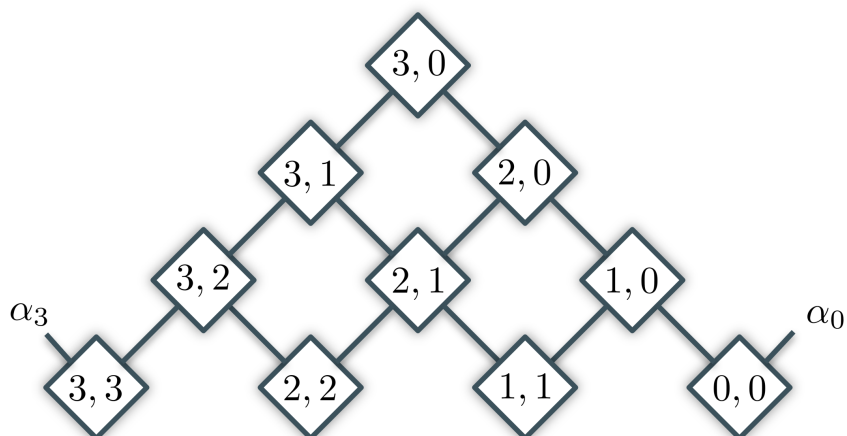


Figure 3.12: Tensor diagram of Eq. (3.11) for $N = 3$ with indices indicated next to legs.

tensors on the lower right and contract the bond between the tensors $(1,0)$ and $(0,0)$ as marked in blue in Fig. 3.14. Then, we store the resulting tensors for the next time-step

$$\begin{array}{c}
 \alpha_{k_2} \\
 \diagdown \quad \diagup \\
 \text{ } \quad \text{ } \\
 \diagup \quad \diagdown \\
 \alpha_{k_1} \quad \beta_{k_2}
 \end{array}
 \begin{array}{c}
 \beta_{k_1} \\
 \diagup \quad \diagdown \\
 \text{ } \quad \text{ } \\
 \diagdown \quad \diagup \\
 \alpha_{k_1} \quad \beta_{k_2}
 \end{array}
 = \delta_{\alpha_{k_1} \beta_{k_1}} \delta_{\alpha_{k_2} \beta_{k_2}} I_{\alpha_{k_1} \alpha_{k_2}}$$

Figure 3.13: Definition of tensors shown in Fig. 3.10, Fig. 3.11, and Fig. 3.12.

and obtain the reduced propagator for $N = 1$ by summing over the redundant leg β_0 and the remaining bond. For the next time-step, we begin with the saved tensors from

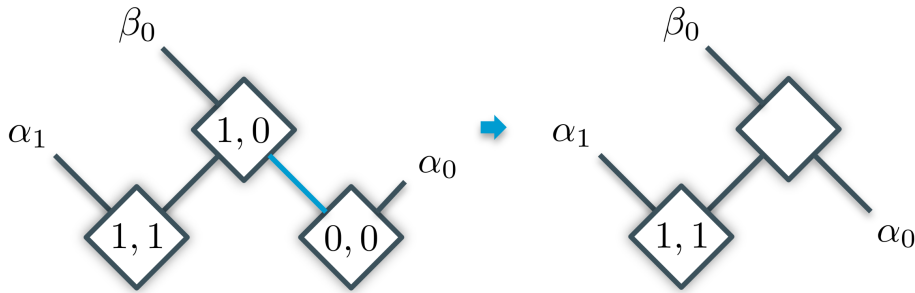


Figure 3.14: Tensor diagram for the first Trotter time-step of TEMPO.

the previous step and contract them with the next diagonal row of tensors, as depicted in Fig. 3.15. Note that this operation closely resembles an MPO acting on an MPS, which we subsequently handle as discussed in Section 3.1. We once again store the resulting tensors for the next time-step and obtain the reduced propagator for $N = 2$ by summing out the redundant legs β_0 and β_1 , and then contracting the remaining bonds. Thus, the essence

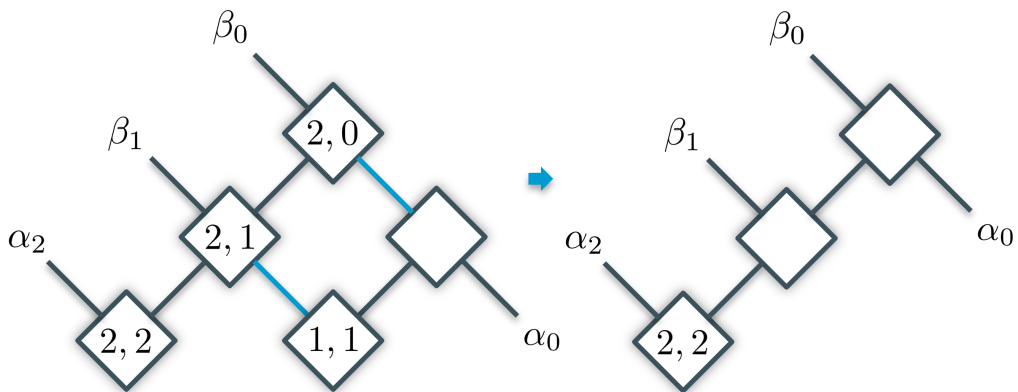


Figure 3.15: Tensor diagram for the second Trotter time-step of TEMPO.

of the TEMPO method is to reformulate the path summation in Eq. (2.84), which is the central object of the QUAPI method. This reformulation involves expressing it as the con-

traction of a tensor network. The MPS-MPO contractions are accompanied by a singular value cutoff denoted as λ_c . This is treated as a convergence parameter and thus TEMPO retains the numerical exactness of QUAPI. The primary advantage of TEMPO lies in the significant extension of the number of time-steps that can be computed without imposing a hard memory cutoff. This extension has proven crucial for the research presented in chapter 4. Specifically, while the full path sum can be computed up to approximately $N = 20$ for a two-level system (see also Section 2.9), the corresponding tensor network can typically be contracted with negligible error for several hundred or even more time-steps, depending on the bath spectral density.

3.3 Benchmark of TEMPO on a Single Mode Model

Consider the special case of the Caldeira-Leggett model of Eq. (2.36), where the central system is a symmetric two-level system

$$\hat{H}_S = \frac{\Omega}{2} \hat{\sigma}_x \quad (3.12)$$

with the Pauli matrix σ_x and the parameter Ω , which is referred to as the *tunneling splitting*. The two-level system is then coupled to a single harmonic mode at frequency ν via the coupling operator $\hat{s} = \hat{\sigma}_z$. Expressing the full Hamiltonian in terms of ladder operators, we have:

$$\hat{H} = \hat{H}_S + \hat{H}_{\text{int}} + \hat{H}_{\text{osc}} = \frac{\Omega}{2} \hat{\sigma}_x - \frac{g}{2} \hat{\sigma}_z (\hat{a} + \hat{a}^\dagger) + \nu \hat{a}^\dagger \hat{a}. \quad (3.13)$$

Here, we choose $\Omega = g = \nu$. Terms proportional to the identity operator are omitted from the Hamiltonian, as they do not impact the dynamics (including the counter-term, since $\hat{\sigma}_z^2 = \hat{\mathbb{1}}$). The solution can be straightforwardly obtained by retaining only the lowest N eigenstates of the harmonic mode, i.e.

$$\hat{H}_{\text{osc}} = \sum_{n=1}^{\infty} \nu |n\rangle \langle n| \approx \sum_{n=1}^N \nu |n\rangle \langle n|, \quad (3.14)$$

and then numerically integrating the Schrödinger equation where N is treated as a convergence parameter. For the two-level system initialized in the $|\uparrow\rangle$ state and the oscillator initialized in the ground state, the *polarization* dynamics $P(t) := \langle \hat{\sigma}_z \rangle(t)$ is shown in Fig. 3.16. As high-energy oscillator states are exponentially suppressed, rapid convergence with respect to N is observed. We use this result to benchmark the TEMPO algorithm. To recover the model in Eq. (3.13), we choose the spectral density

$$J(\omega) = \pi g^2 \delta(\omega - \nu). \quad (3.15)$$

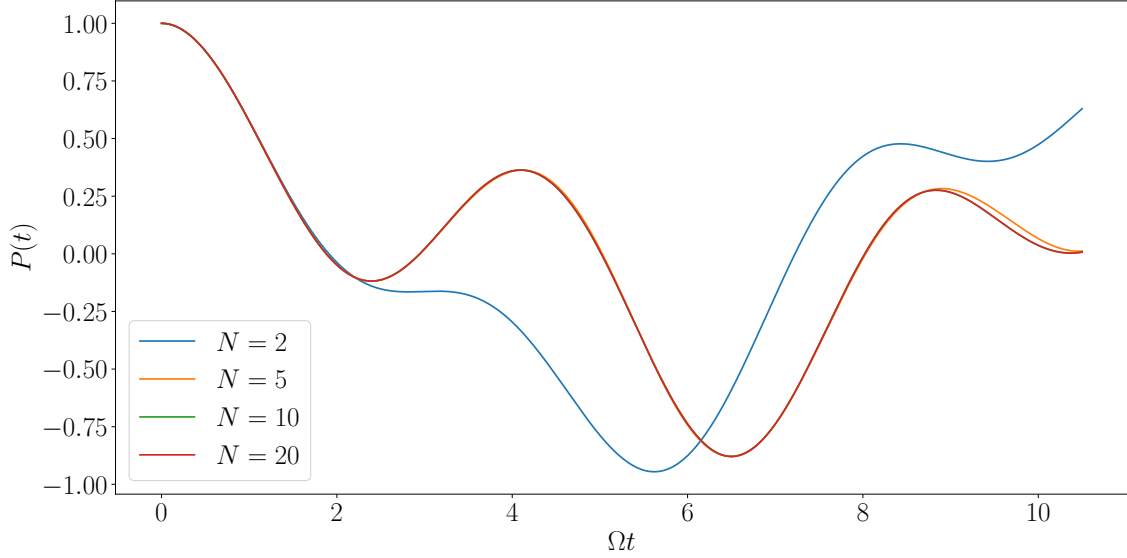


Figure 3.16: Polarization dynamics of the single mode model obtained by numerical integration of the Schrödinger equation for different numbers of oscillator eigenstates N retained.

The initial preparation of the oscillator in the ground state corresponds to zero temperature, i.e., $\coth\left(\frac{\omega\beta}{2}\right) = 1$. Consequently, the bath autocorrelation function becomes

$$L(t) = g^2 e^{-i\omega t}. \quad (3.16)$$

While this toy model is trivial to solve by direct integration of the Schrödinger equation as shown before, it poses a formidable challenge for the TEMPO approach. This is because TEMPO relies on the assumption that the influence functional compresses well. The rate of compression is related to the amount of long-time entanglement within the Feynman-Vernon influence functional, which depends on how quickly $L(t)$ falls off due to Eq. (2.79). As $L(t)$ does not fall off at all in this case, methods imposing a hard memory cutoff such as i-QUAPI and SMatPI cannot be used and one might think that the execution of the full path sum in Eq. (2.84) would be the best option. However, it turns out that TEMPO still performs much better than the full path summation. The corresponding TEMPO result is shown and compared to the direct integration of the Schrödinger equation in Fig. 3.17. In the TEMPO simulations, we have found that smaller Trotter time-steps Δt require a smaller singular value cutoff λ_c to reach the same level of accuracy. Specifically:

- For $\Omega\Delta t = 0.4$, we choose $\lambda_c \in \{10^{-3.5}, 10^{-4}, 10^{-4.5}\}$.
- For $\Omega\Delta t = 0.3$, we choose $\lambda_c \in \{10^{-4}, 10^{-4.5}, 10^{-5}\}$.
- For $\Omega\Delta t = 0.2$, we choose $\lambda_c \in \{10^{-4.5}, 10^{-5}, 10^{-5.5}\}$.

For the smallest Trotter time-step of $\Omega\Delta t = 0.2$, 50 TEMPO iteration steps have been per-

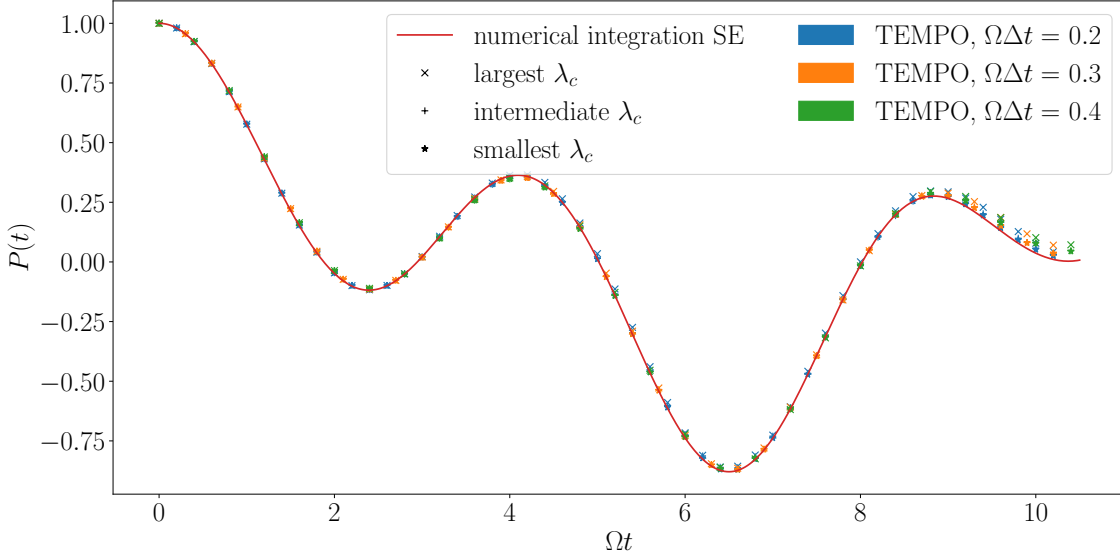


Figure 3.17: Polarization dynamics of the single mode model obtained by numerical integration of the Schrödinger equation at $N = 20$ (red solid line) and TEMPO results (markers) with color-coded Trotter time-step Δt and singular value cutoff λ_c markerstyle-coded (from least to most accurate: cross, plus, star).

formed within a few minutes on a laptop with converged λ_c . In contrast, the summation of the full path sum would take about 6 orders of magnitude longer than the age of the universe to compute using the same hardware. In Fig. 3.18, the growth of internal bond dimension arising in the contraction of the TEMPO tensor network is visualized. After the first time-step, there is only one internal bond as shown on the right-hand side of Fig. 3.14. In the second time-step there are two internal bonds as shown on the right-hand side of Fig. 3.15, with the number of internal bonds increasing by one for every subsequent time-step. The bond dimension grows almost exponentially (see Fig. 3.18 (b)) as a result of the strong long-time entanglement mentioned earlier.

Notably, the maximum bond dimension remains essentially constant in time for different choices of Δt , as shown in Fig. 3.18 (b). Consequently, TEMPO scales only quadratically in the number of time-steps taken while keeping the simulation time and the accuracy with respect to λ_c constant. This is another significant advantage over the summation of the full path sum, which scales exponentially in this respect.

3.4 Generalization of TEMPO to Non-Commuting Baths

In this section, a novel generalization of the TEMPO method that allows to compute the dynamics of systems that are coupled to two baths via coupling operators that do not commute with each other. This is done by rephrasing the path sum obtained by Palm [29], which is based on the QUAPI method, such that it can be computed in terms of a tensor network contraction. Thereby, a substantial increase in computational efficiency is achieved.

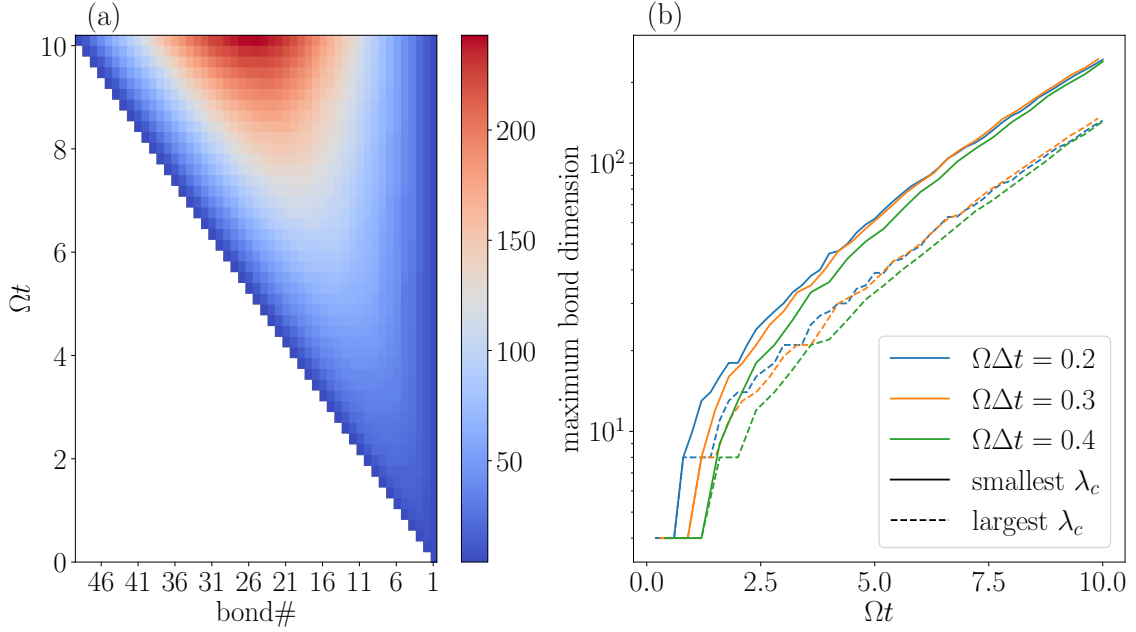


Figure 3.18: Growth of bond dimensions within TEMPO as a function of time. (a) Color-coded internal bond dimensions for every site for $\lambda_c = 10^{-5.5}$ and $\Omega\Delta t = 0.2$. Each row corresponds to a time-step. (b) Maximum internal bond dimension for different Trotter time-steps and λ_c corresponding to a comparable level of accuracy within the given Trotter time-step.

Consider the extension of the Caldeira-Leggett model where the central system couples to two harmonic oscillator baths with the Hamiltonian

$$\hat{H} = \hat{H}_S + \hat{H}_{\text{env},1} + \hat{H}_{\text{env},2} = \hat{H}_S + \sum_j \left[\frac{\hat{p}_{1,j}^2}{2m_{1,j}} + \frac{1}{2}m_{1,j}\omega_{1,j}^2 \left(\hat{x}_{1,j} - \frac{c_{1,j}\hat{s}_1}{m_{1,j}\omega_{1,j}^2} \right)^2 \right] + \sum_j \left[\frac{\hat{p}_{2,j}^2}{2m_{2,j}} + \frac{1}{2}m_{2,j}\omega_{2,j}^2 \left(\hat{x}_{2,j} - \frac{c_{2,j}\hat{s}_2}{m_{2,j}\omega_{2,j}^2} \right)^2 \right]. \quad (3.17)$$

Here, we assume that the first bath is a *pure dephasing* bath, characterized by the commutation relation $[\hat{s}_1, \hat{H}_S] = 0$. For the other bath, we allow a general coupling operator, which typically will be non-commuting, i.e., $[\hat{s}_1, \hat{s}_2] \neq 0$. In Ref. [29], QUAPI has been generalized to this model. The approach involves using a memory cutoff and then iteratively computing the path sum, similar to the method presented in section 2.7. Due to the additional set of oscillators, this approach is significantly more computationally expensive, effectively halving the number of memory steps k_{max} that can be taken into account. As opposed to the treatment in section 3.2, it is advantageous for this purpose to consider the system propagator and the influence functional separately, as previously done in Ref. [61]. This separation allows us to compute the influence functional independently of the parameters of the central system. Consequently, the influence functional can be reused for different parameter choices of the central system.

In the previously considered single-bath case (using the Hamiltonian in Eq. (2.36)), the reduced density matrix at time $N\Delta t$ can be expressed as

$$\tilde{\rho}_{\alpha_N}^{(N)} = \sum_{\alpha_0, \dots, \alpha_{N-1}=1}^{n^2} \tilde{\rho}_{\alpha_0}^{(0)} G(\alpha_0, \dots, \alpha_N) F(\alpha_0, \alpha_1, \dots, \alpha_N), \quad (3.18)$$

where

$$F(\alpha_0, \alpha_1, \dots, \alpha_N) = \prod_{k=0}^N \prod_{k'=0}^k F_{\alpha_k \alpha_{k'}} \quad (3.19)$$

and

$$G(\alpha_0, \dots, \alpha_N) = \prod_{k=1}^N G_{\alpha_k \alpha_{k-1}}. \quad (3.20)$$

Notice that this directly follows from Eq. (3.11). The influence functional $F(\alpha_0, \alpha_1, \dots, \alpha_N)$ is computed using the TEMPO algorithm (see section 3.2) where $I_{\alpha_k \alpha_{k'}}$ is replaced by $F_{\alpha_k \alpha_{k'}}$ in Eq. (3.11). Analogously to the right hand side of Fig. 3.15, TEMPO can be used to obtain the matrix product state representation of the influence functional, which is depicted in Fig. 3.19 for the present case. To rewrite the system propagator as a matrix product state,

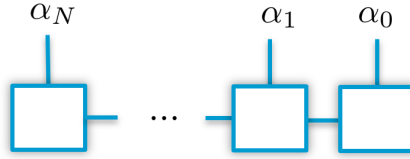


Figure 3.19: Tensor diagram of $F(\alpha_0, \alpha_1, \dots, \alpha_N)$.

we perform a singular value decomposition on each $G_{\alpha_k \alpha_{k-1}}$ such that

$$G(\alpha_0, \dots, \alpha_N) = \prod_{k=1}^N \sum_{j_k} \tilde{G}_{\alpha_k j_k}^{(k)} \tilde{G}_{\alpha_{k-1} j_k}^{(k-1)}. \quad (3.21)$$

For notational convenience, the initial system state $\tilde{\rho}_{\alpha_0}^{(0)}$ is absorbed into the matrix product state representation of the system propagator (Fig. 3.20).

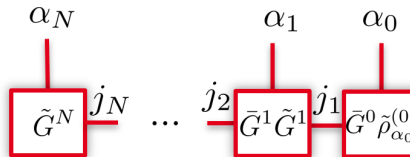


Figure 3.20: Tensor diagram of $\tilde{\rho}_{\alpha_0}^{(0)} G(\alpha_0, \dots, \alpha_N)$.

To compute the sum in Eq. (3.18) as a scalar product between the matrix product states

shown in Figs. 3.19 and 3.20, we introduce a Kronecker delta and an according sum over the index $\tilde{\alpha}_N$, and arrive at

$$\tilde{\rho}_{\alpha_N}^{(N)} = \sum_{\alpha_0, \dots, \alpha_{N-1}, \tilde{\alpha}_N=1}^{n^2} \tilde{\rho}_{\alpha_0}^{(0)} \delta_{\alpha_N \tilde{\alpha}_N} G(\alpha_0, \dots, \tilde{\alpha}_N) F(\alpha_0, \alpha_1, \dots, \tilde{\alpha}_N). \quad (3.22)$$

This expression is graphically depicted in Fig. 3.21.

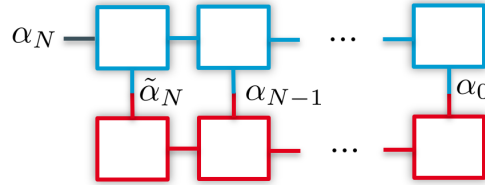


Figure 3.21: Tensor diagram of Eq.(3.22) with $\delta_{\alpha_N \tilde{\alpha}_N} F(\alpha_0, \alpha_1, \dots, \tilde{\alpha}_N)$ colored in blue and $\tilde{\rho}_{\alpha_0}^{(0)} G(\alpha_0, \dots, \tilde{\alpha}_N)$ colored in red.

In Ref. [29], the reduced density matrix for the Hamiltonian given in Eq. (3.17) at time $N\Delta t$ was shown to be

$$\tilde{\rho}_{\alpha_N}^{(N)} = \sum_{\substack{\alpha_0, \dots, \alpha_{N-1}=1 \\ \beta_0, \dots, \beta_{N-1}=1}}^{n^2} K(\alpha_0, \dots, \alpha_N, \beta_0, \dots, \beta_{N-1}) \tilde{\rho}_{\alpha_0}^{(0)} F_1(\beta_0, \beta_1, \dots, \beta_{N-1}) F_2(\alpha_0, \alpha_1, \dots, \alpha_N), \quad (3.23)$$

where $F_{1/2}[J_{1/2}(\omega)]$ denote the influence functionals corresponding to the spectral density $J_{1/2}(\omega)$ of the respective bath. The system propagator

$$K(\alpha_0, \dots, \alpha_N, \beta_0, \dots, \beta_{N-1}) = \left(\prod_{k=1}^N K(\alpha_k, \alpha_{k-1}, \beta_{k-1}) \right) \quad (3.24)$$

is given by

$$K(i_k^\pm, i_{k-1}^\pm, j_{k-1}^\pm) = \langle s_{2, i_k^\pm} | e^{-iH_S \Delta t} | s_{1, j_{k-1}^\pm} \rangle \langle s_{1, j_{k-1}^\pm} | s_{2, i_{k-1}^\pm} \rangle \langle s_{2, i_{k-1}^\pm} | s_{1, j_{k-1}^\pm} \rangle \langle s_{1, j_{k-1}^\pm} | e^{iH_S \Delta t} | s_{2, i_k^\pm} \rangle \quad (3.25)$$

where we have used the notation $\alpha := i^\pm$ and $\beta := j^\pm$.

To evaluate the path sum in terms of a tensor network, we begin by expressing the system propagator as a matrix product operator and absorb the initial state, similarly to the single bath case. The corresponding MPO is depicted in Fig. 3.22. Next, the influence functionals F_1 and F_2 are computed using the TEMPO method. The path sum in Eq. (3.23) can then be represented as a tensor diagram, as shown in Fig. 3.23. It is evaluated by first contracting the green tensors into the red tensors, which is an MPS-MPO operation. Notably, this operation is computationally far cheaper than the computation of the influence functionals, which each require N MPS-MPO operations. The computationally most demanding step is subsequently contracting the remaining two MPS-like

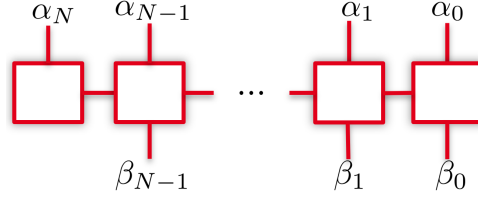


Figure 3.22: Tensor diagram of $\tilde{\rho}_{\alpha_0}^{(0)} K(\alpha_0, \dots, \alpha_N, \beta_0, \dots, \beta_{N-1})$.

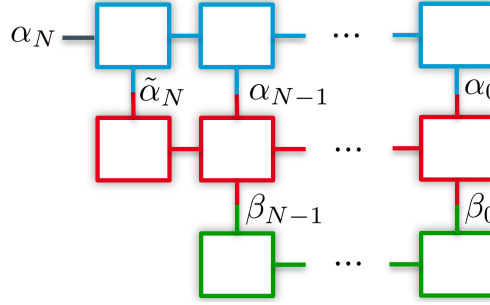


Figure 3.23: Tensor diagram of Eq. (3.23) with $\delta_{\alpha_N \tilde{\alpha}_N} F_2(\alpha_0, \alpha_1, \dots, \tilde{\alpha}_N)$ colored in blue, $\tilde{\rho}_{\alpha_0}^{(0)} K(\alpha_0, \dots, \tilde{\alpha}_N, \beta_0, \dots, \beta_{N-1})$ colored in red, and $F_1(\beta_0, \dots, \beta_{N-1})$ colored in green.

structures as each of them has the bond dimension necessary to accurately store the influence functional of the respective bath. Thus, the contraction of Eq. (3.23), when given the influence functionals and the system propagator, is approximately 8 times more computationally expensive than the last iterative step of computing an influence functional as the computational complexity of an MPS-MPS operation scales cubically in the bond dimension. For simplicity, we use the same value for the singular value cutoff λ_c for all tensor contractions involved.

3.4.1 Verification Based on Previous Results

To verify the implementation of our method, we compare our results to those of Ref. [62] that utilized the direct summation technique. There, the central two-level system

$$\hat{H}_S = \frac{\Omega}{2} \hat{\sigma}_x \quad (3.26)$$

is considered. It is initialized in the $|\uparrow\rangle$ state and coupled to two baths by the operators $\hat{s}_1 = \hat{\sigma}_x$ and $\hat{s}_2 = \hat{\sigma}_z$. The baths are characterized by the *Ohmic* spectral densities

$$J_{x/z}(\omega) = \frac{\pi}{2} \alpha_{x/z} \omega e^{-\omega/\omega_c} \quad (3.27)$$

with the coupling strengths $\alpha_{x/z}$. The high-frequency cutoff, which is set to $\omega_c = 10\Omega$, is required to ensure the integral in Eq. (2.75) is finite. The initial bath temperatures are set to $T = 0.2\Omega$, and the coupling strengths are $\alpha_x = \alpha_z = 1/32$. This setup corresponds to the parameters chosen for the black curve in Fig. 2 of Ref. [62]. We reproduce this

curve in Fig. 3.24 using the tensor network approach introduced here. We use the Trotter time-step $\Omega\Delta t = 0.6$ (as in Ref. [62]) and then converge the singular value cutoff λ_c . Similarly to the massive advantage in computational efficiency that the original TEMPO

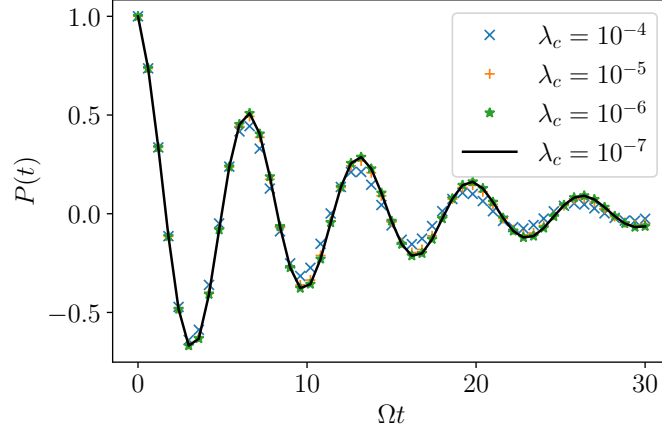


Figure 3.24: Polarization dynamics for $\alpha_x = \alpha_z = 1/32$, bath initial temperatures $T = 0.2\Omega$, bath high-frequency cut-off $\omega_c = 10\Omega$, and different values for singular value cutoff λ_c as indicated.

provides, the method developed here also offers a tremendous advantage. Specifically, the computation time required to compute the black curve of Fig. 3.24 is reduced from about a day using iterative summation [29] to just a few seconds using the tensor network contraction.

3.4.2 Quantum Zeno Disruption by Non-Commuting Baths

The special case of the model used in the previous subsection, where the system is only coupled to the σ_z -bath (i.e., $\alpha_x = 0$), is referred to as the *spin-boson model*. At an initial bath temperature of $T = 0$, the polarization dynamics is particularly well-studied. The noninteracting blip approximation (NIBA) [2] is based on the Feynman-Vernon influence functional and the subsequent approximation that a certain type of paths referred to as *blips* (see also section 2.6) decouple from each other. In the *scaling limit* $\omega_c \rightarrow \infty$, NIBA yields damped coherent oscillations for small coupling strengths α_z [55]:

$$P(t) \approx \frac{1}{1 - \alpha_z} \cos(\omega t) e^{-\gamma t} - \frac{\alpha_z}{1 - \alpha_z}. \quad (3.28)$$

The renormalized oscillation frequency is given by

$$\omega = \Omega_{\text{eff}} \cos \left[\frac{\pi \alpha_z}{2(1 - \alpha_z)} \right], \quad (3.29)$$

the dephasing rate by

$$\gamma = \Omega_{\text{eff}} \sin \left[\frac{\pi \alpha_z}{2(1 - \alpha_z)} \right], \quad (3.30)$$

and the effective level splitting by

$$\frac{\Omega_{\text{eff}}}{\Omega} = [\Gamma(1 - 2\alpha_z) \cos(\pi\alpha_z)]^{1/2(1-\alpha_z)} \left(\frac{\Omega}{\omega_c} \right)^{\alpha_z/(1-\alpha_z)}, \quad (3.31)$$

where Γ denotes the gamma function.

At $\alpha_z = 0.5$, the dynamics becomes fully incoherent (i.e., overdamped), and the exact solution obtained using NIBA is given by [55]

$$P(t) = \exp \left(-\frac{\pi \Omega^2}{2 \omega_c} t \right). \quad (3.32)$$

Upon increasing the coupling strength further, the decay rate decreases until a phase transition occurs at $\alpha_z = 1$. At this point, the two-level system remains *localized* in the initial state, i.e., $P(t) = 1$ [55]. This phenomenon can be interpreted as an example of the quantum Zeno effect [63]. The continuous observation of the central system by the bath with respect to the operator $\hat{\sigma}_z$ prevents it from leaving the eigenstate in which it was initially prepared.

For the case where $\Omega \ll \omega_c < \infty$, the polarization dynamics exhibits a similar behavior. Specifically, at $\omega_c = 10\Omega$, the transition to fully incoherent dynamics still occurs at $\alpha_z = 0.5$ [25]. However, the coupling strength at which the localization transition takes place is larger than in the scaling limit. For $\omega_c = 5\Omega$, the critical coupling strength is approximately $\alpha_z \approx 1.25$ [11]. By converging the numerical TEMPO results (similar to the approach in Section 3.3 where for every Trotter time-step Δt the singular value cut-off λ_c is converged and then Δt is decreased until convergence is reached), we obtain the polarization dynamics for exemplary coupling strengths $\alpha_z \in \{0.1, 0.2, 0.4, 0.8, 1.2\}$ at $\omega_c = 10\Omega$ (dashed lines in Fig. 3.25). Notably, the initial oscillation observed, for instance at $\alpha_z = 1.2$, is governed by ω_c . The timescale $1/\omega_c$ can be interpreted as a finite bath reaction time, causing the dynamics to resemble the undamped case at very short times.

Finally, we consider the two-bath case from the previous subsection, with coupling strengths $\alpha_x = \alpha_z = \alpha/2$. The corresponding numerical results for the polarization dynamics are shown as solid lines in Fig. 3.25. While the quantum Zeno effect slows down the dynamics upon increasing the coupling strength in the single-bath case (leading to localization), the continuous measurement of the two-level system with respect to σ_x by the additional bath disrupts this effect. Consequently, we observe a rapid decay into delocalization at strong coupling strengths. It is worth noting that the suppression of phase transitions by non-commuting fluctuations has also been observed in other mod-

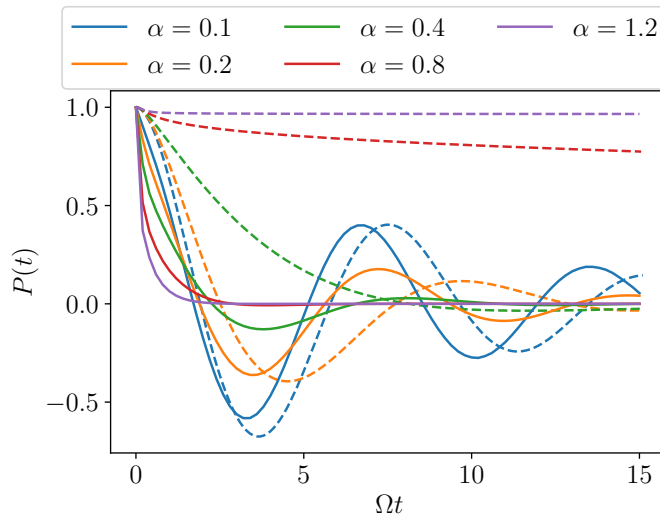


Figure 3.25: Polarization dynamics for bath initial temperatures $T = 0$, high-frequency cutoff $\omega_c = 10\Omega$, and different coupling strengths α . Solid lines: $\alpha_x = \alpha_z = \alpha/2$. Dashed lines: $\alpha_z = \alpha$ and $\alpha_x = 0$.

els [64, 65].

3.5 Summary

In section 3.1, a basic introduction to tensor networks, by following standard literature, was given. This laid the foundation for a novel, simplified derivation of the TEMPO method originally developed by Strathearn et al. [11] in section 3.2. In section 3.3, the numerical TEMPO results were validated on a single-mode model, which is trivially solved by discretizing the harmonic mode and yet poses a challenge to the TEMPO approach as the bath autocorrelation function does not decay. Furthermore, it was shown that the computational effort of TEMPO surprisingly scales quadratically with the inverse Trotter time-step. In section 3.4, a novel generalization of the TEMPO method to the case of two baths that are coupled to the central systems with operators that do not commute with each other was introduced. Stated differently, this method corresponds to evaluating the path sum derived by Palm et al. [62] in terms of a tensor network, which exponentially improves the numerical efficiency. Subsequently, the implementation of the novel method was validated by comparison with previous results and then used to study the disruption of the localization transition in the Ohmic spin-boson model at zero temperature caused by a second bath.

In chapter 6, we will also address vibronic dynamics near a conical intersection in terms of a spin-boson model with two non-commuting baths that have a structured spectral density. For reasons of computational efficiency, this case will, however, be treated with the hierarchical equations of motion technique.

4 Hidden Phase of the Spin-Boson Model

The sub-Ohmic spin-boson model has been studied extensively in the literature [2, 15, 20, 23, 24, 66, 67]. Despite this, the dynamical phase diagram for a finite bath cut-off frequency and zero temperature had remained an open problem, particularly for small spectral exponents $s < 0.5$ [15, 23, 24]. While the highly non-Markovian dynamics of the sub-Ohmic regime could not be fully converged for the entire parameter space using the iterative QUAPI approach in Ref. [23] and the SMatPI approach in Ref. [52], we here present numerically exact TEMPO results and thereby resolve the issue of the dynamical phase diagram [25].

In section 4.1, the literature on the dynamical phase diagram of the sub-Ohmic spin-boson model is discussed. In section 4.2, we follow Ref. [25], which emerged from the work on this thesis, and consider the spin-boson model

$$\hat{H} = \hat{H}_S + \hat{H}_B + \hat{H}_{\text{int}} = \frac{\Omega}{2} \hat{\sigma}_x + \sum_j \left[\frac{\hat{p}_j^2}{2m_j} + \frac{1}{2} m_j \omega_j^2 \left(\hat{x}_j - \frac{c_j \sigma_z}{m_j \omega_j^2} \right)^2 \right] \quad (4.1)$$

with the bath spectral density

$$J(\omega) = \frac{\pi}{2} \alpha \frac{\omega^s}{\omega_c^{s-1}} e^{-\omega/\omega_c} \quad (4.2)$$

and (sub-)Ohmic *spectral exponent* $0 \leq s \leq 1$. In order to keep the coupling strength α dimensionless for all s , an additional factor of ω_c^{1-s} is included in the spectral density. The bath is initialized at zero temperature in the following. We obtain the polarization dynamics $P(t)$ by using the TEMPO technique. This involves converging the singular value cutoff λ_c for increasingly smaller Trotter time-steps Δt until convergence is found. Fig. 4.1 illustrates this process for the numerically challenging case of strong coupling to a sub-Ohmic bath with a small spectral exponent.

4.1 Previous Publications

In Ref. [23], a phase diagram of the spin-boson model was sketched based on all available knowledge at the time. This sketch, shown in Fig. 4.2, includes noninteracting blip approximation (NIBA) results [2] for the Ohmic case ($s = 1$) in the scaling limit $\omega_c \rightarrow \infty$, as previously discussed in section 3.4.2. For the sub-Ohmic case ($s < 1$), the coupling

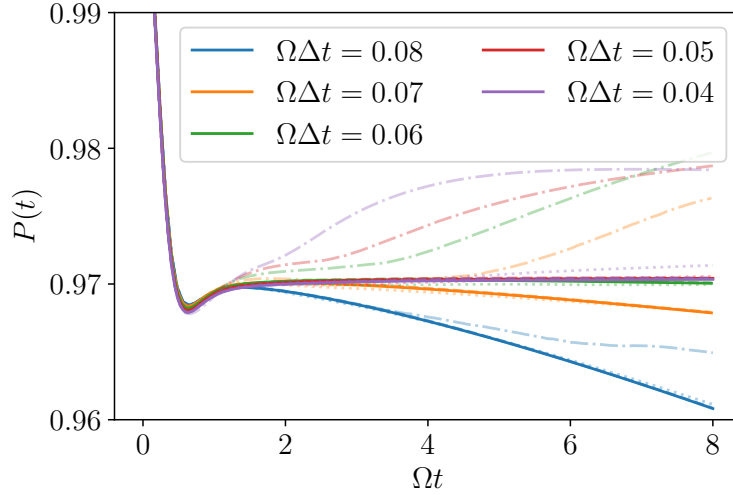


Figure 4.1: Polarization $P(t)$ obtained using TEMPO for $T = 0$, $s = 0.3$, $\alpha = 0.8$, $\omega_c = 10\Omega$, and various values for the Trotter time-step Δt . Dashdotted, dotted, dashed, and solid lines correspond to $\lambda_c = 10^{-5}$, $\lambda_c = 10^{-6}$, $\lambda_c = 10^{-7}$, and $\lambda_c = 10^{-8}$ respectively. Note that the dashed lines are only barely visible as they almost perfectly align with the solid lines.

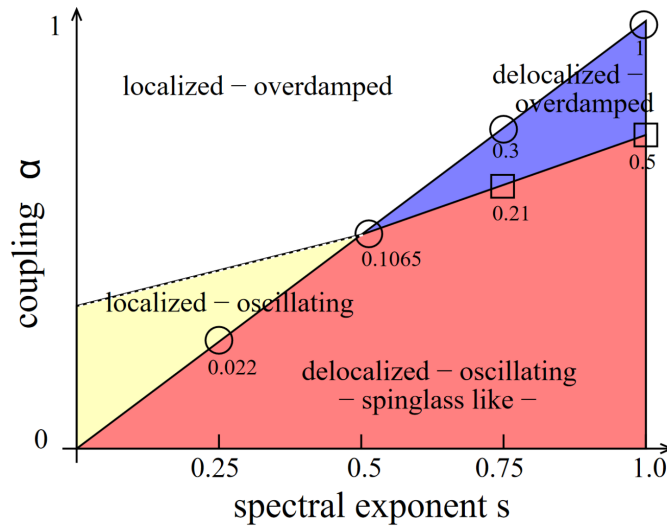


Figure 4.2: Sketch of a phase diagram of the sub-Ohmic spin-boson model at $T = 0$, taken from Ref. [23]. The circles mark the localization transition while the squares mark the transition from coherent to incoherent dynamics.

strengths at which the localization transition occurs (for the case of a hard high-frequency cutoff $\omega_c = 10\Omega$, i.e., $J(\omega) = 0$ for $\omega > \omega_c$) are indicated below the circles. The corresponding data was taken from Ref. [67] and is based on quantum Monte Carlo simulations. The transition from oscillatory to overdamped dynamics is commonly defined to take place when the local extrema in the dynamics vanish. The corresponding data point for the critical coupling strength at $s = 0.75$ was taken from Ref. [66] and is based on a perturbation approach (where also a finite $\omega_c = 10\Omega$ is employed). By use of the the

iterative QUAPI method, as explained in detail in section 2.7, it was found in Ref. [23] that oscillatory dynamics still occurs in the localized phase for spectral exponents $s \leq 0.5$ and the largest coupling strength where numerical convergence could be achieved. Furthermore, it was speculated that this oscillatory behavior would vanish at even stronger coupling strengths. However, as will be demonstrated in section 4.2, this is not the case. Rather, the oscillatory dynamics persists to arbitrarily large coupling strengths for any s , as it is an artifact of the high-frequency cutoff in the bath spectral density.

In Ref. [24], the transition to incoherent dynamics for $s \geq 0.5$ and $\omega_c = 10\Omega$ and polarized initial conditions (see Section 2.5) was studied in more quantitative detail using a path integral Monte Carlo technique. This study led to the dashed phase separation line shown in Fig. 4.3. Additionally, the phase separation line for localization was again taken

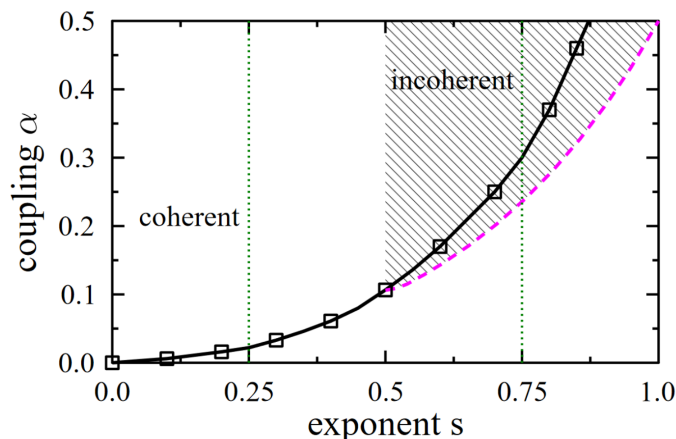


Figure 4.3: Sketch of a phase diagram of the sub-Ohmic spin-boson model at $T = 0$ with polarized initial conditions, taken from Ref. [24]. Black solid line marks the localization transition while the pink line marks the transition from coherent to incoherent dynamics.

from Ref. [67].

However, in section 4.2, we demonstrate that the timescale of the oscillations observed at small s and strong coupling strength is given by ω_c^{-1} and not by Ω^{-1} . Therefore, it should not be referred to as coherent dynamics, which commonly refers to the inherent coherence of the central system. Furthermore, Fig. 4.3 may be misinterpreted to imply a phase separation line between coherent and incoherent dynamics at $s = 0.5$, which we show to be absent in section 4.2.

In Ref. [15], the localization transition and the transition from coherent to incoherent dynamics were studied for the unpolarized initial condition using an extended hierarchical equation of motion technique. The resulting phase diagram is shown in Fig. 4.4. There, the transition from coherent to incoherent dynamics was defined to occur at the coupling strength at which the first local minimum of the polarization dynamics vanishes. The corresponding critical coupling strength was then calculated for $s > 0.5$ while for smaller s it was shown that the minimum does not vanish even at very strong cou-

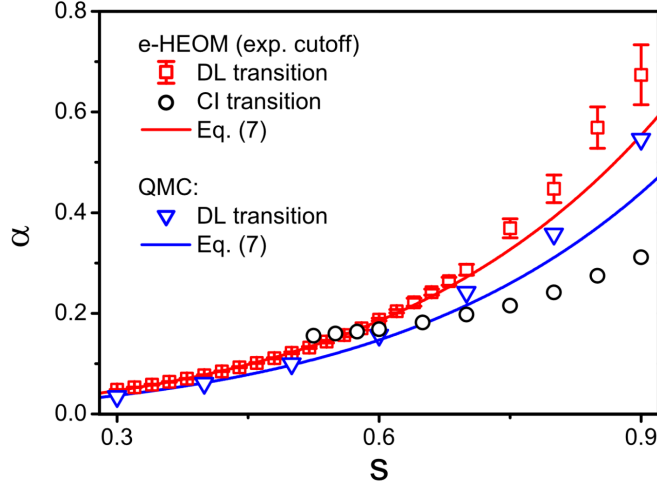


Figure 4.4: Sketch of a phase diagram of the sub-Ohmic spin-boson model at $T = 0$ and $\omega_c = 20\Omega$, taken from Ref. [15]. The coupling strengths at which the localization transition takes place are marked by red boxes as obtained from an extended hierarchical equation of motion technique and blue triangles using the Quantum Monte Carlo data from Ref. [67]. Solid lines show a fit of the corresponding data. Black circles mark the transition from coherent to incoherent dynamics as obtained from the extended hierarchical equation of motion technique.

pling.

4.2 Dynamical Phase Diagram

We now consider the unpolarized initial condition given in Eq. (2.41) and high-frequency bath cutoff frequency $\omega_c = 10\Omega$. In alignment with previous findings at $s = 0.7$, we observe damped oscillatory polarization dynamics with multiple minima and maxima at weak coupling strength, as shown in Fig. 4.5. Since the timescale of these oscillations is given by Ω^{-1} , we also refer to this regime as the coherent regime. As expected, the oscillations vanish, and the dynamics becomes incoherent (i.e., overdamped) upon increasing the coupling strength.

Surprisingly, upon further increasing the coupling strength, we encounter a shallow local minimum in the dynamics, which is not followed by a maximum. This qualitatively different behavior suggests the presence of a novel phase. To investigate the phase separation line implied by Fig. 4.3 at $s = 0.5$, we vary the spectral exponent for a strong coupling strength $\alpha = 0.8$, as shown in in Fig. 4.6. Interestingly, for all the spectral exponents considered, the dynamics is characterized by a single minimum, and we do not observe a transition at $s = 0.5$, contrary to what one might expect from Fig. 4.3.

Next, we investigate how the polarization dynamics changes when varying the coupling strength for a fixed $s = 0.3$, as depicted in Fig. 4.7. At small coupling strengths, we find coherent oscillations with minima and maxima on the timescale of Ω^{-1} . At strong

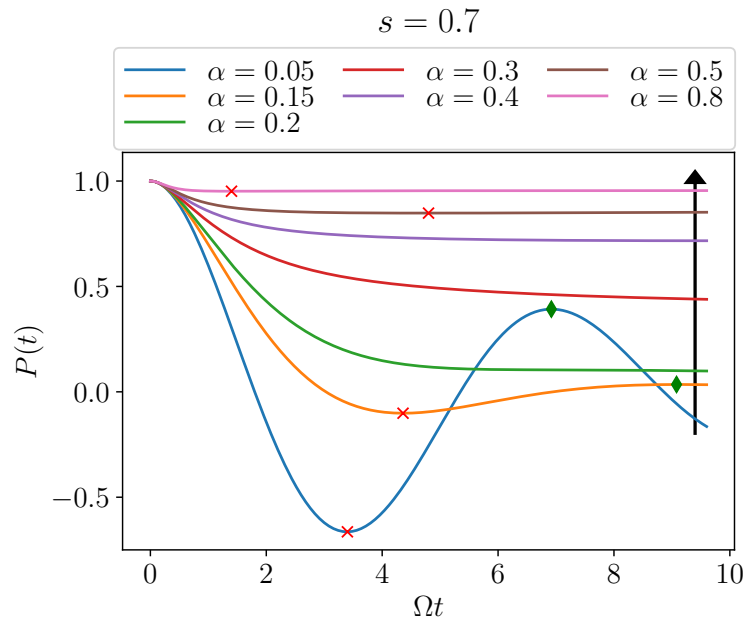


Figure 4.5: Polarization $P(t)$ for $T = 0$, $s = 0.7$, and various coupling strengths α (published in Ref. [25]). The arrow intersects the lines in ascending order of coupling strengths. Local minima (maxima) are marked by a red cross (green diamond).

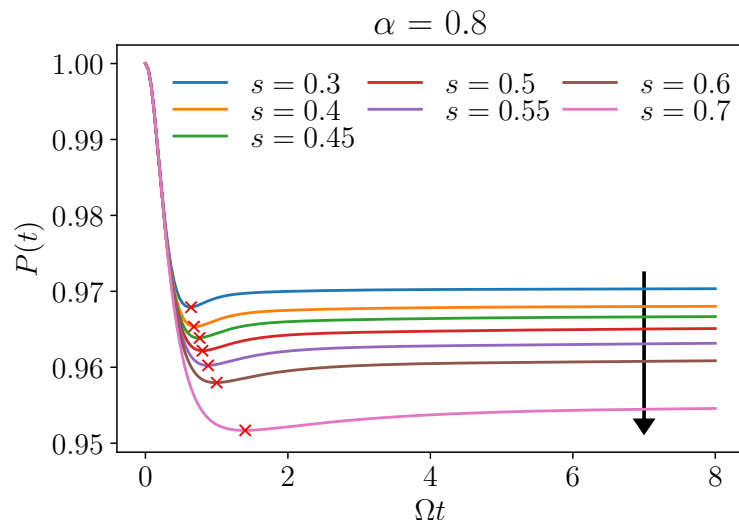


Figure 4.6: Polarization $P(t)$ for $T = 0$, $\alpha = 0.8$, and various spectral exponents s (published in Ref. [25]). The arrow intersects the lines in ascending order of spectral exponents. Local minima are marked with a red cross.

coupling strengths, all minima and maxima except for a single shallow minimum vanish. This behavior resembles what we have observed at $s = 0.7$ (see Fig. 4.5), except for the absence of the fully incoherent phase.

To further characterize the novel phase found at the strongest coupling strengths, we plot the quantity $1 - P(t)$ against the rescaled time $\omega_c t$ for various values of ω_c in Fig. 4.8.

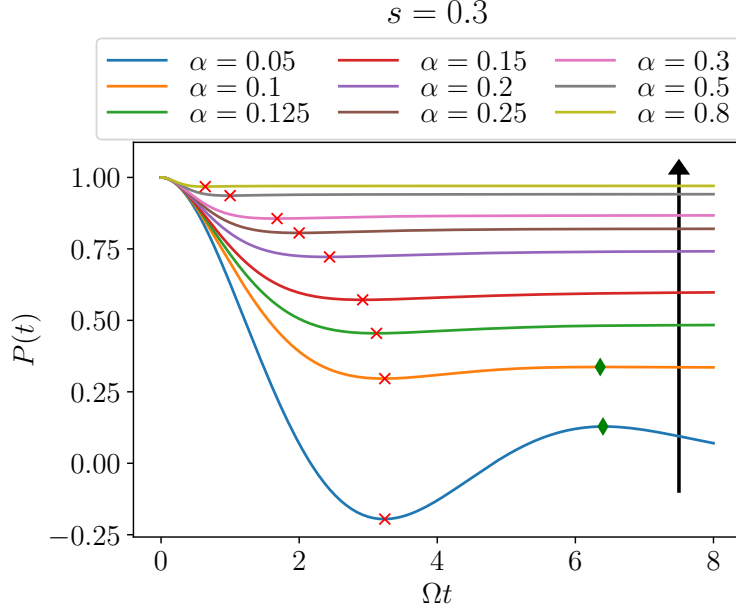


Figure 4.7: Polarization $P(t)$ for $T = 0$, $s = 0.3$, and various coupling strengths α (published in Ref. [25]). The arrow intersects the lines in ascending order of coupling strengths. Local minima (maxima) are marked by a red cross (green diamond).

We find that the minimum in $P(t)$ always occurs at a time $t_{\min} \simeq \text{const.}/\omega_c$ for suffi-

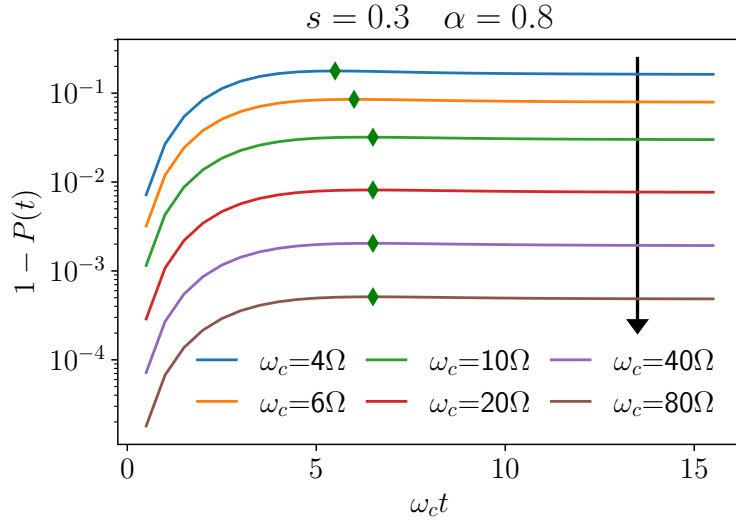


Figure 4.8: Polarization $1 - P(t)$ for $T = 0$, $\alpha = 0.8$, $s = 0.3$, and various bath cutoff frequencies ω_c (published in Ref. [25]). The arrow intersects the lines in ascending order of cutoff frequencies. Local maxima are marked with a green diamond. Note that the $\omega_c = 10\Omega$ line corresponds to the $s = 0.3$ line in Fig. 4.6.

ciently large values of ω_c . This indicates that the oscillatory behavior at strongest coupling strength is purely bath-driven and therefore distinct from the coherent oscillations

on the timescale Ω^{-1} found at weak coupling strengths. For this reason, we refer to this novel phase as *pseudo-coherent*. In the scaling limit $\omega_c \rightarrow \infty$, the oscillatory motion vanishes and the dynamics becomes fully incoherent.

In summary, we have observed three distinct phases. At weak coupling strength, coherent dynamics takes place irrespective of the spectral exponent. For $s = 0.7$, we have observed that the dynamics becomes fully overdamped (referred to as incoherent) at first and then pseudo-coherent upon increasing the coupling strength. For $s = 0.3$, the fully overdamped phase does not exist; instead, the dynamics becomes pseudo-coherent directly when increasing the coupling strength out of the coherent phase. By examining the full parameter space of $0 \leq s \leq 1$ and α , we construct the dynamical phase diagram shown in Fig. 4.9. For the transition from the coherent to the incoherent domain, we use

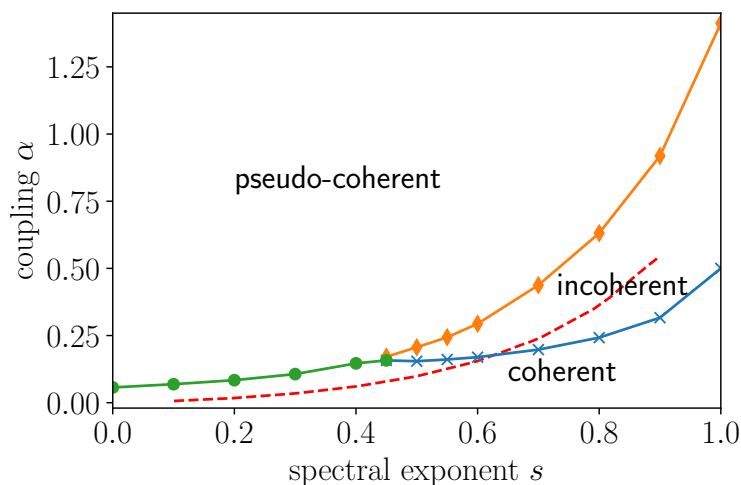


Figure 4.9: Phase diagram of the (sub-)Ohmic spin-boson model at $T = 0$ and $\omega_c = 10\Omega$ (similar to figure published in Ref. [25]). The symbols represent coupling strengths $\alpha(s)$ at which a transition occurs and are linearly interpolated for better visibility. The localization transition is marked as a dashed red line with data taken from Ref. [67].

that same criterion as in Ref. [15], and hence track the first local minimum while increasing coupling strength until it vanishes at the critical coupling strength. These critical coupling strengths are marked as blue crosses in Fig. 4.9.

The coupling strengths at which local minima reappear within $\Omega t < 8$ are marked as orange diamonds in Fig. 4.9. This choice of timescale is due to computational limitations: the computational complexity of TEMPO scales rapidly with the number of time steps, and simultaneously, the minima of the pseudo-coherent phase (which first appear at later times for smaller coupling strengths) become increasingly shallow. This necessitates smaller Trotter time-steps and larger singular value cutoffs. However, as the pseudo-coherent minima get rapidly renormalised to later times when approaching the phase boundary (as seen in Fig. 4.10), the retrieved values for the critical coupling strengths should not significantly differ from considering all times $\Omega t < \infty$.

The coupling strengths at which the first local maxima vanish when transitioning directly from the coherent to the pseudo-coherent domain are marked as green circles in Fig. 4.9. To contextualize the obtained dynamical phase diagram, we also show the coupling strengths at which the localization transition occurs (as obtained by Quantum Monte Carlo simulations in Ref. [67]) as a dashed red line in Fig. 4.9.

The case $s = 0.45$, as depicted in Fig. 4.10, is particularly insightful. There, we observe

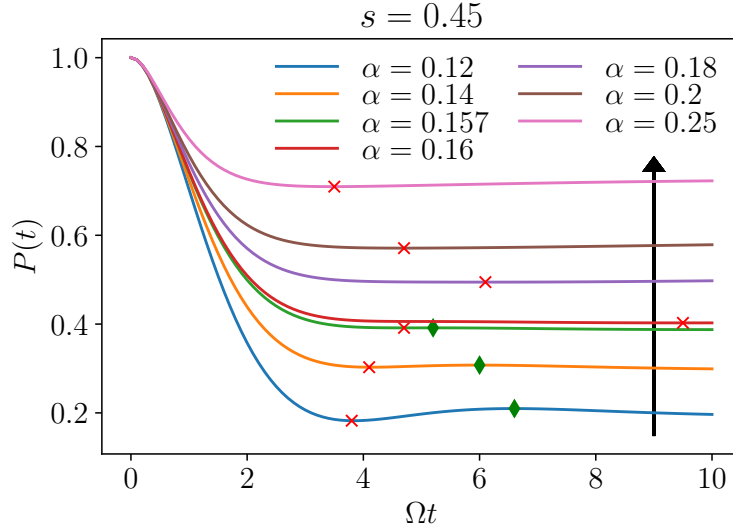


Figure 4.10: Polarization $P(t)$ for $T = 0$, $s = 0.45$, and various coupling strengths α (published in Ref. [25]). The arrow intersects the lines in ascending order of coupling strengths. Local minima (maxima) are marked with a red cross (green diamond).

that the first minimum and maximum of the coherent dynamics merge upon sufficiently increasing the coupling strength. Subsequently, the minimum of the pseudo-coherent phase appears at a much later time upon further increasing the coupling strength. This underscores the distinctiveness of the coherent and the pseudo-coherent phases.

Finally, for the polarized initial condition employed in Ref. [24], we find that the oscillatory dynamics observed at strongest coupling is governed by the timescale ω_c^{-1} and is thus fully induced by the bath (i.e., pseudo-coherent), as shown in Fig. 4.11 (a). The observed maxima in $P(t)$ result from a renormalization of the oscillation frequency due to the polarized initial condition compared to the unpolarized initial condition. Furthermore, Fig. 4.11 (b) demonstrates that there is no transition occurring at $s = 0.5$ and strong coupling, contrary to what one might expect from Fig. 4.3.

Motivated by the work presented in this chapter, the dependence of the phase diagram on the initial preparation has been studied in more detail in Ref. [68]. However, the phase diagrams obtained there differs slightly from ours due to a distinct definition of the transition to the pseudo-coherent phase, which utilizes the oscillatory frequency renormalization induced by the bath. As this definition is more sensitive to the influence of the bath, the pseudo-coherent phase already appears at slightly weaker coupling strengths

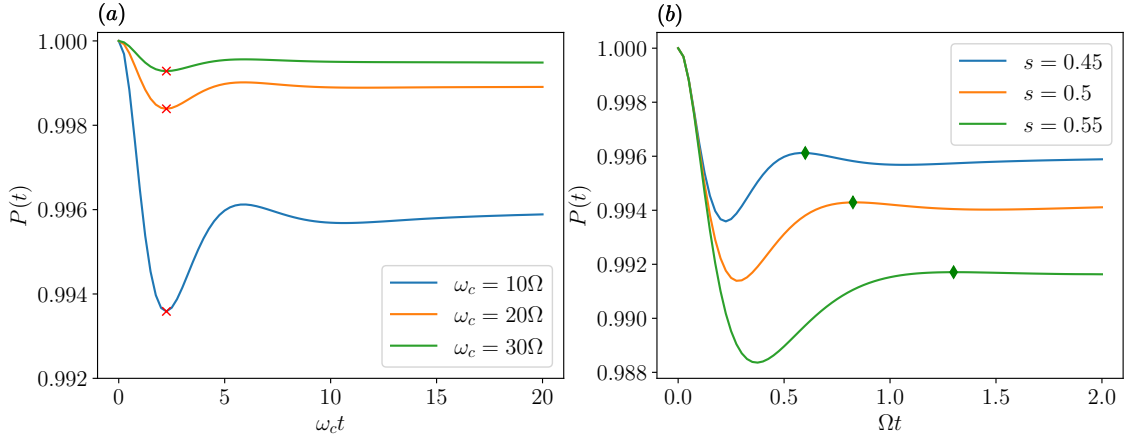


Figure 4.11: Polarization $P(t)$ obtained using TEMPO for polarized initial conditions at $T = 0$ and $\alpha = 0.5$ (published in Ref. [25]). (a) Spectral exponent $s = 0.45$ and various bath high-frequency cutoffs ω_c . Local minima are marked with a red cross. (b) Bath high-frequency cutoff $\omega_c = 10\Omega$, and various spectral exponents s . Local maxima are marked with a green diamond.

compared to the criterion employed in this work. Qualitatively however, one always finds the coherent phase at weak and the pseudo-coherent phase at strong coupling with an incoherent phase in between them for $s \gtrsim 0.5$.

4.3 Summary

In section 4.1, an overview of the literature on the dynamical phase diagram of the sub-Ohmic spin-boson model was given. Crucially, it had been unclear whether coherent dynamics takes place for $s \lesssim 0.5$ and strong coupling strength. In section 4.2, this issue was resolved by using the numerically exact TEMPO approach to identify a novel *pseudo-coherent* phase characterized by oscillatory dynamics even at strong coupling strengths. The frequency related to the oscillation in this phase is proportional to the bath cut-off frequency. Therefore, the oscillatory motion is not generated by the two-level system but by the bath. Finally, a corresponding phase diagram of the sub-Ohmic spin-boson model was given and its dependence on the initial conditions was discussed.

5 $1/f$ Quantum Noise in the Spin-Boson Model

Experiments on superconducting qubits have shown that magnetic flux noise has a spectrum with strongly pronounced low-frequency modes of the form $J(\omega) \propto \omega^s$ with $s < 0$ [27]. With this property, it falls in the category of $1/f$ noise, the microscopic origin of which is not always clear in all systems [69]. A common source of $1/f$ noise can be described by few two-level fluctuators, which cannot be modeled by a spin-boson model [69]. In this case, the theoretical description is restricted to weak coupling or high temperature, employing highly non-trivial approximate methods [70] and is thus beyond the scope of this work. Instead, we consider the continuum limit here, where a treatment in terms of the spin-boson model is justified. An example of this is the electronic spin of a color center that couples to the vibrational motion of hexagonal boron nitride membranes, which has been addressed in terms of the spin-boson model with $s = -1$ using approximate numerical tools [28].

The purpose of this chapter is to provide numerically exact TEMPO results for the highly non-Markovian $1/f$ quantum noise regime of the spin-boson model, which amounts to an extension of the work presented in chapter 4 to the case $s < 0$. To this end, we present the extended phase diagram in section 5.1 and compute dephasing rates at weak coupling in section 5.2. In section 5.3, we briefly comment on the reorganization energy of the bath. As it diverges for $s \leq 0$, which is the reason why this case had originally been viewed as pathological [2], we introduce a low-frequency cutoff in the spectral density, which is justified by experimental evidence [27].

The decisive quantity on which QUAPI and thus TEMPO depend, as previously derived in Eq. (2.75), is given by

$$Q(t) = \frac{1}{\pi} \int_0^\infty d\omega \frac{J(\omega)}{\omega^2} \left[\coth\left(\frac{\omega\beta}{2}\right) (1 - \cos(\omega t)) + i(\sin(\omega t) - \omega t) \right]. \quad (5.1)$$

The low-frequency cutoff ω_{ir} with $J(\omega) = 0$ for $\omega < \omega_{\text{ir}}$ ensures that the divergence of $Q(t)$ for $s \leq 0$ at finite temperature and $s \leq -1$ at zero temperature is lifted.

5.1 Extended Phase Diagram

Fig. 5.1 depicts the extension of the sub-Ohmic phase diagram of Fig. 4.9 to the $1/f$ regime down to $s = -0.75$, which is the smallest spectral exponent where numerical convergence could be achieved. In the $1/f$ quantum noise regime, the dynamics behaves

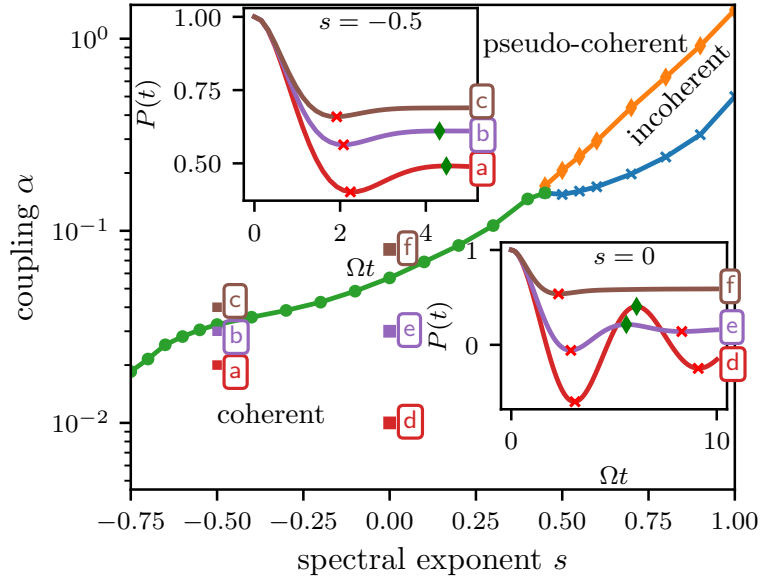


Figure 5.1: Phase diagram of the spin-boson model at $T = 0$ and $\omega_c = 10\Omega$. The green line represents the transition from coherent to pseudo-coherent behavior. The blue line represents transition from coherent to incoherent behavior. The orange line represents the transition from incoherent to pseudo-coherent behavior. Top left inset: Polarization dynamics for $s = -0.5$ and $\alpha \in \{0.02, 0.03, 0.04\}$ with minima (maxima) marked by a red cross (green diamond) showing the transition from coherent to pseudo-coherent phase. Bottom right inset: Polarization dynamics for $s = 0$ and $\alpha \in \{0.01, 0.03, 0.08\}$.

qualitatively similar to the sub-Ohmic regime: it exhibits a transition to pseudo-coherent dynamics upon increasing the coupling strength out of the coherent phase, as previously shown for $0 \leq s \leq 0.45$. Surprisingly, we observe an inflection point in the critical coupling strength $\alpha(s)$ at $s \approx -0.5$. As an illustrative example of the characteristic pseudo-coherent dynamics deep in the $1/f$ regime, we show the case $s = -0.7$ in Fig. 5.2.

5.2 Dephasing Rate

At weak coupling, the polarization dynamics exhibits damped oscillations, with NIBA yielding Eq. (3.28) in the Ohmic case $s = 1$. Furthermore, we find that Eq. (3.28) fits our numerical data well over a wide range of spectral exponents and temperatures in the weak coupling regime when α , ω , and γ are used as free parameters. Illustrative fits for the case $s = -0.5$ and zero temperature are shown in the inset of Fig. 5.3. From these fits, we extract the dephasing rates γ for weak coupling, resulting in a linear dependence of

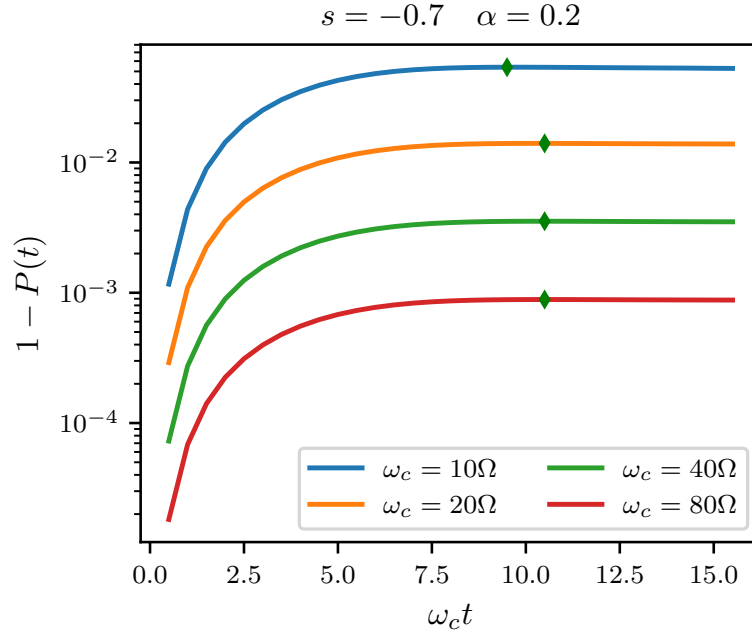


Figure 5.2: Polarization $1 - P(t)$ for $T = 0$, $\alpha = 0.2$, $s = -0.7$, and different bath cutoff frequencies ω_c . Local maxima are marked with a green diamond.

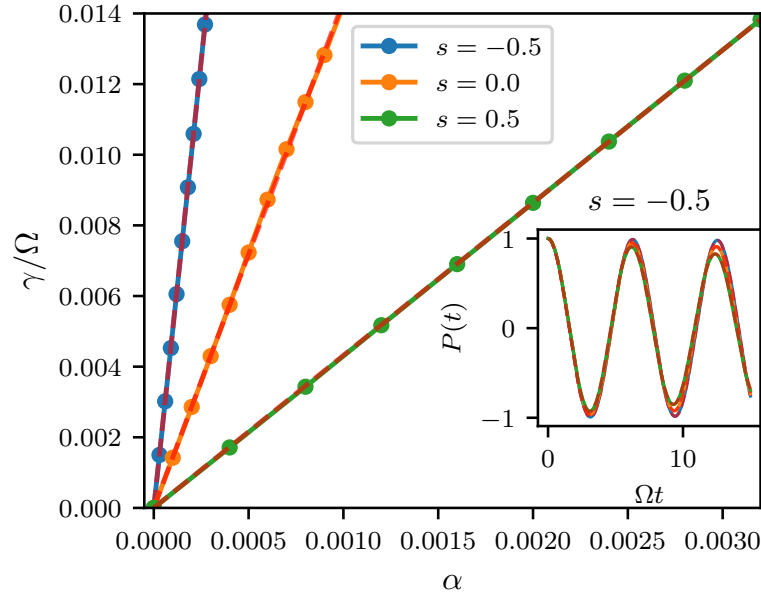


Figure 5.3: Dephasing rates as a function of coupling strength for $T = 0$ for different spectral exponents with linear fit (dashed lines). Inset: Polarization dynamics for $s = -0.5$ and $\alpha \in \{3 \cdot 10^{-5}, 1.5 \cdot 10^{-4}, 3 \cdot 10^{-4}\}$ fitted with function given in Eq. (3.28) (dashed lines).

the dephasing rates on the coupling strength (see Fig. 5.3). We then compute $\gamma'(\alpha)|_{\alpha=0}$ for various spectral exponents and temperatures by performing linear fits on the function $\gamma(\alpha)$, as presented in Fig. 5.4. In the sub-Ohmic regime ($s \geq 0$), the temperature depen-

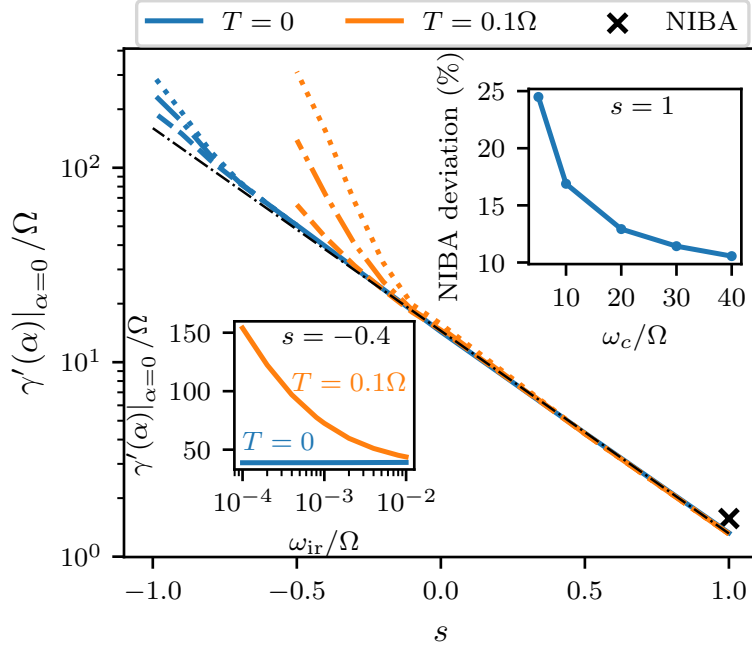


Figure 5.4: Slope $\gamma'(\alpha)|_{\alpha=0}$ as a function of the spectral exponent for temperatures $T = 0$ and $T = 0.1\Omega$ and low-frequency cutoffs $\omega_{\text{ir}} = 0$ (solid lines), $\omega_{\text{ir}} = 10^{-4}$ (dotted lines), $\omega_{\text{ir}} = 10^{-3}$ (dash-dotted lines), and $\omega_{\text{ir}} = 10^{-2}$ (dashed lines). The thin dash-dotted black line corresponds to Eq. (5.2). Bottom left inset: $\gamma'(\alpha)|_{\alpha=0}$ as a function of the low-frequency cutoff for $s = -0.4$ and temperatures as indicated. The black cross marks the NIBA result $\gamma'(\alpha)|_{\alpha=0}^{\text{NIBA}} = \Omega\pi/2$. Top right inset: relative deviation of TEMPO from NIBA $1 - \gamma'(\alpha)|_{\alpha=0}/\gamma'(\alpha)|_{\alpha=0}^{\text{NIBA}}$ as a function of high-frequency cutoff for $s = 1$.

dence is negligible, whereas in the $1/f$ noise regime ($s < 0$), the temperature dependence becomes significant. Furthermore, despite the divergence of the integral in Eq. (2.75) for $s = 0$ at finite temperature, the dynamics is almost independent of the low-frequency cutoff. However, for smaller values of s , the dephasing rates can become arbitrarily large by choosing a corresponding small low-frequency cutoff. Thus, the low-frequency cutoff plays a crucial role in determining the amount of dephasing caused by the environment. In any measurement, the low-frequency cutoff is a characteristic parameter of the experimental setup, as observed in Ref. [27]. We empirically find the dephasing rate

$$\gamma \approx 14.5\alpha e^{-2.4s} \quad (5.2)$$

from the data in Fig. 5.4 for $\alpha \ll 1$ and $\omega_{\text{ir}} = 0$. This result is valid for $s \gtrsim 0$ at finite temperatures and for $s \gtrsim -0.5$ at zero temperature. The deviation of our numerical results from the NIBA value of $\gamma'(\alpha)|_{\alpha=0}^{\text{NIBA}} = \Omega\pi/2$ (which directly follows from Eq. (3.30)) for $s = 1$ arises from the finite high-frequency cutoff (see top right inset of Fig. 5.4). Thus, while Eq. (5.2) has been generated from data with high-frequency cutoff $\omega_c = 10\Omega$, it also yields an approximation of the dephasing rate for a wide range of different ω_c due

to the weak dependence of the dynamics on the high-frequency cutoff at weak coupling.

5.3 Reorganization Energy

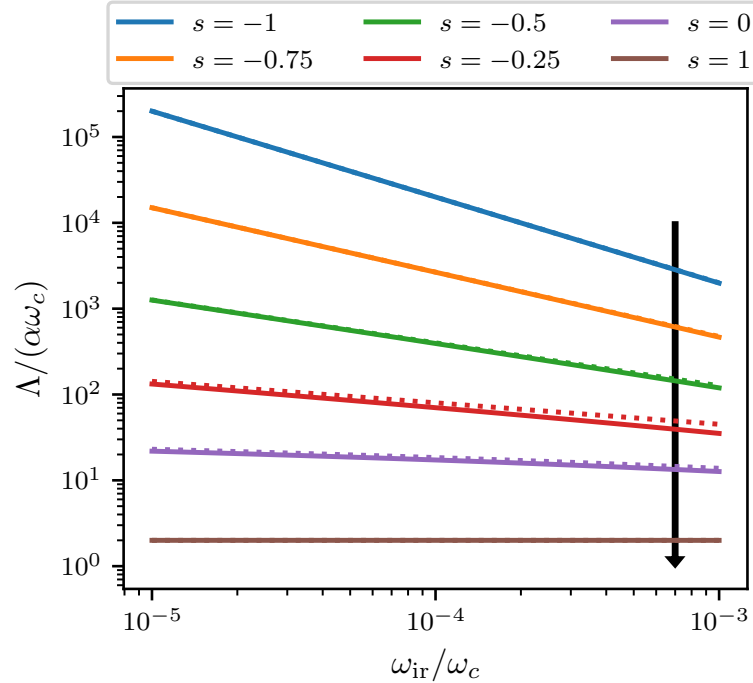


Figure 5.5: Reorganization energy Λ as a function of $\omega_{\text{ir}}/\omega_c$ for $s \in \{-1, -0.75, -0.5, -0.25, 0, 1\}$. Solid lines show exact value for Λ while dotted lines show approximation given on the right-hand side of Eq. (5.3). The arrow intersects the lines in ascending order of s

A further quantity to characterize the impact of the environment is the reorganization energy, which quantifies the energy contained in the bath fluctuations [55]. It is given by

$$\Lambda = \int_{\omega_{\text{ir}}}^{\infty} d\omega \frac{J(\omega)}{\omega} \underset{\omega_{\text{ir}} \ll \omega_c}{\approx} 2\alpha\omega_c \cdot \begin{cases} -\frac{1}{s} \left(\frac{\omega_{\text{ir}}}{\omega_c}\right)^s & s < 0 \\ -\ln\left(\frac{\omega_{\text{ir}}}{\omega_c}\right) & s = 0, \\ \Gamma(s) & s > 0 \end{cases} \quad (5.3)$$

as shown in Fig. 5.5, where $\Gamma(s)$ denotes the gamma function. For $s \leq 0$, it diverges in the limit $\omega_{\text{ir}} \rightarrow 0$. Nonetheless, as shown in Fig. 5.4, we find the polarization dynamics to be well-defined in the limit $\omega_{\text{ir}} \rightarrow 0$ for at least some $s < 0$ at zero temperature.

5.4 Summary

In section 5.1, the dynamical phase diagram computed in chapter 4 was extended to the regime of spectral exponents $s < 0$, where no qualitative change in the dynamical

behavior compared to the sub-Ohmic regime was found. In section 5.2, the dephasing rate at weak coupling strengths for the entire parameter space $-1 \leq s \leq 1$ for finite and zero temperature was studied, and an empirical formula for the dephasing rate was given. For the Ohmic case, it was shown that the deviation of the numerically exact TEMPO results from the non-interacting blip approximation is due to the finite bath high-frequency cut-off. Despite the divergence of the bath reorganization energy, as shown in section 5.3, the dephasing rate was shown to be well-defined for parts of the parameter space, while in others it was shown to depend on the experimentally realistic choice of a bath low-frequency cut-off.

6 Coherent Ultrafast Stimulated X-Ray Raman Spectroscopy of Dissipative Conical Intersections

A particularly interesting application of the spin-boson model is the vibronic dynamics around a conical intersection in polyatomic molecules. As it involves a large change in the energy gap on an ultrashort timescale, its direct spectroscopical observation is extremely challenging. The transient redistribution of ultrafast electronic coherences in attosecond Raman signals (TRUECARS) technique utilizes a combination of broadband and narrowband X-ray pulses to achieve both the required spectral and temporal resolution. Previously, TRUECARS had only been studied theoretically for isolated quantum systems [39–42]. The purpose of this chapter is to study the TRUECARS signal under the dissipative effects caused by the fluctuating charges of solvent molecules and the fluctuating nuclei of the molecular host.

While the novel method presented in section 3.4 had originally been intended to tackle this problem, the hierarchical equations of motion (HEOM) technique [12] has turned out to be computationally far more efficient for the parameters chosen, as shown in section 6.1. In section 6.2, the two-state two-mode model is introduced and mapped to an effective spin-boson model, and in section 6.3, the effect of dissipation on the TRUECARS signal is analyzed.

6.1 Hierarchical Equations of Motion (HEOM)

HEOM is a numerically exact method to compute the dynamics of the reduced density matrix in the Caldeira-Leggett model (as described by Eq. 2.36), which has originally been derived by Tanimura and Kubo [12] from the Feynman-Vernon influence functional given in Eq. 2.46. In this work, we have made use of its implementation in the QuTiP library [71, 72].

Following the presentation in Ref. [72], we define the superoperators

$$\hat{A}^\times := [\hat{A}, \cdot] \quad (6.1)$$

$$\hat{A}^\circ := \{\hat{A}, \cdot\} \quad (6.2)$$

in terms of the commutator and anticommutator. The *Liouvillian* is defined by

$$\mathcal{L} := -i\hat{H}_S^\times, \quad (6.3)$$

allowing us to write the von-Neumann equation as

$$\dot{\rho}(t) = \mathcal{L}\rho(t). \quad (6.4)$$

The real and imaginary parts of the bath autocorrelation function (Eq. (2.61))

$$L(t) = L_R(t) + iL_I(t) \quad (6.5)$$

are approximated by

$$L_R(t) = \sum_{k=1}^{N_R} c_k^R e^{-\gamma_k^R t} \quad (6.6)$$

$$L_I(t) = \sum_{k=1}^{N_I} c_k^I e^{-\gamma_k^I t} \quad (6.7)$$

using the parameters c_k^j and γ_k^j , along with the convergence parameters N_j for $j \in \{R, I\}$. Analyzing the temporal derivatives of the Feynman-Vernon influence functional [12] yields the hierarchical equations of motion [72]

$$\begin{aligned} \dot{\rho}^n(t) = & \left(\mathcal{L} - \sum_{j=R,I} \sum_{k=1}^{N_j} n_{jk} \gamma_k^j \right) \rho^n(t) \\ & - i \sum_{k=1}^{N_R} c_k^R n_{Rk} \hat{s}^\times \rho^{n_{Rk}^-}(t) + \sum_{k=1}^{N_I} c_k^I n_{Ik} \hat{s}^\circ \rho^{n_{Ik}^-}(t) - i \sum_{j=R,I} \sum_{k=1}^{N_j} \hat{s}^\times \rho^{n_{jk}^+}(t). \end{aligned} \quad (6.8)$$

Here, n is a tuple with $n = (n_{R1}, n_{R2}, \dots, n_{RN_R}, n_{I1}, n_{I2}, \dots, n_{IN_I}) \in \{0, 1, \dots, N_c\}^{N_R+N_I}$, where the *hierarchy depth* $N_c \in \mathbb{N}$ is a convergence parameter. The reduced density is denoted by $\rho^{(0,\dots,0)}(t)$, while all other ρ^n with $n \neq (0, \dots, 0)$ are referred to as *auxiliary density matrices* that are not directly linked to physical observables. The notation n_{jk}^\pm refers to the tuple n where the element n_{jk} is raised/lowered by one. A significant advantage of HEOM is that it - unlike QUAPI - straightforwardly generalizes to multiple baths with different coupling operators \hat{s} by adding corresponding additional terms to Eq. (6.8).

6.1.1 Benchmark

To validate our numerical results, we consider the model studied in Ref. [47], where effectively the spin-boson model

$$\hat{H} = \frac{\Omega}{2} \hat{\sigma}_x + \sum_j \left[\frac{\hat{p}_j^2}{2m_j} + \frac{1}{2} m_j \omega_j^2 \left(\hat{x}_j - \frac{c_j \sigma_z}{m_j \omega_j^2} \right)^2 \right] \quad (6.9)$$

with bath spectral density

$$J(\omega) = \frac{4\pi\eta g^2 \omega \omega_0^2}{(\omega_0^2 - \omega^2)^2 + (2\pi\eta\omega\omega_0)^2} \quad (6.10)$$

was studied. We consider the parameter set $\eta = 0.014$, $g = 0.18\Omega$, and $\omega_0 = \Omega$ (unless stated otherwise), and set the bath to an initial temperature of $T = 0.1\Omega$.

Following the procedure in Ref. [72], we express the bath autocorrelation function corresponding to the spectral density in Eq. (6.10) using the form of Eqs. (6.6) and (6.7) as

$$\begin{aligned} L_R^{[N_R]}(t) &= \frac{g^2 \omega_0}{2\tilde{\omega}} \left(\coth \left(\frac{\tilde{\omega} + i2\pi\eta\omega_0}{2T} \right) e^{i\tilde{\omega}t} + \coth \left(\frac{\tilde{\omega} - i2\pi\eta\omega_0}{2T} \right) e^{-i\tilde{\omega}t} \right) e^{-\pi\eta\Omega t} \\ &\quad - \sum_{k=1}^{N_R} \frac{\alpha\pi\omega_0^2 \epsilon_k T}{\left((\tilde{\omega} + i\pi\eta\omega_0)^2 + \epsilon_k^2 \right) \left((\tilde{\omega} - i\pi\eta\omega_0)^2 + \epsilon_k^2 \right)} e^{-\epsilon_k t} \end{aligned} \quad (6.11)$$

$$L_I(t) = \frac{g^2 \omega_0}{2\tilde{\omega}} i \left(e^{i\tilde{\omega}t} - e^{-i\tilde{\omega}t} \right) e^{-\pi\eta\omega_0 t}, \quad (6.12)$$

with the shorthand notation

$$\tilde{\omega} = \omega_0 \sqrt{1 - (\pi\eta)^2}, \quad (6.13)$$

$$\epsilon_k = 2\pi k T. \quad (6.14)$$

Note that the decomposition of the imaginary part in Eq. (6.12) is exact with only two terms, while the real part in Eq. (6.11) is only exact in the limit $N_R \rightarrow \infty$. However, as shown in Fig. 6.1, convergence is rapid, and even using $N_R = 0$ yields percent-level accuracy.

Using Eq. (6.8), we compute the polarization dynamics $P(t) = \langle \hat{\sigma}_z \rangle (t) = \text{Tr} \left(\rho^{(0,\dots,0)}(t) \hat{\sigma}_z \right)$ for different values of N_R and N_C , as depicted in Fig. 6.2(a). As expected from Fig. 6.1, changing N_R barely changes the dynamics, while a hierarchy depth of at least $N_C = 3$ is required for complete convergence.

In the case $\eta = 0$, the model defined in Eqs. (6.9) and (6.10) is equivalent to [47]

$$\hat{H} = \frac{\Omega}{2} \hat{\sigma}_x - g \hat{\sigma}_z \left(\hat{a} + \hat{a}^\dagger \right) + \omega_0 \hat{a}^\dagger \hat{a}, \quad (6.15)$$

which we have encountered before in section 3.3. Since the harmonic mode is initialized

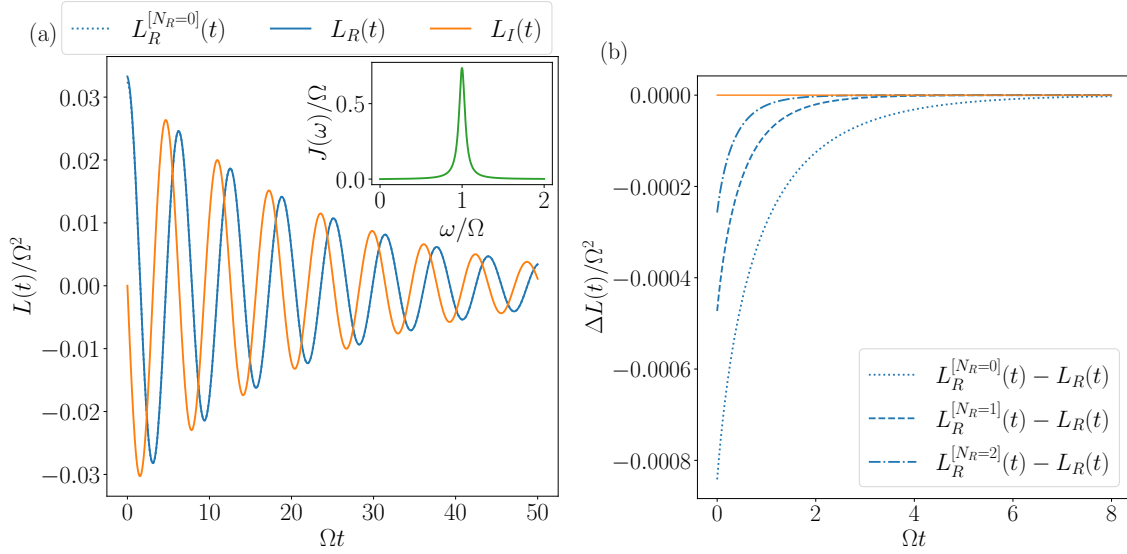


Figure 6.1: (a) Real part $L_R(t)$ and imaginary part $L_I(t)$ of the bath autocorrelation function according and approximation of the real part $L_R^{[N_R]}(t)$ for $N_R = 0$. The difference between $L_R(t)$ (solid blue line) and $L_R^{[N_R=0]}(t)$ (dotted blue line) is small and therefore barely visible. Inset: Bath spectral density Eq. (6.10). (b) Difference between the approximation $L_R^{[N_R]}(t)$ and the exact $L_R(t)$ for different values of N_R as indicated.

at a finite-temperature thermal state, we solve the dynamics here by directly integrating the von-Neumann equation (as opposed to the Schrödinger equation in section 3.3). The parameter η corresponds to the coupling strength between the harmonic mode and an Ohmic bath, resulting in an effective broadening of the mode and thus η is related to the width of the peaked spectral density given in Eq. (6.10) [30, 47]. In Fig. 6.2(b), we further validate our HEOM results by showing that it can interpolate between the undamped dynamics and the dynamics for $\eta = 0.014$ by varying η .

In Fig. 6.3, we compare the polarization dynamics obtained by HEOM and TEMPO to data of Ref. [47], where the iterative QUAPI method (as presented in section 2.7) was used. As expected, we observe a near-perfect match between the HEOM and TEMPO results as both are numerically exact methods that have been fully converged. However, the converged TEMPO simulation employing $\Omega\Delta t = 0.25$ and $\lambda_c = 10^{-5.5}$ is much more computationally demanding than the HEOM simulation, taking about 15 minutes for TEMPO compared to less than a second for HEOM. Furthermore, there is a significant deviation from the iterative QUAPI results, which can be attributed to a combination of the three approximations made in Ref. [47]. In that work, the i-QUAPI data was generated by equivalently considering the harmonic mode as part of the system damped by an Ohmic bath. The computational effort of QUAPI scales rapidly with system size, so the oscillator was restricted to the 12 lowest eigenstates. Additionally, a memory cutoff of $k_{\max} = 1$ was used, and a cutoff frequency of $\omega_c = 10\Omega$ was introduced into the Ohmic bath.

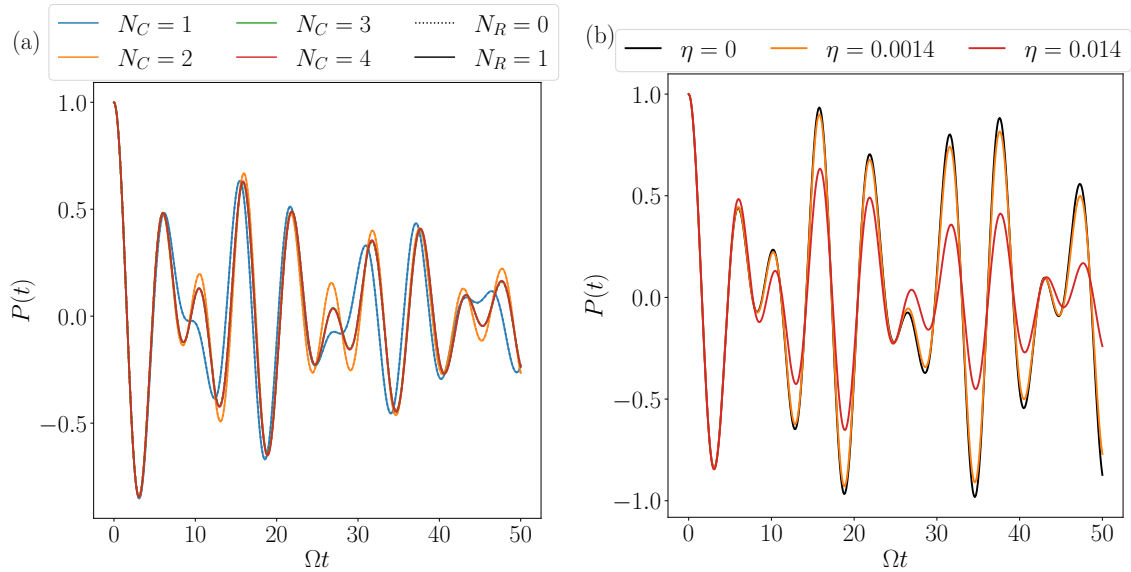


Figure 6.2: (a) HEOM Polarization dynamics for different values of N_C and N_R . (b) Polarization dynamics for the undamped case ($\eta = 0$) generated by directly integrating the von-Neumann equation and HEOM polarization dynamics for the damped case ($\eta > 0$).

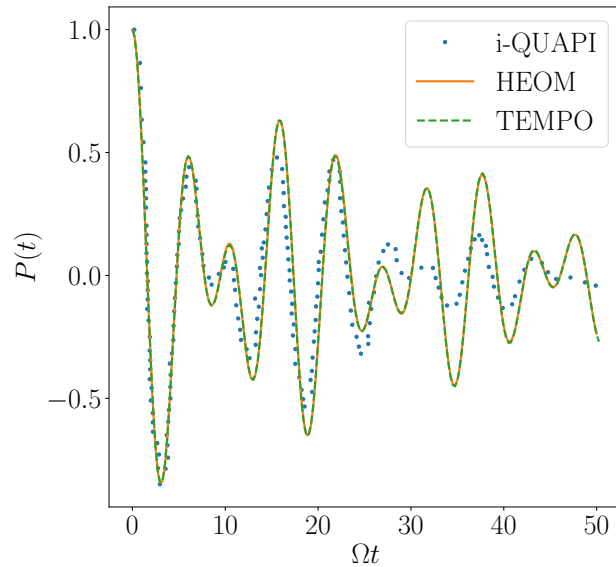


Figure 6.3: Polarization dynamics for $\eta = 0.014$ computed using HEOM (orange solid line), TEMPO (green dashed line), and iterative QUAPI (blue dots). In the latter case, the data has been taken from Ref. [47].

In conclusion, HEOM is better suited for the model that will be treated in the next section due to its rapid convergence for spectral densities of the form given in Eq. (6.10), and its straightforward generalization to multiple baths, unlike TEMPO (see also section 3.4).

6.2 Model

Similar to Refs. [31, 73], we consider the Hamiltonian

$$\hat{H} = \hat{H}_{\text{el}} + \hat{H}_{\text{el-nuc}} + \hat{H}_{\text{nuc}} + \hat{H}_{\text{env}}, \quad (6.16)$$

where

$$\hat{H}_{\text{el}} = \frac{\epsilon}{2} \hat{\sigma}_z + \frac{\Delta}{2} \hat{\sigma}_x \quad (6.17)$$

describes two molecular electronic states with energy splitting ϵ and tunneling splitting Δ . Additionally, the system consists of nuclear modes with the Hamiltonian

$$\hat{H}_{\text{nuc}} = \sum_{i \in \{c,t\}} \Omega (\hat{P}_i^2 + \hat{Q}_i^2) / 2. \quad (6.18)$$

Here, $\hat{Q}_i^2 = \Omega m_i \hat{q}_i$ and $\hat{P}_i^2 := \hat{p}_i^2 / (\Omega m_i)$ denote the unitless position and momentum operators of the tuning (t) and coupling (c) modes, where both modes have identical vibrational frequencies Ω . The electronic states are bilinearly coupled to the nuclear modes via

$$\hat{H}_{\text{el-nuc}} = \kappa_c \hat{\sigma}_x \hat{Q}_c + \kappa_t \hat{\sigma}_z \hat{Q}_t \quad (6.19)$$

with vibronic coupling strengths $\kappa_{c/t}$. We employ realistic model parameters similar to those found in photosynthetic complexes [31, 73]: $\epsilon = \Omega = 300 \text{ cm}^{-1}$, $\Delta = 50 \text{ cm}^{-1}$, $\kappa_t = 150 \text{ cm}^{-1}$, and $\kappa_c = 75 \text{ cm}^{-1}$. The *potential energy surfaces* are defined as the eigenenergies $E_{\pm}(Q_c, Q_t)$ of the Hamiltonian $\hat{H}_{\text{el}} + \hat{H}_{\text{el-nuc}}(Q_c, Q_t) + \hat{H}_{\text{nuc}}(Q_c, Q_t)$, where the nuclear mode positions Q_c and Q_t are treated as parameters, and the nuclear momenta are set to zero. Therefore, the potential energy surfaces $E_{\pm}(Q_c, Q_t)$ are given by the eigenvalues of the matrix

$$\begin{pmatrix} \epsilon/2 + \kappa_t Q_t + \Omega_c Q_c^2/2 + \Omega_t Q_t^2/2 & \Delta/2 + \kappa_c Q_c \\ \Delta/2 + \kappa_c Q_c & -\epsilon/2 - \kappa_t Q_t + \Omega_c Q_c^2/2 + \Omega_t Q_t^2/2 \end{pmatrix}, \quad (6.20)$$

which are

$$E_{\pm}(Q_c, Q_t) = \Omega_c Q_c^2/2 + \Omega_t Q_t^2/2 \pm \sqrt{(\epsilon/2 + \kappa_t Q_t)^2 + (\Delta/2 + \kappa_c Q_c)^2}. \quad (6.21)$$

The potential energy surfaces exhibit a conical intersection at $Q_t = -\epsilon/(2\kappa_t) = -1$ and $Q_c = -\Delta/(2\kappa_c) = -1/3$, as shown in Fig. 6.4. The electronic two-level system is initially prepared in the excited electronic state, and the nuclear modes are initialized at thermal equilibrium at room temperature ($293 \text{ K} \sim 204 \text{ cm}^{-1}$), where it is assumed that they are initially decoupled from the electronic degree of freedom. The initial probability density in position space of the nuclear modes on the upper electronic potential surface,

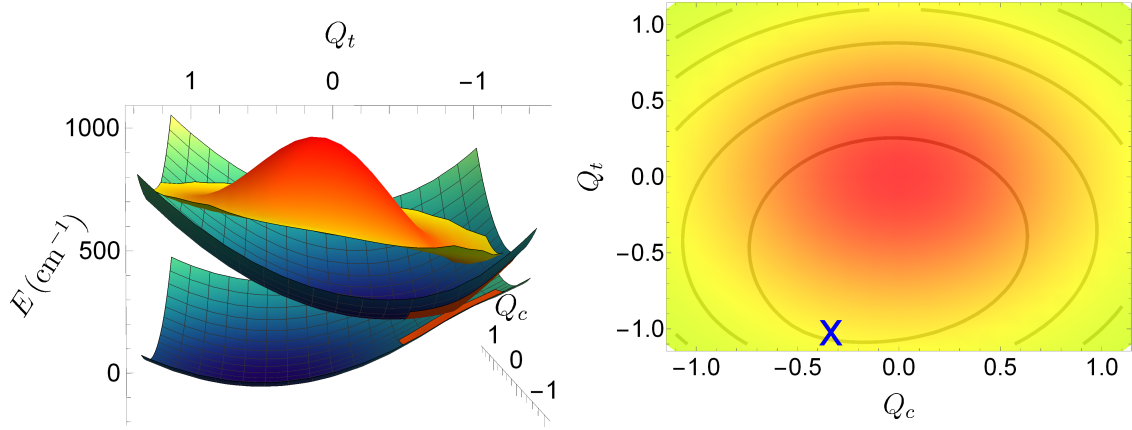


Figure 6.4: Left: Potential energy surfaces of $\hat{H}_{\text{el}} + \hat{H}_{\text{el-nuc}} + \hat{H}_{\text{nuc}}$ and probability density of the initial state based on the parameters provided in the text. The region around the conical intersections is highlighted in orange. Right: The potential energy surface is depicted with contour lines, and the initial state's probability density is color-coded. The conical intersection is highlighted by a blue cross.

graphically depicted in Fig. 6.4, is given by

$$|\psi_e(Q_c, Q_t)|^2 := |\langle Q_c, e | \text{Tr}_t(W(0)) | Q_c, e \rangle \cdot \langle Q_t, e | \text{Tr}_c(W(0)) | Q_t, e \rangle|^2, \quad (6.22)$$

where $W(0)$ denotes the initial density matrix, $|e/g\rangle$ denotes the electronic excited/-ground state, $|Q_{c/t}\rangle$ denotes a position eigenstate of the coupling/tuning mode, and $\text{Tr}_{c/t}$ denotes the trace over all states of the coupling/tuning mode.

The environmental effects are described by three sets of harmonic oscillators

$$\hat{H}_{\text{env}} = \sum_{i \in \{c,t,\text{el}\}} \sum_j \left[\frac{\hat{p}_{ij}^2}{2m_{ij}} + \frac{1}{2} m_{ij} \omega_{ij}^2 \left(\hat{x}_{ij} - \frac{c_{ij} \hat{s}_i}{m_{ij} \omega_{ij}^2} \right)^2 \right]. \quad (6.23)$$

The vibrational damping of the tuning and coupling modes and electronic dephasing take place via the operators $\hat{s}_c = \hat{Q}_c$, $\hat{s}_t = \hat{Q}_t$, and $\hat{s}_{\text{el}} = \hat{\sigma}_z$, respectively. For the vibrational damping, we assume pure Ohmic spectral densities with equal damping constants η_{vib} such that

$$J_{c,t}(\omega) = \eta_{\text{vib}} \omega. \quad (6.24)$$

For the electronic bath, we also assume an Ohmic form

$$J_{\text{el}}(\omega) = \eta_{\text{el}} \omega \gamma^2 / (\gamma^2 + \omega^2) \quad (6.25)$$

with the electronic damping constant η_{el} . Following spectroscopic measurements of photosynthetic complexes in aqueous solution [74, 75], the electronic damping constant will be chosen to be an order of magnitude larger than the vibrational damping constant and

the Drude cutoff frequency is fixed to $\gamma = 4\epsilon$. The environmental harmonic degrees of freedom are initialized at thermal equilibrium at room temperature.

6.2.1 Mapping to an Effective Spin-Boson Model

To obtain the electronic dynamics, we map the Hamiltonian in Eq. (6.16) to an effective spin-boson model. This procedure was originally introduced in Ref. [30] and has subsequently been used in Refs. [31, 73] in a setting very similar to our current setup. Both the nuclear tuning and coupling modes become part of the bath, resulting in the Hamiltonian

$$\hat{H} = \hat{H}_{\text{el}} + \hat{H}_{\text{env}}^{\text{eff}}, \quad (6.26)$$

where $\hat{H}_{\text{env}}^{\text{eff}}$ is formally identical to Eq. (6.23), but with $\hat{s}_c = \hat{\sigma}_x$ and $\hat{s}_t = \hat{\sigma}_z$, and with the effective spectral densities

$$J_{c/t}^{\text{eff}}(\omega) = \frac{16\eta_{\text{vib}}k_{c/t}^2\omega\Omega^2}{(\Omega^2 - \omega^2)^2 + (2\pi\eta_{\text{vib}}\omega\Omega)^2}. \quad (6.27)$$

Instead of directly coupling the electronic two-level system to the two nuclear modes, which are then subject to Ohmic vibrational damping, we couple it to effective baths with spectral densities that have peaks at the nuclear mode frequency Ω and widths determined by η_{vib} . For the initial preparation used here, this mapping is exact. As the structured environment coupled to the electronic system induces non-Markovian dynamics, we use the HEOM technique to obtain the reduced density matrix of the electronic system. The electronic dynamics is shown in Fig. 6.5 for both the undamped case $\eta_{\text{el}} = 0 = \eta_{\text{vib}}$ and the damped case $\eta_{\text{el}} = 0.1$ and $\eta_{\text{vib}} = 0.01$. The undamped case corresponds to the Hamiltonian

$$\hat{H} = \hat{H}_{\text{el}} + \hat{H}_{\text{el-nuc}} + \hat{H}_{\text{nuc}}, \quad (6.28)$$

where the dynamics was obtained by numerical integration of the von-Neumann equation. For the damped case Eq. (6.26), HEOM was used. The coupling strengths in this case were chosen to be similar to what has been observed in photosynthetic complexes, where electronic damping occurs on a much faster timescale than vibrational damping [74–77].

6.3 Dissipative Transient Redistribution of Ultrafast Electronic Coherences in Attosecond Raman Signals

The transient redistribution of ultrafast electronic coherences in attosecond Raman signals (TRUECARS) [39] technique uses a combination of a broadband pulse $\mathcal{E}_0(t)$ and a

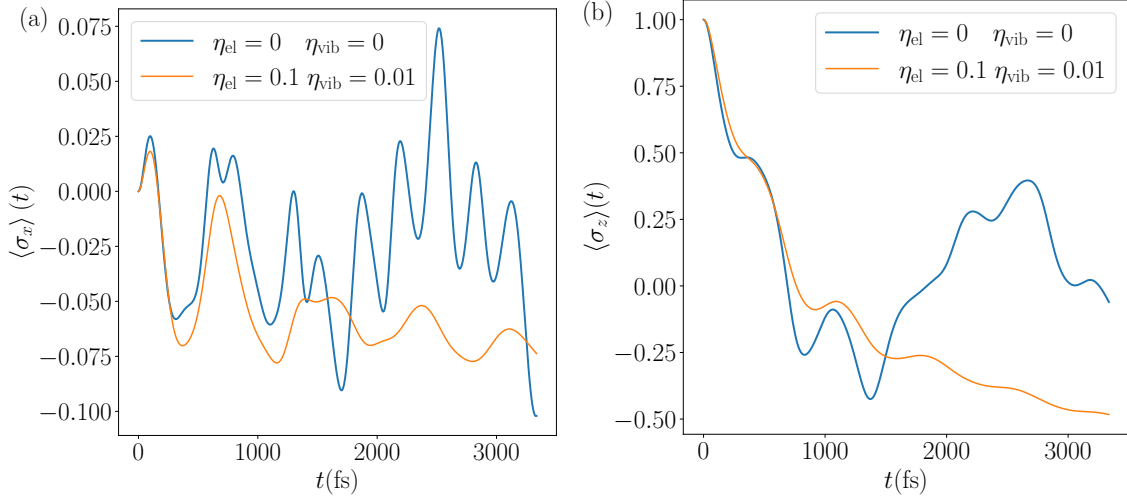


Figure 6.5: Electronic dynamics for undamped (blue lines) and damped case (orange lines). (a) Coherence dynamics $\langle \hat{\sigma}_x \rangle(t)$. (b) Population dynamics $\langle \hat{\sigma}_z \rangle(t)$.

narrow-band pulse $\mathcal{E}_1(t)$ as a probing field, with

$$H_{\text{spec}}(t) = \hat{\sigma}_x |\mathcal{E}_0(t) + \mathcal{E}_1(t)|^2, \quad (6.29)$$

and Gaussian field envelopes

$$\mathcal{E}_{0/1}(t) = \frac{1}{\sigma_{0/1}} \exp\left(-\frac{t^2}{2\sigma_{0/1}^2}\right), \quad (6.30)$$

where we set the pulse durations to $\sigma_0 = 7.5$ fs and $\sigma_1 = 30$ fs. The TRUECARs signal is given by

$$S(\omega, T) = 2\Im \int_{-\infty}^{\infty} dt e^{i\omega(t-T)} \mathcal{E}_0^*(\omega) \mathcal{E}_1(t-T) \langle \sigma_x(t) \rangle, \quad (6.31)$$

with Raman frequency ω and delay time T . Due to Eq. (6.31), σ_0 is connected to the width of an envelope function on the TRUECARs signal with respect to ω . Thus, the only requirement on σ_0 is that it needs to be sufficiently small, i.e., it needs to supply sufficient temporal resolution for the TRUECARs signal to still be visible (see Fig. 6.6). The requirements on σ_1 are that it has to be significantly shorter than the timescale on which the dynamics takes place and yet spectrally narrower than the electronic energy splitting [39], which corresponds to $\sigma_1 \gtrsim 17.5$ fs in the model considered here. The signals $S(\omega, T)$ of the undamped and damped cases are shown in Fig. 6.6 (a) and (b), respectively. The red and blue signals show the Stokes and the anti-Stokes components of the Raman spectra. The oscillatory pattern for later delay times T indicates that the electronic coherence lifetime is longer than the simulation time and exceeds 2 ps in the absence of dissipation. The oscillatory pattern in the undamped case becomes more complex at later delay times, since after the first passage of the conical intersection, the electronic wavepacket returns and repasses through the intersection, thereby generating new electronic coherences on

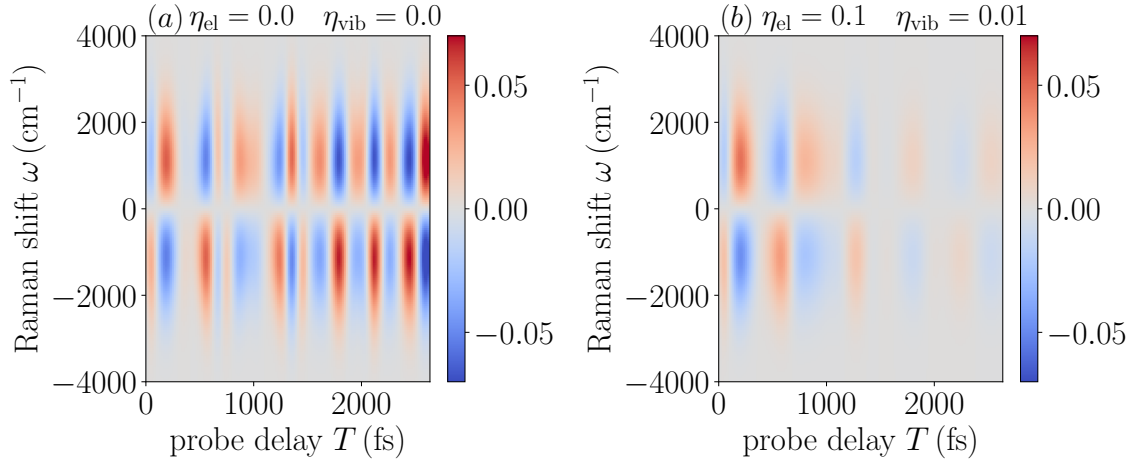


Figure 6.6: TRUECARs Signal $S(\omega, T)$, Eq. (6.31) corresponding to the coherence dynamics in Fig. 6.5, for (a) the undamped case $\eta_{\text{el}} = 0 = \eta_{\text{vib}}$, and (b) the damped case $\eta_{\text{el}} = 0.1, \eta_{\text{vib}} = 0.01$.

a time scale determined by the vibrational frequency.

In the presence of dissipation, the oscillatory pattern fades out on a time scale of a few hundred femtoseconds. Yet, we speculate that such a signal should still be measurable in a present-day experimental set-ups.

To quantify the influence of the damping strength on the electronic coherence, we consider the ratio of the TRUECARs signal strength with and without damping for fixed delay times. In Fig. 6.7, we show the ratio $S_{\eta_{\text{el}}, \eta_{\text{vib}}} / S_{0,0}$, where we take the local maxima at the waiting times closest to the two different values $T = 200$ fs (solid lines) and $T = 2200$ fs (dash-dotted lines). At short delay times $T = 200$ fs, the TRUECARs sig-

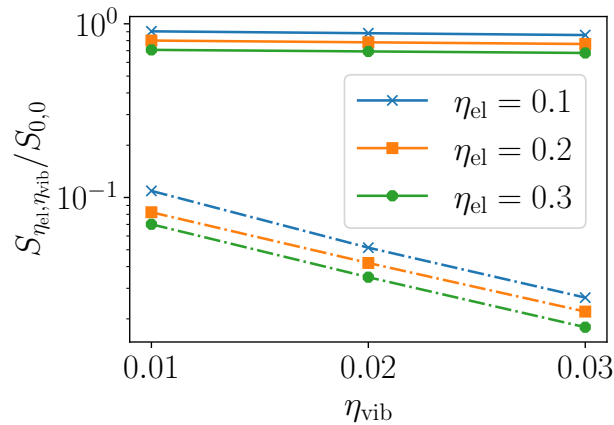


Figure 6.7: Ratio of the magnitudes of the local maxima of the damped TRUECARs signals $S_{\eta_{\text{el}}, \eta_{\text{vib}}}(\omega = 970 \text{ cm}^{-1}, T)$ and the corresponding undamped signal $S_{0,0}(\omega = 970 \text{ cm}^{-1}, T)$ for all $(\eta_{\text{el}}, \eta_{\text{vib}}) \in \{0.1, 0.2, 0.3\} \times \{0.01, 0.02, 0.03\}$. The solid lines represent the local maxima closest to $T = 200$ fs, while the dash-dotted lines indicate the maxima closest to $T = 2200$ fs.

nal is still sizable even for rather strong electronic damping. At these short times, the

weaker vibrational damping has essentially no effect. The vibrational damping sets in at longer waiting times, as seen from the data for $T = 2200$ fs, where it causes the signal to be an order of magnitude weaker. Nevertheless, the characteristic signal is still present, showing that TRUECARS is a versatile tool to uncover time-dependent electronic coherences in the dynamics of an electronic wavepacket near a conical intersection, even in the presence of electronic and vibrational damping.

6.3.1 Frequency-Resolved Optical Gating (FROG) Spectrogram

The fate of the coherences near the conical intersection may also be revealed by the frequency-resolved optical gating (FROG) spectrogram [78]

$$I(\omega, T) = \left| \int_{-\infty}^{\infty} dt S(t) E_{\text{gate}}(t - T) e^{-i\omega t} \right|^2, \quad (6.32)$$

of the TRUECARS signal $S(t) = S(\omega, T = t)$ with the gating function

$$E_{\text{gate}}(t - T) = \theta(t - T)\theta(1000 \text{ fs} - t + T). \quad (6.33)$$

Thus, the FROG signal corresponds to the Fourier transforms of the TRUECARS signal for all possible time windows of length 1000 fs. To identify the energies relevant for electronic transitions, we define the *stick spectrum* by following Ref. [79]. The energy eigenbasis of Eq. (6.28) is denoted as $|k\rangle$ with the eigenenergies E_k , and the product basis consisting of the uncoupled electronic and vibrational states is denoted as $|e/g, n_t, n_c\rangle$. There, $|e/g\rangle$ refers to the electronic excited/ground state and $|n_{c/t}\rangle$ refers to the state with occupation number $n_{c/t}$ of the coupling/tuning mode. The stick height $|\mu_{k,l}|^2$ associated with the transition energy $E_k - E_l$ is then obtained from

$$\mu_{k,l} := \langle k | \hat{\sigma}_x | l \rangle = \sum_{n_t, n_c} [\langle k | g, n_t, n_c \rangle \langle e, n_t, n_c | l \rangle + \langle k | e, n_t, n_c \rangle \langle g, n_t, n_c | l \rangle]. \quad (6.34)$$

In Fig. 6.8, the FROG spectrogram $I(\omega, T)$ of the TRUECARS signal is shown for both the undamped and damped cases. We observe that a strong FROG component develops around 250 cm^{-1} , which corresponds to the fundamental energy gap between the two lowest vibronic states, as indicated by the stick spectrum.

In the absence of damping (see Fig. 6.8 (a)), the signal weakens after about 300 fs, moves to smaller frequencies, and reappears again around 250 cm^{-1} , before eventually disappearing. In the presence of damping (see Fig. 6.8 (b)), the FROG signal emerges at slightly higher frequencies, approximately around 270 cm^{-1} . Although the FROG signal weakens after a delay time of about 300 fs, it is still clearly present.

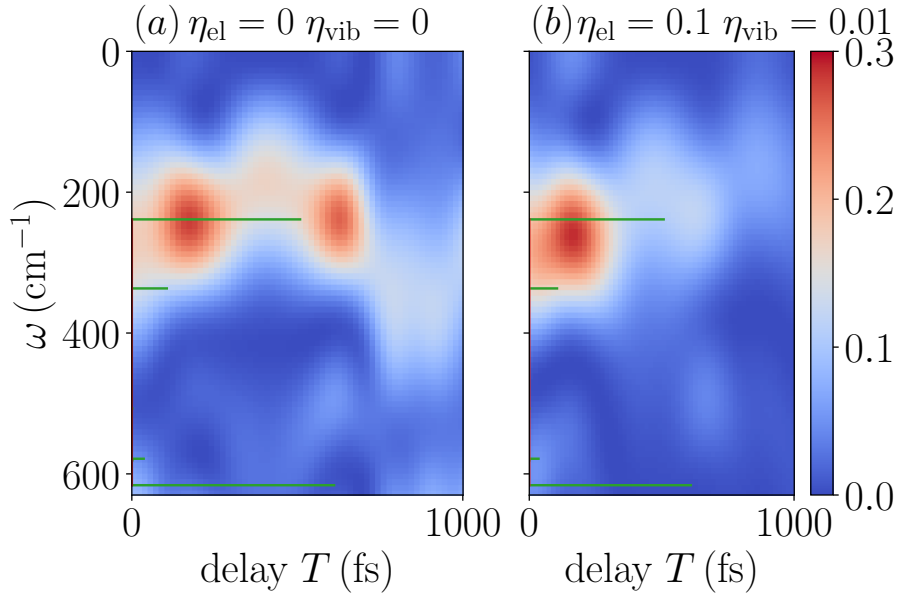


Figure 6.8: FROG Signal $I(\omega, T)$, Eq. (6.32), with $S(t) = S(\omega = 970 \text{ cm}^{-1}, T = t)$ for (a) the undamped case $\eta_{\text{el}} = 0 = \eta_{\text{vib}}$, and (b) the damped case $\eta_{\text{el}} = 0.1$, $\eta_{\text{vib}} = 0.01$. The green bars mark the stick spectrum of the undamped vibronic Hamiltonian.

6.4 Summary

In section 6.1, the HEOM technique was briefly introduced by closely following the literature. Then, the HEOM implementation was validated by comparing the dynamics of a single-mode model to HEOM results for a corresponding effective spin-boson model with a peaked spectral density. Furthermore, it was shown that HEOM results on the latter model very closely match the corresponding TEMPO results and that HEOM is more efficient on this model by orders of magnitude. Also, it was shown that iterative QUAPI results from the literature deviate significantly from the exact result on the same model due to additional approximations made there. In section 6.2, the molecular vibronic dynamics in the presence of dissipation was modeled in terms of a two-state two-mode model with realistic parameters, resembling experimental observations of photosynthetic complexes at room temperature known in the literature. This model was then exactly mapped to an effective spin-boson model with two non-commuting baths with a peaked spectral density. In section 6.3, the effect of environmental dissipation on the TRUECARs signal strength was studied in this model. It was found that on the scale of 100 fs, it barely gets weakened, and on the scale of 1000 fs, it gets weakened by about an order of magnitude.

7 Conclusion and Outlook

In chapter 2, a detailed derivation of the quasi adiabatic propagator path integral (QUAPI) Makri and Makarov [8, 9] has been provided. Additionally, a minor (but novel) improvement of the original iteration scheme has been introduced. However, this improvement is less relevant due to other recent advances, such as the small matrix decomposition of the path integral expression (SMatPI) [50] and its extension [51]. These advancements make the computational effort for propagation after a memory cutoff negligible and have been presented here in a simplified version employing the Trotter splitting used by Strathearn et al. [45]. Additionally, the approximation introduced by SMatPI has been systematically analyzed, and an argument has been made that it serves as a complete replacement of the original iteration scheme.

In chapter 3, a concise introduction to the tensor network formalism has been provided. The time-evolving matrix product operator (TEMPO) technique by Strathearn et al. [11], which evaluates QUAPI in terms of the contraction of a tensor network, has been derived in a much simpler fashion compared to the original presentation. Subsequently, TEMPO has been benchmarked on a single-mode model consisting of a two-level system coupled to a single harmonic oscillator. Although this model is trivial to solve in general, it poses a formidable challenge for the TEMPO method due to the oscillator turning the dynamics of the two-level system highly non-local. Nonetheless, it has been shown that TEMPO is applicable to the single-mode model. Additionally, the surprising property that the computational cost of TEMPO scales only quadratically with the inverse time discretization step has been uncovered. Furthermore, the TEMPO approach has been generalized to the case of two baths acting on the central system with coupling operators that do not commute with each other. This novel method essentially rephrases the method of Palm et al. [62], where QUAPI was generalized to multiple baths, in terms of the contraction of a tensor network. Thereby, the computational efficiency is increased substantially, reducing the computation time from days to seconds in a specific case. Subsequently, the method has been used to demonstrate how a second bath disrupts the quantum Zeno effect in the Ohmic spin-boson model at zero temperature. A further direction of study could be a more detailed analysis of the dephasing rates in this case.

In chapter 4, by utilizing TEMPO, a novel dynamical phase of the spin-boson model at zero temperature has been discovered at strong coupling strength. It has been shown that no coherent dynamics occurs at strong coupling strength. This *pseudo-coherent* dynamics

is characterized by a single oscillatory minimum in the polarization dynamics and is induced entirely by the bath. Subsequently, a dynamical phase diagram at zero temperature for the spin-boson model in the (sub-)Ohmic regime has been obtained. Based on this, the phase diagram has been extended to the super-Ohmic regime in Ref. [26]. A further direction of study could be investigating the critical coupling strengths of the localization transition for the full parameter space. This may be achieved by the TEMPO contraction strategy recently developed in Ref. [80], which makes propagation to infinite times feasible. Another direction could be studying the effect of the bath high-frequency cutoff. However, these topics were beyond the scope of this work.

In chapter 5, the phase diagram of the spin-boson model has been extended to the $1/f$ quantum noise regime. Furthermore, the dephasing rate at weak coupling strengths in the (sub-)Ohmic and the $1/f$ regime, and its dependence on both temperature and an infrared bath frequency cutoff, has been studied. An empirical formula for the dephasing rate has been given, which is valid at zero temperature in the full parameter space and valid at finite temperature for most of the parameter space studied. Potentially, this work may provide designing guidelines for the optimization of superconducting qubits.

In the final chapter 6, the hierarchical equations of motion (HEOM) method of Tanimura and Kubo [12] has been summarized, and its numerical results have been verified by comparing to TEMPO on a single-mode model where the oscillator mode is subject to Ohmic damping. The reason HEOM has been chosen over TEMPO is its straightforward generalization to multiple baths and superior efficiency for the specific spectral densities that were considered. The transient redistribution of ultrafast electronic coherences in attosecond Raman signals (TRUECARs) [39], which is a spectroscopic technique for measuring conical intersections, has subsequently been studied using HEOM. By employing a toy model with parameters motivated by experimental measurements from photosynthetic complexes, the effect of environmental dissipation at room temperature on the TRUECARs signal strength has been studied. It has been concluded that TRUECARs should be sufficiently robust to be measurable in a future spectroscopic experiment.

Bibliography

- [1] R. Santra, *Einführung in die Theoretische Physik: Klassische Mechanik mit mathematischen Methoden*. Berlin, Heidelberg: Springer Berlin Heidelberg, 2023.
 - [2] A. J. Leggett, S. Chakravarty, A. T. Dorsey, M. P. A. Fisher, A. Garg, and W. Zwerger, "Dynamics of the dissipative two-state system," *Rev. Mod. Phys.*, vol. 59, pp. 1–85, Jan. 1987.
 - [3] M. A. Nielsen and I. L. Chuang, *Quantum computation and quantum information*. Cambridge ; New York: Cambridge University Press, 10th anniversary ed ed., 2010.
 - [4] A. O. Caldeira and A. J. Leggett, "Influence of Dissipation on Quantum Tunneling in Macroscopic Systems," *Phys. Rev. Lett.*, vol. 46, pp. 211–214, Jan. 1981.
 - [5] A. Redfield, "The Theory of Relaxation Processes," in *Advances in Magnetic and Optical Resonance*, vol. 1, pp. 1–32, Elsevier, 1965.
 - [6] R. Feynman and F. Vernon, "The theory of a general quantum system interacting with a linear dissipative system," *Annals of Physics*, vol. 24, pp. 118–173, Oct. 1963.
 - [7] R. Egger and U. Weiss, "Quantum Monte Carlo simulation of the dynamics of the spin-boson model," *Z. Physik B - Condensed Matter*, vol. 89, pp. 97–107, Feb. 1992.
 - [8] N. Makri and D. E. Makarov, "Tensor propagator for iterative quantum time evolution of reduced density matrices. I. Theory," *The Journal of Chemical Physics*, vol. 102, pp. 4600–4610, Mar. 1995.
 - [9] N. Makri and D. E. Makarov, "Tensor propagator for iterative quantum time evolution of reduced density matrices. II. Numerical methodology," *The Journal of Chemical Physics*, vol. 102, pp. 4611–4618, Mar. 1995.
 - [10] N. Makri, "Small Matrix Path Integral for System-Bath Dynamics," *J. Chem. Theory Comput.*, vol. 16, pp. 4038–4049, July 2020.
 - [11] A. Strathearn, P. Kirton, D. Kilda, J. Keeling, and B. W. Lovett, "Efficient non-Markovian quantum dynamics using time-evolving matrix product operators," *Nat Commun*, vol. 9, p. 3322, Dec. 2018.
 - [12] Y. Tanimura and R. Kubo, "Time Evolution of a Quantum System in Contact with a Nearly Gaussian-Markoffian Noise Bath," *J. Phys. Soc. Jpn.*, vol. 58, pp. 101–114, Jan. 1989.
-

- [13] D. Suess, A. Eisfeld, and W. Strunz, "Hierarchy of Stochastic Pure States for Open Quantum System Dynamics," *Phys. Rev. Lett.*, vol. 113, p. 150403, Oct. 2014.
 - [14] H. Liu, L. Zhu, S. Bai, and Q. Shi, "Reduced quantum dynamics with arbitrary bath spectral densities: Hierarchical equations of motion based on several different bath decomposition schemes," *The Journal of Chemical Physics*, vol. 140, p. 134106, Apr. 2014.
 - [15] C. Duan, Z. Tang, J. Cao, and J. Wu, "Zero-temperature localization in a sub-Ohmic spin-boson model investigated by an extended hierarchy equation of motion," *Phys. Rev. B*, vol. 95, p. 214308, June 2017.
 - [16] H.-D. Meyer, U. Manthe, and L. Cederbaum, "The multi-configurational time-dependent Hartree approach," *Chemical Physics Letters*, vol. 165, pp. 73–78, Jan. 1990.
 - [17] H. Wang, "Basis set approach to the quantum dissipative dynamics: Application of the multiconfiguration time-dependent Hartree method to the spin-boson problem," *The Journal of Chemical Physics*, vol. 113, pp. 9948–9956, Dec. 2000.
 - [18] H. Wang and M. Thoss, "Multilayer formulation of the multiconfiguration time-dependent Hartree theory," *The Journal of Chemical Physics*, vol. 119, pp. 1289–1299, July 2003.
 - [19] Y. Kurashige, "Matrix product state formulation of the multiconfiguration time-dependent Hartree theory," *The Journal of Chemical Physics*, vol. 149, p. 194114, Nov. 2018.
 - [20] R. Bulla, N.-H. Tong, and M. Vojta, "Numerical Renormalization Group for Bosonic Systems and Application to the Sub-Ohmic Spin-Boson Model," *Phys. Rev. Lett.*, vol. 91, p. 170601, Oct. 2003.
 - [21] C. Seoanez, F. Guinea, and A. H. C. Neto, "Dissipation due to two-level systems in nano-mechanical devices," *Europhys. Lett.*, vol. 78, p. 60002, June 2007.
 - [22] D. Rosenberg, P. Nalbach, and D. D. Osheroff, "Memory Effects in Amorphous Solids below 20 mK," *Phys. Rev. Lett.*, vol. 90, p. 195501, May 2003.
 - [23] P. Nalbach and M. Thorwart, "Ultraslow quantum dynamics in a sub-Ohmic heat bath," *Phys. Rev. B*, vol. 81, p. 054308, Feb. 2010.
 - [24] D. Kast and J. Ankerhold, "Persistence of Coherent Quantum Dynamics at Strong Dissipation," *Phys. Rev. Lett.*, vol. 110, p. 010402, Jan. 2013.
 - [25] F. Otterpohl, P. Nalbach, and M. Thorwart, "Hidden Phase of the Spin-Boson Model," *Phys. Rev. Lett.*, vol. 129, p. 120406, Sept. 2022.
-

-
- [26] P. Nacke, F. Otterpohl, M. Thorwart, and P. Nalbach, "Dephasing and pseudocoherent quantum dynamics in super-Ohmic environments," *Phys. Rev. A*, vol. 107, p. 062218, June 2023.
- [27] D. A. Rower, L. Ateshian, L. H. Li, M. Hays, D. Bluvstein, L. Ding, B. Kannan, A. Almanakly, J. Braumüller, D. K. Kim, A. Melville, B. M. Niedzielski, M. E. Schwartz, J. L. Yoder, T. P. Orlando, J. I.-J. Wang, S. Gustavsson, J. A. Grover, K. Serniak, R. Comin, and W. D. Oliver, "Evolution of $1/f$ Flux Noise in Superconducting Qubits with Weak Magnetic Fields," *Phys. Rev. Lett.*, vol. 130, p. 220602, May 2023.
- [28] M. Abdi and M. B. Plenio, "Analog quantum simulation of extremely sub-Ohmic spin-boson models," *Phys. Rev. A*, vol. 98, p. 040303, Oct. 2018.
- [29] T. Palm, *The two level system under the influence of non-commuting fluctuations*. PhD thesis, Hamburg, 2020.
- [30] A. Garg, J. N. Onuchic, and V. Ambegaokar, "Effect of friction on electron transfer in biomolecules," *The Journal of Chemical Physics*, vol. 83, pp. 4491–4503, Nov. 1985.
- [31] H.-G. Duan, R. J. D. Miller, and M. Thorwart, "Impact of Vibrational Coherence on the Quantum Yield at a Conical Intersection," *J. Phys. Chem. Lett.*, vol. 7, pp. 3491–3496, Sept. 2016.
- [32] D. R. Yarkony, "Diabolical conical intersections," *Rev. Mod. Phys.*, vol. 68, pp. 985–1013, Oct. 1996.
- [33] W. Domcke, D. Yarkony, and H. Köppel, eds., *Conical intersections Vol. 15: electronic structure, dynamics & spectroscopy*. No. v.15 in Advanced series in physical chemistry, River Edge, NJ: World Scientific, 2004. OCLC: ocm56885304.
- [34] W. Domcke, D. Yarkony, and H. Köppel, *Conical intersections Vol. 17: theory, computation and experiment*. Singapore: World Scientific Publishing Co. Pte. Ltd., 2012. OCLC: 841845209.
- [35] W. Domcke and D. R. Yarkony, "Role of Conical Intersections in Molecular Spectroscopy and Photoinduced Chemical Dynamics," *Annu. Rev. Phys. Chem.*, vol. 63, pp. 325–352, May 2012.
- [36] D. Keefer, S. M. Cavaletto, J. R. Rouxel, M. Garavelli, H. Yong, and S. Mukamel, "Ultrafast X-Ray Probes of Elementary Molecular Events," *Annu. Rev. Phys. Chem.*, vol. 74, pp. 73–97, Apr. 2023.
- [37] D. Polli, P. Altoè, O. Weingart, K. M. Spillane, C. Manzoni, D. Brida, G. Tomasello, G. Orlandi, P. Kukura, R. A. Mathies, M. Garavelli, and G. Cerullo, "Conical intersection dynamics of the primary photoisomerization event in vision," *Nature*, vol. 467, pp. 440–443, Sept. 2010.
-

- [38] M. H. Farag, T. L. C. Jansen, and J. Knoester, "Probing the Interstate Coupling near a Conical Intersection by Optical Spectroscopy," *J. Phys. Chem. Lett.*, vol. 7, pp. 3328–3334, Sept. 2016.
- [39] M. Kowalewski, K. Bennett, K. E. Dorfman, and S. Mukamel, "Catching Conical Intersections in the Act: Monitoring Transient Electronic Coherences by Attosecond Stimulated X-Ray Raman Signals," *Phys. Rev. Lett.*, vol. 115, p. 193003, Nov. 2015.
- [40] D. Keefer, T. Schnappinger, R. De Vivie-Riedle, and S. Mukamel, "Visualizing conical intersection passages via vibronic coherence maps generated by stimulated ultrafast X-ray Raman signals," *Proc. Natl. Acad. Sci. U.S.A.*, vol. 117, pp. 24069–24075, Sept. 2020.
- [41] D. Keefer, V. M. Freixas, H. Song, S. Tretiak, S. Fernandez-Alberti, and S. Mukamel, "Monitoring molecular vibronic coherences in a bichromophoric molecule by ultrafast X-ray spectroscopy," *Chem. Sci.*, vol. 12, no. 14, pp. 5286–5294, 2021.
- [42] S. M. Cavaletto, D. Keefer, and S. Mukamel, "High Temporal and Spectral Resolution of Stimulated X-Ray Raman Signals with Stochastic Free-Electron-Laser Pulses," *Phys. Rev. X*, vol. 11, p. 011029, Feb. 2021.
- [43] G.-L. Ingold, "Path Integrals and Their Application to Dissipative Quantum Systems," *arXiv:quant-ph/0208026*, vol. 611, pp. 1–53, 2002. arXiv: quant-ph/0208026.
- [44] N. Makri, "Blip decomposition of the path integral: Exponential acceleration of real-time calculations on quantum dissipative systems," *The Journal of Chemical Physics*, vol. 141, p. 134117, Oct. 2014.
- [45] A. Strathearn, *Modelling Non-Markovian Quantum Systems Using Tensor Networks*. Springer Theses, Cham: Springer International Publishing, 2020.
- [46] M. Thorwart and P. Hänggi, "Decoherence and dissipation during a quantum XOR gate operation," *Phys. Rev. A*, vol. 65, p. 012309, Dec. 2001.
- [47] M. Thorwart, E. Paladino, and M. Grifoni, "Dynamics of the spin-boson model with a structured environment," *Chemical Physics*, vol. 296, pp. 333–344, Jan. 2004.
- [48] P. Nalbach and M. Thorwart, "Landau-Zener Transitions in a Dissipative Environment: Numerically Exact Results," *Phys. Rev. Lett.*, vol. 103, p. 220401, Nov. 2009.
- [49] P. Nalbach, D. Braun, and M. Thorwart, "Exciton transfer dynamics and quantumness of energy transfer in the Fenna-Matthews-Olson complex," *Phys. Rev. E*, vol. 84, no. 4, p. 041926, 2011.
- [50] N. Makri, "Small matrix disentanglement of the path integral: Overcoming the exponential tensor scaling with memory length," *J. Chem. Phys.*, vol. 152, p. 041104, Jan. 2020.
-

-
- [51] N. Makri, "Small Matrix Path Integral with Extended Memory," *J. Chem. Theory Comput.*, vol. 17, pp. 1–6, Jan. 2021.
- [52] F. Otterpohl, "Advanced Iterative Path Integral Simulation of Nonequilibrium Quantum Dynamics," *Master Thesis, Universität Hamburg*, 2021.
- [53] H. Grabert, P. Schramm, and G.-L. Ingold, "Quantum Brownian motion: The functional integral approach," *Physics Reports*, vol. 168, pp. 115–207, Oct. 1988.
- [54] F. W. Byron and R. W. Fuller, *Mathematics of classical and quantum physics*. 2. Reading, Mass: Addison-Wesley, 1970.
- [55] U. Weiss, *Quantum Dissipative Systems*. World Scientific, 4 ed., Mar. 2012.
- [56] S. R. White, "Density matrix formulation for quantum renormalization groups," *Phys. Rev. Lett.*, vol. 69, pp. 2863–2866, Nov. 1992.
- [57] S. R. White, "Density-matrix algorithms for quantum renormalization groups," *Phys. Rev. B*, vol. 48, pp. 10345–10356, Oct. 1993.
- [58] J. Eisert, M. Cramer, and M. B. Plenio, "Colloquium : Area laws for the entanglement entropy," *Rev. Mod. Phys.*, vol. 82, pp. 277–306, Feb. 2010.
- [59] J. C. Bridgeman and C. T. Chubb, "Hand-waving and Interpretive Dance: An Introductory Course on Tensor Networks," *J. Phys. A: Math. Theor.*, vol. 50, p. 223001, June 2017. arXiv:1603.03039 [cond-mat, physics:hep-th, physics:quant-ph].
- [60] M. Fishman, S. White, and E. Stoudenmire, "The ITensor Software Library for Tensor Network Calculations," *SciPost Phys. Codebases*, p. 4, Aug. 2022.
- [61] M. R. Jørgensen and F. A. Pollock, "Exploiting the causal tensor network structure of quantum processes to efficiently simulate non-Markovian path integrals," *Phys. Rev. Lett.*, vol. 123, p. 240602, Dec. 2019. arXiv: 1902.00315.
- [62] T. Palm and P. Nalbach, "Quasi-adiabatic path integral approach for quantum systems under the influence of multiple non-commuting fluctuations," *J. Chem. Phys.*, vol. 149, p. 214103, Dec. 2018.
- [63] B. Misra and E. C. G. Sudarshan, "The Zeno's paradox in quantum theory," *Journal of Mathematical Physics*, vol. 18, pp. 756–763, Apr. 1977.
- [64] A. H. Castro Neto, E. Novais, L. Borda, G. Zaránd, and I. Affleck, "Quantum Magnetic Impurities in Magnetically Ordered Systems," *Phys. Rev. Lett.*, vol. 91, p. 096401, Aug. 2003.
- [65] E. Novais, A. H. Castro Neto, L. Borda, I. Affleck, and G. Zarand, "Frustration of decoherence in open quantum systems," *Phys. Rev. B*, vol. 72, p. 014417, July 2005.
-

- [66] Z. Lü and H. Zheng, "Quantum dynamics of the dissipative two-state system coupled with a sub-Ohmic bath," *Phys. Rev. B*, vol. 75, p. 054302, Feb. 2007.
- [67] A. Winter, H. Rieger, M. Vojta, and R. Bulla, "Quantum Phase Transition in the Sub-Ohmic Spin-Boson Model: Quantum Monte Carlo Study with a Continuous Imaginary Time Cluster Algorithm," *Phys. Rev. Lett.*, vol. 102, p. 030601, Jan. 2009.
- [68] L. Chen, Y. Yan, M. F. Gelin, and Z. Lü, "Dynamics of the spin-boson model: The effect of bath initial conditions," *The Journal of Chemical Physics*, vol. 158, p. 104109, Mar. 2023.
- [69] E. Paladino, Y. Galperin, G. Falci, and B. Altshuler, " $1/f$ noise: Implications for solid-state quantum information," *Rev. Mod. Phys.*, vol. 86, pp. 361–418, Apr. 2014.
- [70] X. You, A. A. Clerk, and J. Koch, "Positive- and negative-frequency noise from an ensemble of two-level fluctuators," *Phys. Rev. Research*, vol. 3, p. 013045, Jan. 2021.
- [71] J. Johansson, P. Nation, and F. Nori, "QuTiP 2: A Python framework for the dynamics of open quantum systems," *Computer Physics Communications*, vol. 184, pp. 1234–1240, Apr. 2013.
- [72] N. Lambert, T. Raheja, S. Cross, P. Menczel, S. Ahmed, A. Pitchford, D. Burgarth, and F. Nori, "QuTiP-BoFiN: A bosonic and fermionic numerical hierarchical-equations-of-motion library with applications in light-harvesting, quantum control, and single-molecule electronics," *Phys. Rev. Research*, vol. 5, p. 013181, Mar. 2023.
- [73] H.-G. Duan and M. Thorwart, "Quantum Mechanical Wave Packet Dynamics at a Conical Intersection with Strong Vibrational Dissipation," *J. Phys. Chem. Lett.*, vol. 7, pp. 382–386, Feb. 2016.
- [74] H.-G. Duan, V. I. Prokhorenko, R. J. Cogdell, K. Ashraf, A. L. Stevens, M. Thorwart, and R. J. D. Miller, "Nature does not rely on long-lived electronic quantum coherence for photosynthetic energy transfer," *Proc. Natl. Acad. Sci. U.S.A.*, vol. 114, pp. 8493–8498, Aug. 2017.
- [75] H.-G. Duan, M. Thorwart, and R. J. D. Miller, "Does electronic coherence enhance anticorrelated pigment vibrations under realistic conditions?," *The Journal of Chemical Physics*, vol. 151, p. 114115, Sept. 2019.
- [76] H.-G. Duan, A. Jha, L. Chen, V. Tiwari, R. J. Cogdell, K. Ashraf, V. I. Prokhorenko, M. Thorwart, and R. J. D. Miller, "Quantum coherent energy transport in the Fenna–Matthews–Olson complex at low temperature," *Proc. Natl. Acad. Sci. U.S.A.*, vol. 119, p. e2212630119, Dec. 2022.
- [77] A. Jha, P.-P. Zhang, V. Tiwari, L. Chen, M. Thorwart, R. J. D. Miller, and H.-G. Duan, "Unraveling quantum coherences mediating primary charge transfer processes in photosystem II reaction center," *Sci. Adv.*, vol. 10, p. eadk1312, Mar. 2024.
-

-
- [78] R. Trebino, K. W. DeLong, D. N. Fittinghoff, J. N. Sweetser, M. A. Krumbügel, B. A. Richman, and D. J. Kane, "Measuring ultrashort laser pulses in the time-frequency domain using frequency-resolved optical gating," *Review of Scientific Instruments*, vol. 68, pp. 3277–3295, Sept. 1997.
- [79] H.-G. Duan, *Two-dimensional Spectroscopic Study of Biological Photosynthetic Systems and the Solar Cell Functional Materials*. PhD thesis, Hamburg, 2018.
- [80] V. Link, H.-H. Tu, and W. T. Strunz, "Open Quantum System Dynamics from Infinite Tensor Network Contraction," *Phys. Rev. Lett.*, vol. 132, p. 200403, May 2024.
-

Acknowledgement

First and foremost, I would like to thank Prof. Dr. Michael Thorwart for his encouragement and mentorship throughout both my master's and PhD projects. I am also grateful to Prof. Dr. Peter Nalbach for always asking the right questions. For the smooth collaboration on the dissipative TRUECARS project, I thank Dr. Daniel Keefer and Prof. Dr. Shaul Mukamel.

Furthermore, I would like to acknowledge Frederik, Zitong, Charlotte, and Jan, whose theses I had the pleasure of supervising. I am also grateful to the numerous students I have had the opportunity to teach over the years, as well as the teachers that taught me.

I am also grateful for the hospitality of the Flatiron Institute and would like to thank Wolfgang and MirYam for hosting me during my time there. Additionally, I would like to thank my colleagues Carl, Giacomo, Kevin, and Mark at the CCQ for their camaraderie.

Finally, I thank the members of the *Lernhalbgruppe* - Jonathan, Jörn, Mathis, Max, and Niclas for fighting through so many exercise sheets with me.

Eidesstattliche Versicherung

Hiermit versichere ich an Eides statt, die vorliegende Dissertationsschrift selbst verfasst und keine anderen als die angegebenen Hilfsmittel und Quellen benutzt zu haben.

Die Dissertation wurde in der vorgelegten oder einer ähnlichen Form nicht schon einmal in einem früheren Promotionsverfahren angenommen oder als ungenügend beurteilt.

Hamburg, den _____ Unterschrift: _____